Issue 1 2014 | Volume 10

The Journal on Advanced Studies in Theoretical and Experimental Physics, including Related Themes from Mathematics

PROGRESS IN PHYSICS

"All scientists shall have the right to present their scientific research results, in whole or in part, at relevant scientific conferences, and to publish the same in printed scientific journals, electronic archives, and any other media." — Declaration of Academic Freedom, Article 8

ISSN 1555-5534

The Journal on Advanced Studies in Theoretical and Experimental Physics, including Related Themes from Mathematics

PROGRESS IN PHYSICS

A quarterly issue scientific journal, registered with the Library of Congress (DC, USA). This journal is peer reviewed and included in the abstracting and indexing coverage of: Mathematical Reviews and MathSciNet (AMS, USA), DOAJ of Lund University (Sweden), Zentralblatt MATH (Germany), Scientific Commons of the University of St. Gallen (Switzerland), Open-J-Gate (India), Referativnyi Zhurnal VINITI (Russia), etc.

Electronic version of this journal:
http://www.ptep-online.com

Postal Address

Department of Mathematics and Science,
University of New Mexico,
705 Gurley Ave., Gallup, NM 87301, USA

ISSN: 1555-5534 (print)
ISSN: 1555-5615 (online)

Standard Address Number: 297-5092
Printed in the United States of America

January 2014 **Vol. 10, Issue 1**

CONTENTS

Information for Authors and Subscribers

Progress in Physics has been created for publications on advanced studies in theoretical and experimental physics, including related themes from mathematics and astronomy. All submitted papers should be professional, in good English, containing a brief review of a problem and obtained results.

All submissions should be designed in LaTeX format using *Progress in Physics* template. This template can be downloaded from *Progress in Physics* home page http://www.ptep-online.com. Abstract and the necessary information about author(s) should be included into the papers. To submit a paper, mail the file(s) to the Editor-in-Chief.

All submitted papers should be as brief as possible. We accept brief papers, no larger than 8 typeset journal pages. Short articles are preferable. Large papers can be considered in exceptional cases to the section *Special Reports* intended for such publications in the journal. Letters related to the publications in the journal or to the events among the science community can be applied to the section *Letters to Progress in Physics*.

All that has been accepted for the online issue of *Progress in Physics* is printed in the paper version of the journal. To order printed issues, contact the Editors.

This journal is non-commercial, academic edition. It is printed from private donations. (Look for the current author fee in the online version of the journal.)

LETTERS TO PROGRESS IN PHYSICS

Book Review: "Inside Stars. A Theory of the Internal Constitution of Stars, and the Sources of Stellar Energy According to General Relativity"

Pierre A. Millette

Astrophysics research on stellar atmospheres at Department of Physics, University of Ottawa (alumnus), Ottawa, Canada. E-mail: PierreAMillette@alumni.uottawa.ca

This book provides a general relativistic theory of the internal constitution of liquid stars. It is a solid contribution to our understanding of stellar structure from a general relativistic perspective. It raises new ideas on the constitution of stars and planetary systems, and proposes a new approach to stellar structure and stellar energy generation which is bound to help us better understand stellar astrophysics.

The book "Inside Stars. A Theory of the Internal Constitution of Stars, and the Sources of Stellar Energy According to General Relativity" by Larissa Borissova and Dmitri Rabounski [1] provides a general relativistic theory of the internal constitution of liquid stars.

The generally accepted model of stellar constitution considers stars to be high-temperature gaseous plasmas obeying the ideal gas equation of state. However, in the late nineteenth and early twentieth centuries, the question of whether stars are gaseous or liquid was the subject of much debate. P.-M. Robitaille provides a detailed discussion of this debate in his work [2, 3]. Recent evidence for liquid stars, in particular the extensive research performed by P.-M. Robitaille on the liquid metallic hydrogen model of the Sun, and his proposed liquid plasma model of the Sun [4], have re-opened the question.

In this book, the authors provide a novel general relativistic theory of the internal constitution of liquid stars, using a mathematical formalism first introduced by Abraham Zelmanov for calculating physically observable quantities in a four-dimensional pseudo-Riemannian space, known as the theory of chronometric invariants. This mathematical formalism allows to calculate physically observable chronometric-invariant tensors of any rank, based on operators of projection onto the time line and the spatial section of the observer. The basic idea is that physically observable quantities obtained by an observer should be the result of a projection of four-dimensional quantities onto the time line and onto the spatial section of the observer.

In the book, a star is modelled as a sphere of incompressible liquid described by Schwarzschild's metric. However, unlike Schwarzschild's solution which requires that the metric be free of singularities, space-time singularities are considered in this model. The conditions for a spatial singularity, known as a space break, are derived.

For our Sun, a space break is found to be within the Asteroid belt. The theory thus also provides a model of the internal constitution of our solar system. It provides an explanation for the presence of the Asteroid belt, the general structure of the planets inside and outside that orbit, and the net emission of energy by the planet Jupiter.

There is another space break located within a star's field. As a result of their analysis, the authors propose a new classification of stars based on the location of the space breaking of a star's field with respect to its surface. This classification of stars results in three main types: regular stars (covering white dwarfs to super-giants) covered in Chapter 2, of which Wolf-Rayet stars are a subtype, neutron stars and pulsars, covered in Chapter 4 and collapsars (i.e. black holes), covered in Chapter 5. Chapter 3 examines the properties of the stellar wind within their liquid star model.

The stellar mass-luminosity relation, which is the main empirical relation of observational astrophysics, is compared by the authors to that derived in the framework of the liquid model. From this they obtain the physical characteristics of the mechanism that produces energy inside the stars. Using the liquid model, the pressure inside stars can be calculated as a function of radius, including the central pressure. As pointed out by the authors, the temperature of the incompressible liquid star does not depend on pressure, only on the source of stellar energy. The authors match the calculated energy production of the suggested mechanism of thermonuclear fusion of the light atomic nuclei in the Hilbert core (the "inner sun") of the stars to the empirical mass-luminosity relation of observational astrophysics, to determine the density of the liquid stellar substance in the Hilbert core.

In the general relativistic model of liquid stars, the inside of the star is homogeneous, with a small core (about a few kilometres in radius) in its centre. The core is separated from the main mass of the star by the model's collapse surface with the radius depending on the star's mass. Despite almost all the mass of the star being located outside the core (the core is not a black hole), the force of gravity approaches to infinity on the surface of the core due to the inner space breaking of the star's field within it. The super-strong force of gravity is sufficient for the transfer of the necessary kinetic energy to the

lightweight atomic nuclei of the stellar substance, to sustain the process of thermonuclear fusion. Thus, thermonuclear fusion of the light atomic nuclei is possible in the Hilbert core of each star. The energy produced by the thermonuclear fusion is the energy emitted by the stars: the small core of each star is its luminous "inner sun", while the generated stellar energy is transferred to the physical surface of the star by thermal conductivity. Due to the fact that the star's substance is liquid, more and more "nuclear fuel" is delivered from other regions of the star to its luminous Hilbert core, thus supporting the combustion inside the "nuclear boiler", until the time when all the nuclear fuel of the star is spent.

Pulsars and neutron stars are found to be stars whose physical radius is close to the radius of their Hilbert core. They are modelled by introducing an electromagnetic field in the theory to account for their rotation and gravitation. Electromagnetic radiation is found to be emitted only from the poles of those stars, along the axis of rotation of the stars.

Finally, the properties of black holes as derived from the model are considered. The authors find that regular stars cannot collapse. They derive the conditions for pulsars and neutron stars to become collapsars. Interestingly, the authors apply their model to the Universe and, based on their results, suggest that the Universe can be considered as a sphere of perfect liquid which is in a state of gravitational collapse (the liquid model of the Universe). Hence they deduce that the observable Universe is a collapsar, a huge black hole.

This book represents a solid contribution to our understanding of stellar structure from a general relativistic perspective. It provides a general relativistic underpinning to the theory of liquid stars. It raises new ideas on the constitution of stars and planetary systems, and proposes a new approach to stellar structure and stellar energy generation which is bound to generate much new research, and help us better understand stellar astrophysics.

Submitted on October 24, 2013 / Accepted on October 25, 2013

References

1. Borissova L. and Rabounski D. Inside Stars. American Research Press, Rehoboth (NM, USA), 2013 (available from Progress in Physics website).
2. Robitaille P.-M. A Thermodynamic History of the Solar Constitution — I: The Journey to a Gaseous Sun, *Progress in Physics*, 2011, v. 7(3), pp. 3–25.
3. Robitaille P.-M. A Thermodynamic History of the Solar Constitution — II: The Theory of a Gaseous Sun and Jeans' Failed Liquid Alternative, *Progress in Physics*, 2011, v. 7(3), pp. 41–59.
4. Robitaille P.-M. A High Temperature Liquid PLasma Model of the Sun, *Progress in Physics*, 2007, v. 3(1), pp. 70–81.

Mass-Radius Relations of Z and Higgs-Like Bosons

Bo Lehnert

Alfvén Laboratory, Royal Institute of Technology, SE-10044 Stockholm, Sweden. E-mail: Bo.Lehnert@ee.kth.se

Relations between the rest mass and the effective radius are deduced for the Z boson and the experimentally discovered Higgs-like boson, in terms of a revised quantum electrodynamic (RQED) theory. The latter forms an alternative to the Standard Model of elementary particles. This results in an effective radius of the order of 10^{-18} m for the Z boson, in agreement with accepted data. A composite model for the Higgs-like boson is further deduced from the superposition of solutions represented by two Z bosons. This model satisfies the basic properties of the observed Higgs-like particle, such as a vanishing charge and spin, a purely electrostatic and strongly unstable state, and an effective radius of about 10^{-18} m for a rest mass of 125 GeV.

1 Introduction

Recently an elementary particle has been discovered at the projects ATLAS [1] and CMS [2] of CERN, being unstable, having vanishing net electric charge and spin, and a rest mass of 125 GeV. This discovery was made in connection with a search for the Higgs boson and its theoretical base given by the Standard Model of an empty vacuum state.

Being distinguished from the latter model, a revised quantum electrodynamic (RQED) theory has been elaborated [3], as founded on the principle of a non-empty vacuum state. It is supported by the quantum mechanical Zero Point Energy [4] and the experimentally verified Casimir force [5]. This relativistic and gauge invariant theory of broken symmetry is based on a nonzero electric field divergence in the vacuum, in combination with a vanishing magnetic field divergence due to the non-existence of observed magnetic monopoles.

Among the subjects being treated by RQED theory, this report is devoted to the mass-radius relation obtained for the Z boson, and to that associated with a model of the Higgs-like boson. This provides an extension of an earlier analysis on a Higgs-like particle [6].

2 Particle with vanishing net electric charge

Due to the RQED theory of axisymmetric particle-shaped steady states with rest mass, a separable generating function

$$F(r,\theta) = CA - \phi = G_0 G(\rho,\theta)\,, \quad G = R(\rho)\cdot T(\theta) \tag{1}$$

can be introduced in a spherical frame (r,θ,φ) of reference [3]. There is an electrostatic potential ϕ and an electric charge density $\bar{\rho} = \varepsilon_0 \operatorname{div}\mathbf{E}$, a current density $\mathbf{j} = (0,0,C\bar{\rho})$ with $\mathbf{C}^2 = c^2$ and $C = \pm c$ representing the two spin directions along φ, and a magnetic vector potential $\mathbf{A} = (0,0,A)$. A dimensionless radial coordinate $\rho = r/r_0$ is introduced with a characteristic radius r_0, and a dimensionless generating function G with the characteristic amplitude G_0.

As based on the function (1), the general forms of the potentials and the charge density become

$$CA = -(\sin\theta)^2\, DF\,, \tag{2}$$

$$\phi = -\left[1 + (\sin\theta)^2\, D\right] F\,, \tag{3}$$

$$\bar{\rho} = -\frac{\varepsilon_0}{r_0^2\rho^2}\, D\left[1 + (\sin\theta)^2\, D\right] F\,, \tag{4}$$

where the operators are

$$D = D_\rho + D_\theta$$
$$D_\rho = -\frac{\partial}{\partial\rho}\left(\rho^2\frac{\partial}{\partial\rho}\right) \qquad D_\theta = -\frac{\partial^2}{\partial\theta^2} - \frac{\cos\theta}{\sin\theta}\frac{\partial}{\partial\theta}\,. \tag{5}$$

Since the analysis will be applied to the special class of particles with vanishing net electric charge, such as the Z and Higgs-like bosons, the radial part R of the function (1) has to be convergent at the origin $\rho = 0$, and a polar part T is chosen having top-bottom symmetry with respect to the equatorial plane $\theta = \pi/2$. This is due to earlier performed basic deductions [3].

Due to the non-zero electric field divergence, there are local intrinsic charges even when the net integrated charge vanishes. For a convergent generating function the total integrated energy W can either be expressed in terms of the field energy density

$$w_f = \frac{1}{2}\,\varepsilon_0\left(\mathbf{E}^2 + c^2\mathbf{B}^2\right) \tag{6}$$

or of the source energy density

$$w_s = \frac{1}{2}\,\bar{\rho}\,(\phi + CA) \tag{7}$$

from which

$$W = \int w_f\, dV = \int w_s\, dV. \tag{8}$$

We shall use the option (7) for which the local contribution to the particle mass becomes

$$dm_0 = \frac{w_s}{c^2}\, dV \tag{9}$$

and that related to the angular momentum (spin) becomes

$$ds_0 = Cr(\sin\theta)\; dm_0 \tag{10}$$

for a volume element $dV = 2\pi r^2 (\sin\theta)\, d\theta dr$ in a spherical frame.

A generating function being convergent both at $\rho = 0$ and at large ρ, and having top-bottom symmetry, is finally chosen through the form

$$R = \rho^{\gamma} \cdot e^{-\rho}, \qquad T = (\sin\theta)^{\alpha}, \tag{11}$$

where $\gamma \geqslant 1$ and $\alpha \geqslant 1$. The part R then increases to a maximum at the effective radius $\hat{r} = \gamma r_0$ after which it drops steeply towards zero at large ρ.

3 Model of a Z boson

A Z boson is first considered, having zero net electric charge, spin $h/2\pi$, a rest mass of 91 GeV, and an effective radius of about 10^{-18} m according to given data [7].

From (1)–(5), (8), (9) and (11) the product of the mass m_{0Z} and the effective radius $\hat{r}_Z = \gamma r_{0Z}$ becomes

$$\hat{r}_Z m_{0Z} = \pi \left(\varepsilon_0 / c^2\right) r_{0Z}^2 G_0^2 \gamma J_{mZ}, \tag{12}$$

where

$$J_{mZ} = \int_0^{\infty} \int_0^{\pi} f\, g_Z \, d\rho \, d\theta \tag{13}$$

and

$$f = -(\sin\theta)\, D \left[1 + (\sin\theta)^2 D\right] G, \tag{14}$$

$$g_Z = -\left[1 + 2(\sin\theta)^2 D\right] G. \tag{15}$$

The spin is further given by

$$s_{0Z} = \pi \varepsilon_0 \left(C/c^2\right) r_{0Z}^2 G_0^2 J_{sZ} = \pm h/2\pi \tag{16}$$

where

$$J_{sZ} = \int_0^{\infty} \int_0^{\pi} \rho\, (\sin\theta)\, f\, g_Z \, d\rho \, d\theta. \tag{17}$$

Combination of (12)–(17) yields

$$\hat{r}_Z m_{0Z} = \frac{h}{2\pi c} \frac{\gamma J_{mZ}}{J_{sZ}}. \tag{18}$$

This relates the mass to the effective radius, in a way being dependent on the profile shape of the generating function:

- A numerical analysis of the $1 \leqslant \gamma \leqslant 10$ and $1 \leqslant \alpha \leqslant 10$ cases, results in the large ranges $17.7 \leqslant J_{mZ} \leqslant 9.01 \times 10^{15}$ and $39.8 \leqslant J_{sZ} \leqslant 1.83 \times 10^{16}$ of the amplitudes J_{mZ} and J_{sZ}. The last factor of the right-hand member in (18) stays however within the limited range of $0.445 \leqslant (\gamma J_{mZ}/J_{sZ}) \leqslant 0.904$.
- In the asymptotic cases $\gamma \gg \alpha \gg 1$ and $\alpha \gg \gamma \gg 1$ the values of $(\gamma J_{mZ}/J_{sZ})$ become $15/38$ and 1, respectively. This is verified in an earlier analysis [8].
- In spite of the large variations of J_{mZ} and J_{sZ} with the profile shape, the factor $\gamma J_{mZ}/J_{sZ}$ thus has a limited variation within a range of about 0.4 to 1.

For the present deduced model, the rest mass of 91 GeV then results in an effective radius in the range of 0.87×10^{-18} to 2.2×10^{-18} m. This is consistent with the given value of $\hat{r}_Z$.

For the expressions (2) and (3) combined with the form (11) can finally be seen that there is a moderately large deviation from a state $\mathbf{E}^2 = c^2 \mathbf{B}^2$ of equipartition between the electrostatic and magnetostatic particle energies.

4 Model of a Higgs-like boson

One of the important reactions being considered in the experiments at CERN is the decay of the observed Higgs-like boson into two Z bosons, and further into four leptons. Since the Higgs-like boson was found to have a mass of 125 GeV, and the Z bosons have masses of 91 GeV each, an extra contribution of 57 GeV is required for the decay into the Z bosons. It can then be conceived that this extra energy is "borrowed" from the Heisenberg uncertainty relation when the entire decay process takes place in a very short time. At least one of the involved Z bosons then behaves as a virtual particle. In this connection is also observed that the magnitude of the Higgs-like boson mass has not been predicted through the theory by Higgs [9].

With the decay process in mind, a relation will now be elaborated between the mass and the effective radius of the Higgs-like boson. Then it has first to be observed that a relation similar to equation (18) cannot be straightforwardly deduced. This is because the Higgs-like boson has no spin, and its related effective radius can on account of the required extra energy not become identical with that of a single Z boson.

Solutions for models of massive individual bosons and leptons are available from RQED theory. The field equations are linear, and these solutions can be superimposed to form a model of a Higgs-like particle having vanishing charge and spin. It can be done in terms of four leptons or two Z bosons. Choosing the latter option [6], superposition of the potentials (2) and (3) for two modes with opposite spin directions results in a composite Higgs-like mode with zero charge and spin but nonzero rest mass. This mode has no magnetic field, is purely electrostatic, and is thus expected to be highly unstable. In analogy with the deductions (1)–(11), the corresponding integrated mass m_{0H} becomes

$$\hat{r}_H m_{0H} = \pi \left(\varepsilon_0 / c^2\right) r_{0H}^2 G_0^2 \gamma J_{mH} \tag{19}$$

with the effective radius $\hat{r}_H \neq \hat{r}_Z$ and

$$J_{mH} = \int_0^{\infty} \int_0^{\pi} f\, g_H \, d\rho \, d\theta. \tag{20}$$

Here f is still obtained from (14) and

$$g_H = -2\left[1 + (\sin\theta)^2 D\right] G = g_Z - G \tag{21}$$

with g_Z given by (15). Combination of (19) and (12) yields

$$\frac{\hat{r}_H}{\hat{r}_Z} = \frac{r_{0H}}{r_{0Z}} = \frac{m_{0H}}{m_{0Z}} \frac{J_{mZ}}{J_{mH}} . \qquad (22)$$

The dependence on the profile shape of the generating function is as follows:

- Numerical analysis in the ranges $1 \leqslant \gamma \leqslant 10$ and $1 \leqslant \alpha \leqslant 10$ results in the amplitude variations $138 \leqslant J_{mZ} \leqslant 9.8 \times 10^{15}$ and $287 \leqslant J_{mH} \leqslant 1.8 \times 10^{16}$, but their ratio is strongly limited to $2.03 \leqslant J_{mH}/J_{mZ} \leqslant 2.20$.
- From expression (21) at large γ and α can further be seen that J_{mH}/J_{mZ} approaches the asymptotic value 2.

With these evaluations, and the experimentally determined masses $m_{0Z} = 91$ GeV and $m_{0H} = 125$ GeV, the effective radius $\hat{r}_H$ of the Higgs-like boson comes from (22) out to be in the range 0.54×10^{-18} to 1.5×10^{-18} m.

5 Summary

The present model of the Z boson leads to an effective radius of the order of 10^{-18} m, in agreement with given data. This can be taken as support of the present theory.

Concerning the present model of a Higgs-like boson, the following results should be observed:

- An imagined "reversal" of the decay of a Higgs-like boson into two Z bosons initiates the idea of superimposing two Z boson modes to form a model of such a particle. The resulting composite particle solution is consistent with the point made by Quigg [7] that the Higgs is perhaps not a truly fundamental particle but is built out of as yet unobserved constituents.
- The present model of a Higgs-like boson satisfies the basic properties of the particle observed at CERN. It has a vanishing electric charge and spin, a nonzero rest mass, and is unstable due to its purely electrostatic nature.
- The present theory finally results in an effective radius of the order of 10^{-18} m for the experimentally detected Higgs-like particle having a rest mass of 125 GeV, and vice versa.

Acknowledgement

The author is indebted to Dr. Ahmed Mirza for valuable help with the numerical evaluations of this report.

Submitted on November 4, 2013 / Accepted on November 10, 2013

References

1. Aad G. et al., ATLAS Collaboration. Observation of a new particle in the search for the Standard Model Higgs boson with the ATLAS detector at the LHC. *Phys.Lett.*, 2012, v. B716, 1–29.
2. Chatrchyan S. et al., CMS Collaboration. Observation of a new boson at a mass of 125 GeV with the CMS experiment at the LHC. *Phys.Lett.*, 2012, v. B716, 30–61.
3. Lehnert B. Revised Quantum Electrodynamics. In Dvoeglazov V. V. (ed). Contemporary Fundamental Physics. Nova Science Publishers Inc., New York, 2013.
4. Schiff L. I. Quantum Mechanics. McGraw-Hill Book Comp. Inc., New York-Toronto-London, 1949, Ch.IV, Sec.13.
5. Casimir H. B. G. On the attraction between two perfectly conducting plates. *Proc.K.Ned.Akad.Wet.*,1948, v. 51, 793–795.
6. Lehnert B. Higgs-like particle due to revised quantum electrodynamics. *Progress in Physics*, 2013, v. 3, 31–32.
7. Quigg C. The coming revolutions in particle physics. *Scientific American*, February 2008, 38–45.
8. Lehnert B. and Roy S. Extended electromagnetic theory. World Scientific Publishers, Co. Pte. Ltd, Singapore, 1998, Ch.5.2.
9. Higgs P. W. Spontaneous symmetry breakdown without massless bosons. *Physical Review*, 1966, v. 145, 1156–1168.

Reexamination of Nuclear Shape Transitions in Gadolinium and Dysprosium Isotopes Chains by Using the Geometric Collective Model

Khalaf A.M.[1], Aly H.F.[2], Zaki A.A.[2] and Ismail A.M.[2]

[1]Physics Department, Faculty of Science, Al-Azhar University, Cairo, Egypt. E-mail: ali_khalaf43@hotmail.com
[2]Hot Laboratories Center, Atomic Energy Authority, P.No. 13759, Cairo, Egypt. E-mail: dr_ahmedph@yahoo.com

The geometric collective model proposed in a previous paper in examined to describe the nuclear shape transitions for Gd and Dy isotopes chains. The optimized model parameters for each nucleus have been adjusted by fitting procedure using a computer simulated search program in order to reproduce the excitation energies ($2_1^+, 4_1^+, 6_1^+, 8_1^+, 0_2^+, 2_3^+, 4_3^+, 2_2^+, 3_1^+$ and 4_2^+) and the two neutron separation energies in all nuclei in each isotopic chain. Calculated potential energy surface (PES'S) describing all deformation effects of each nucleus have been extracted. Our systematic studies on Gd / Dy chains have revealed a shape transition from spherical vibrator to axially deformed rotor when moving from the lighter to heavier isotopes.

1 Introduction

Recent developments in nuclear structure have brought considerable focusing on the problems of shape phase transition and shape coexistence phenomena [1]. For instance, several isotopes have been found to undergo shape phase evolution of first order from spherical vibrator to deformed axially symmetric rotor [2–6] and phase transition of second order from spherical vibrator to deformed γ - soft [7–9]. The study of shape phase transitions in nuclei was best done by using the interacting boson model (IBM) [10]. The original version of IBM (IBM-1) includes s and d bosons, it defines six-dimensional space and this leads to a description in terms of a unitary group U(6). Three dynamical symmetries in the IBM-1 were shown [11]: the U(5) symmetry corresponding to spherical oscillator, the SU(3) symmetry corresponding to deformed axially rotor and the O(6) symmetry corresponding to the γ - soft asymmetric rotor shapes. These three symmetry limits from a triangle known as a Casten triangle that represents the nuclear phase diagram [12]. The X(5) critical point symmetry [13] has been found to correspond to the first order transition between U(5) and SU(3), while the E(5) critical point symmetry [14] has been found to correspond to the second order transition between U(5) and O(6).

In the previous paper [3], we used the flexible and powerful geometric collective model (GCM) [3, 15–18] to describe the quantum phase transition between spherical and deformed shapes for doubly even nuclei in lanthanide and actinide isotopes chains. The potential energy surfaces (PES'S) describing all deformed effects of each nucleus were extracted in terms of the intrinsic shape parameters β and γ. The parameter β is related to the axial deformation of the nucleus, while γ measure the deviation from axial symmetry. In the present work, it is of interest to examine the GCM in investigating the shape transition from spherical vibrator to axially deformed rotor for Gd and Dy isotopic chains by analyzing the PES'S. In section 2, we construct the GCM Hamiltonian and its eigenfunction. In section 3, we generated the PES'S to classify shape phase transitions and to decide if a nucleus is close to criticality. In section 4, we applied our model to the rare earth Gd / Dy isotopic chains which evolve a rapid structural charges from spherical to well-deformed nuclei when moving from lighter to the heavier isotopes.

2 The GCM Hamiltonian and eigenstates

In GCM, the Hamiltonian of the nucleus, in appropriate units, can be expressed as a series expansion in terms of the surface deformation coordinates α and the conjugate momenta π as [3]:

$$\begin{aligned} H = & \frac{1}{2B_2}[\pi\times\pi]^{(0)} + C_2[\alpha\times\alpha]^{(2)} \\ & + C_3[[\alpha\times\alpha]^{(2)}\times\alpha]^{(0)} \\ & + C_4[\alpha\times\alpha]^{(0)}[\alpha\times\alpha]^{(0)} \end{aligned} \tag{1}$$

The eigenstates of the the Hamiltonian 1 associated with the number ν of quanta and definite seniority λ, angular momentum L and projection M can be denoted by the Ket

$$|\nu\lambda\mu LM\rangle = F_\ell^\lambda(\beta)\sum_k \varphi_k^{\lambda\mu L}(\gamma)D_{Mk}^{L_*}(\omega_i) \tag{2}$$

where

$$\ell = \frac{1}{2}(\nu-\lambda) \tag{3}$$

and μ indicates the remaining quantum numbers required to fully characterize the states of the Hamiltonian 1. ω_i are the Euler angles, β and γ are the intrinsic coordinates. $D_{Mk}^{L_*}(\omega_i)$ are the Wigner functions that are the irreducible representation of the O(3) group.

In equation 2 $F_\ell^\lambda(\beta)$ are functions of β associated with the radial part of a five-dimensional oscillator

$$\begin{aligned} F_\ell^\lambda(\beta) = & \left[\frac{2(n_i)}{\Gamma(n+\lambda+\frac{5}{2})}\right]^{1/2}\left(\frac{C_2}{\hbar\omega}\right)^{\frac{5}{4}+\frac{\lambda}{2}}\beta^\lambda \\ & \cdot L_n^{\lambda+\frac{3}{2}}\cdot\left(\left(\frac{C_2}{\hbar\omega}\right)\beta^2\right)e^{-\frac{1}{2}\frac{C_2}{\hbar\omega}\beta^2} \end{aligned} \tag{4}$$

where $L_n^{\lambda+\frac{3}{2}}$ are the well-known Laguerre polynomials and the function is normalized for the volume element $\beta 4 d\beta$. The γ-dependent functions $\varphi_k^{\lambda\mu L}$ satisfy the differential equation

$$\Lambda^2 \varphi_k^{\lambda\mu L} = \lambda(\lambda+3)\varphi_k^{\lambda\mu L} \tag{5}$$

where Λ^2 is the seniority operator (Casimir operator of O(5)) which has the form

$$\Lambda^2 = -\frac{1}{\sin 3\gamma}\frac{\partial}{\partial\gamma} + \sum_{k=1}^{3} I_k^{-1}\grave{L}_k^2(\omega_i) \tag{6}$$

with

$$I_k = 4B_2 \sin^2\left(\gamma - \frac{2\pi}{3}k\right) \tag{7}$$

I_k are the moments of inertia with respect to the principle axes. For arbitrary angular momentum L and λ , $\varphi(\gamma)$ reads

$$\varphi_{\grave{k}}^{\lambda+2,\mu,L+2}(\gamma) = \sum_k \varphi_{k,\bar{k}}^{\lambda LL+2}\left(\gamma, \frac{\partial}{\partial\gamma}\right)\varphi_k^{\lambda\mu L}(\gamma) \tag{8}$$

$$\varphi_{\bar{k}}^{\lambda+2,\mu,L+2}(\gamma) =$$

$$= \sum_{\bar{L}\bar{k}k}\left(\sqrt{35(2\bar{L}+1)}W(L,L+2,2,2,2\bar{L}) \times \right. \tag{9}$$

$$\left. Q_{\bar{k},\grave{k}}^{\lambda+1,\bar{L},L+2}\left(\gamma, \frac{\partial}{\partial\gamma}\right) Q_{k,\bar{k}}^{\lambda,L,\bar{L}}\left(\gamma, \frac{\partial}{\partial\gamma}\right)\varphi_k^{\lambda\mu L}(\gamma)\right)$$

where W is a Racah coefficient and $Q_{k,\bar{k}}^{\lambda,L,\bar{L}}(\gamma, \frac{d}{d\gamma})$ is an operator function of γ and $\frac{d}{d\gamma}$.

3 Potential energy surfaces (PES'S) and critical point symmetries

The PES depends only upon the shape of the nucleus not it orientation in space, and can thus be expressed purely in terms of the shape coordinates β and γ as [3]:

$$V(\beta,\gamma) = C_2\frac{1}{\sqrt{5}}\beta^2 - C_3\sqrt{\frac{2}{35}}\beta^3\cos 3\gamma + C_4\frac{1}{5}\beta^4 \tag{10}$$

where $\beta \in [0,\infty]$ and $\gamma \in [0, 2\pi/3]$

The equilibrium shape associated to the GCM Hamiltonian can be obtained by determining the minimum of energy surface with respect to the geometric variables β and γ, i.e the first derivative vanish. Since the parameter C_2 controls the steepness of the potential, and therefore, the dynamical fluctuations in γ, it strongly affects the energies of excited intrinsic states. The parameter $C_3 = 0$ gives a γ-flat potential and an increase of C_3 introduces a γ-dependence the potential with a minimum at $\gamma = 0$. Changing C_3 will indeed induce a γ-unstable to symmetric rotor transition, it is best to simultaneously vary C_2 and C_4 as well. The shape transition from vibrator to rotor is achieved by starting from the vibrator limit, lowering C_2 from positive to negative value, increasing C_4 to large positive value, which gradually increasing C_3 (lowering C_2 from positive to negative value, introducing a large positive C_4 and a positive C_3).

4 Numerical results applied to Gd and Dy isotopes chains

The N = 90 isotones ^{154}Gd [15, 16] and ^{156}Dy [17, 18] were seen to provide good example to transition from spherical to axially deformed. In our calculation we will examine and systematically study the lanthanide $^{148-162}$Gd and $^{150-164}$Dy isotopes because of the richness of available experimental data indicating a transition of nuclear shapes from spherical to deformed form. The ground band levels are shown in Figure (1). We can see that the energy values for each spin states in lanthanide change almost linearly for $N \leq 88$ and become quite flat for N ≥ 90. This is consistent with the onset of the Z = 64 sub-shell effect. For actinide the energy levels become flat for N ≥ 144. The optimized model parameters for each nucleus was adjusted by fitting procedure using a computer simulated search program in order to describe the gradual change in the structure as neutron number varied and to reproduce the properties of the selected reliable state of positive parity excitation ($2_1^+, 4_1^+, 6_1^+, 8_1^+, 0_2^+, 2_3^+, 4_3^+, 2_2^+, 3_1^+$ and 4_2^+) and the two neutron separation energies of all isotopes in each isotopic chain. The resulting parameters are listed explicitly in Tables (1).

For the isotopic chains investigated here, the collective properties are illustrated by represented the calculated potential energy surface (PES) describing all deformation effects of the nucleus. We investigated the change of nuclear structure

Table 1: The GCM parameters as derived in fitting procedure used in the calculation of the Gd and Dy isotopes.

Nucleus	C_2	C_3	C_4
^{148}Gd	16.53067	1.48970	-34.76151
^{150}Gd	9.79566	11.28331	-5.21603
^{152}Gd	-26.55250	53.24420	138.12500
^{154}Gd	-71.41529	104.21630	313.83380
^{156}Gd	-91.19133	127.81150	392.95380
^{158}Gd	-101.97220	141.63350	437.50440
^{160}Gd	-111.19320	153.76500	476.06680
^{162}Gd	-120.17800	165.64110	513.72330
^{150}Dy	18.56558	1.70251	-38.99710
^{152}Dy	10.69898	12.69373	-5.14990
^{154}Dy	-29.90650	59.16022	154.37500
^{156}Dy	-79.02660	114.63790	346.26770
^{158}Dy	-99.93424	139.43080	429.68950
^{160}Dy	-110.88850	153.43620	474.89930
^{162}Dy	-120.13350	165.59310	513.55260
^{164}Dy	-129.12150	177.47260	551.221306

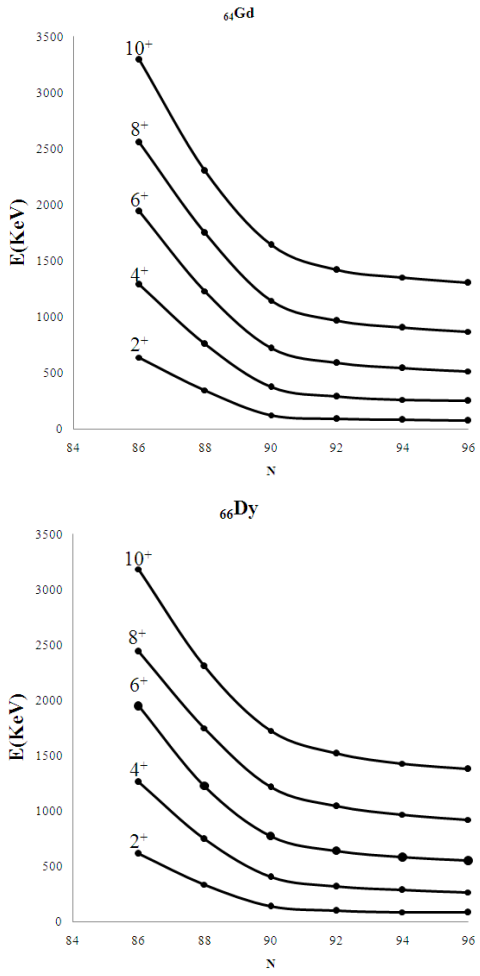

Fig. 1: Systematics of low-lying yrast level energies in even-even lanthanides Gd/Dy isotopes. The $2^+, 4^+, ...10^+$ level energies are plotted. The states are labeled by I^π.

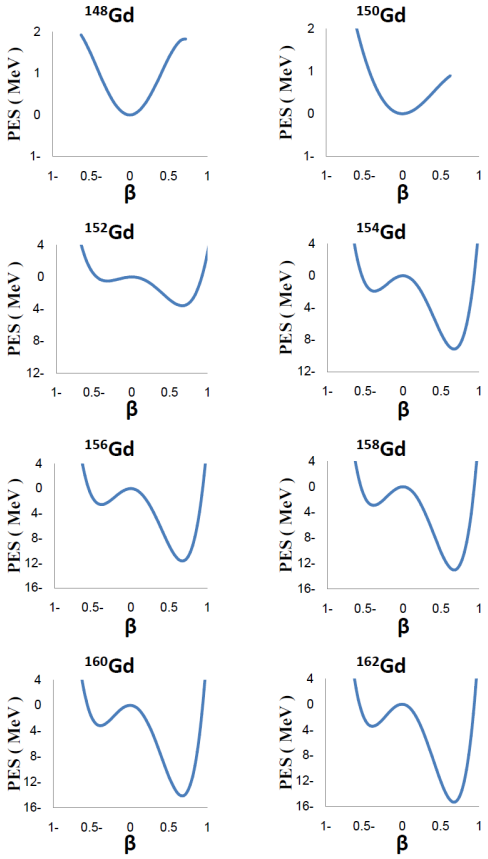

Fig. 2: Potential energy surface (PES) calculated with GCM as a function of the shape parameter β for shape phase transition from spherical to prolate deformed for Gadolinium isotope chain $^{148-162}_{64}$Gd.

within these chains as illustrated in Figures (2, 3). The PES's versus the deformation parameter β for lanthanide isotopic chains of nuclei evolving from spherical to axially symmetric well deformed nuclei. We remark that for all mentioned nuclei, the PES is not flat, exhibiting a deeper minimum in the prolate ($\beta > 0$) region and a shallower minimum in the oblate ($\beta < 0$) region. Relatively flat PES occur for the N = 86 nuclei ^{150}Gd and ^{152}Dy. A first order shape phase transition with change in number of neutrons when moving from the lighter to heavier isotopes, i.e U(5) - SU(3) transitional region are observed.

The present result for ^{154}Gd is in good agreement with Nilsson-Strutinsky BCS calculations [18]. However, the existence of a bump in the PES is related to the success of the confined γ-soft (BCS) rotor model [19], employing an infinite square well potential displaced from zero, as well as to the relevance of Davidson potentials [20–22]. It also be related to the significant five-dimensional centrifugal effect [22–25].

5 Conclusion

In the present paper exact numerical results of GCM Hamiltonian along the shape phase transition line from harmonic spherical vibrator shape to axially deformed rotor shape are obtained. A systematic study of even-even $^{148-162}$Gd and $^{150-164}$Dy isotopes chains in the lanthanide region is presented. For each nucleus the GCM parameters C_2, C_3, C_4 were optimized to fit the energy ratios between selected low-lying states. The geometric character of the nuclei has been visualized by plotting the PES'S obtained from the GCM Hamiltonian. In these chains, nuclei evolve from spherical to prolate axially deformed rotor when moving from the lighter to the heavier isotopes. Also we have analyzed the critical points of the shape phase transition in the space of the GCM parameters C_2, C_3 and C_4.

Submitted on: July 25, 2013 / Accepted on: August 02, 2013

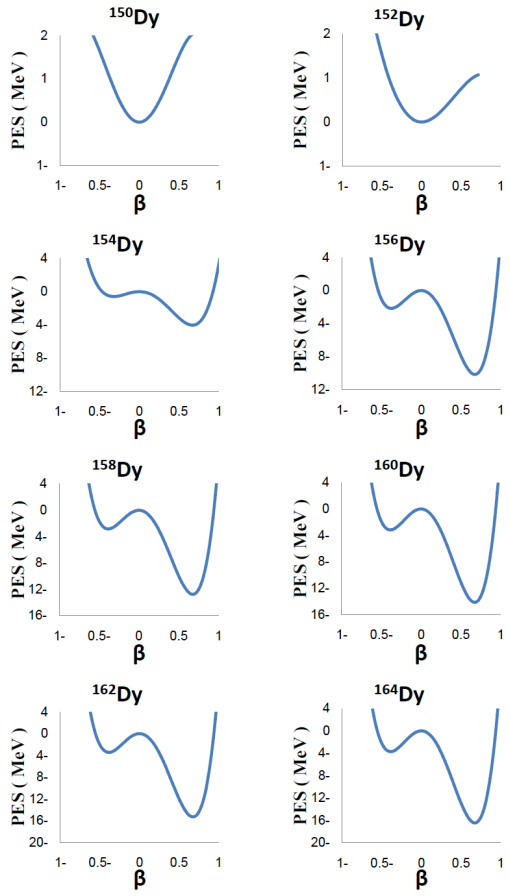

Fig. 3: Potential energy surface (PES) calculated with GCM as a function of the shape parameter β for shape phase transition from spherical to prolate deformed for Dysprosium isotope chain $^{150-164}_{66}$Dy.

References

1. Iachello F. and Zamfir N.V. Quantum Phase Transitions in Mesoscopic Systems. *Physical Review Letters*, 2004, v. 92(3), 212501–212505.
2. Khalaf A.M. and Awwad T.M. A Theoretical Description of U(5)-SU(3) Nuclear Shape Transitions in the Interacting Boson Model. *Progress in Physics*,2013, v. 1, 7–11.
3. Khalaf A.M. and Ismail A.M. The Nuclear Shape Phase Transitions Studied Within the Geometric Collective Model. *Progress in Physics*, 2013, v. 2, 51–55.
4. Khalaf A.M. and Ismail A.M. Structure Shape Evolution in Lanthanide and Actinide Nuclei. *Progress in Physics*, 2013, v. 2, 98-104.
5. Rosensteel G and Rowe D.J. Phase Transitions and Quasidynamical Symmetry in Nuclear Collective Models, III: The U(5) to SU(3) Phase Transition in the IBM. *Nuclear Physics*, 2005, v. A759, 92–128.
6. Liu Y.X., Mu L.Z. and Wei H. Approach to The Rotation Driven Vibrational to Axially Rotational Shape Phase Transition Along The Yrast Line of a Nucleus. *Physics Letters*, 2006, v. B633, 49–53.
7. Heinze S. et al. Evolution of spectral properties along the O(6)-U(5) transition in the interacting boson model. I. Level dynamics. *Physical Review*, 2006, v. C76, 014306–014316.
8. Zhang Y., Hau Z. and Liu Y.X. Distinguishing a First Order From a Second Order Nuclear Shape Phase Transition in The Interacting Boson Model. *Physical Review*, 2007, v. C76, 011305R–011308R.
9. Casten R.F. and Zamfir N.V. Evidence for a Possible E(5) Symmetry in 134Ba. *Physical Review Letters*, 2000, v. 85, 3584–3586, Casten R.F. and Zamfir N.V. Empirical Realization of a Critical Point Description in Atomic Nuclei. *Physical Review Letters*, 2001, v. 87, 052503–052507.
10. Iachello F. and Arima A. The Interacting Boson Model. Cambridge University Press, Cambridge, England, 1987.
11. Arima A. and Iachello F. Interacting Boson Model of Collective States I. The Vibrational Limit. *Annals of Physics*, 1976,(N.Y.) v. 99, 253–317, Arima A. and Iachello F. Interacting Boson Model of Collective States II. The Rotational Limit. *Annals of Physics*, 1978,(N.Y.) v. 111, 201–238.
12. Casten R.F. Nuclear Structure from a Simple Prespective. Oxford University, Oxford, 1990.
13. Iachello F. Analytic Prescription of Critical Point Nuclei in a Spherical Axially Deformed Shape Phase Transtion. *Physical Review Letters*, 2001, v. 87, 052502–052506.
14. Iachello F. Dynamic Symmetries at The Critical Point. *Physical Review Letters*, 2000, v. 85 3580–3583.
15. Tonev D. et al. Transition Probabilities in 154Gd: Evidence for X(5) Critical Point Symmetry. *Physical Review*, 2004, v. C69, 034334–034339.
16. Dewald A. et al. Shape changes and test of the critical-point symmetry X(5) in N = 90 nuclei. *The European Physical Journal*, 2004, v. A20, 173–178.
17. Caprio M.A. et al. Low-Spin Structure of 156Dy Through -ray Spectroscopy. *Physical Review*, 2002, v. C66, 054310–054328.
18. Zhang J.Y. et al. Phase/shape coexistence in 152Sm in the geometric collective model. *Physical Review*, 1999, v. C60, 061304R–061308R.
19. Turken N. and Inci I. Comparing some predictions between Davidson-like potentials and interacting boson model: X(5) behavior of even-even 128-140Nd isotopes. *Physics of Atomic Nuclei*, 2008, v. 71, 1918–1925.
20. Bonatsos D. et al. Ground state bands of the E(5) and X(5) critical symmetries obtained from Davidson potentials through a variational procedure. *Physics Letters*, 2004, v. B584, 40–47.
21. Bonatsos D. et al. E(5) and X(5) Critical Point Symmetries Obtained From Davidson Potentials Through a Variational Procedure. *Physical Review*, 2004, v. C70, 024305–024314.
22. Caprio M.A. Effects of $\beta - \gamma$ coupling in transitional nuclei and the validity of the approximate separation of variables. *Physical Review*, 2005, v. C72, 054323–054333.
23. Rowe D.J. A computationally tractable version of the collective model. *Nuclear Physics*, 2004, v. A735, 372–392.
24. Rowe D.J., Turner P.S. and Repka J. Spherical harmonics and basic coupling coefficients for the group SO(5) in an SO(3) basis. *Journal of Mathematical Physics*, 2004, v. 45, 2761–2784.
25. Rowe D.J. and Turner P.S. The Algebraic Collective Model. *Nuclear Physics*, 2005, v. A753, 94–105.

Nuclear Potential Energy Surfaces and Critical Point Symmetries within the Geometric Collective Model

Khalaf A.M.[1], Aly H.F.[2], Zaki A.A.[2] and Ismail A.M.[2,3]

[1]Physics Department, Faculty of Science, Al-Azhar University, Cairo, Egypt. E-mail: ali_khalaf43@hotmail.com
[2]Hot Laboratories Center, Atomic Energy Authority, P.No. 13759, Cairo, Egypt.
[3]Physics Department, Faculty of Science and Arts, Bukairiyah, Qassim University, Kingdom Saudi Arabia.
Corresponding Author: E-mail: dr_ahmedph@yahoo.com

The critical points of potential energy surface (PES's) of the limits of nuclear structure harmonic oscillator, axially symmetric rotor and deformed γ-soft and discussed in framework of the general geometric collective model (GCM). Also the shape phase transitions linking the three dynamical symmetries are studied taking into account only three parameters in the PES's. The model is tested for the case of $^{238}_{92}$U , which shows a more prolate behavior. The optimized model parameters have been adjusted by fitting procedure using a simulated search program in order to reproduce the experimental excitation energies in the ground state band up to 6^+ and the two neutron separation energies.

1 Introduction

Shape phase transitions from one nuclear shape to another were first discussed in framework of the interacting boson model (IBM) [1]. The algebraic structure of this model is based upon U(6) and three dynamical symmetries arise involving the sub algebras U(5), SU(3) and O(6). There have been numerous recent studies of shape phase transitions between the three dynamical symmetries in IBM [2–9]. The three different phases are separated by lines of first-order phase transition, with a singular point in the transition from spherical to deformed γ-unstable shapes, which is second order. In the usual IBM-1 no triaxial shape appears.

Over the years, studies of collective properties in the framework of geometric collective model (GCM) [3, 10–12] have focused on lanthanide and actinide nuclei. In GCM the collective variables β (the ellipsoidal deformation) and γ (a measure of axial asymmetry) are used. The characteristic nuclear shapes occuring in the GCM are shown in three shapes which are spherical, axially symmetric prolate deformed (rotational) and axial asymmetry (γ -unstable). The shape phase transitions between the three shapes have been considered by the introduction of the critical point symmetries E(5) [13] and X(5) [14]. The dynamical symmetry E(5) describe the phase transition between a spherical vibrator (U(5)) and γ-soft rotor (O(6)) and the X(5) for the critical point of the spherical to axially deformed (SU(3)) transition. Also the critical point in the phase transition from axially deformed to triaxial nuclei, called Y(5) has been analyzed [15].

The main objective of this study is to analyze the importance of the critical points in nuclear shapes changes. The paper is organized as follows. In sec. 2 we survey the framework of the GCM and the method to analyze the PES's in terms of the deformation variables β and γ. In section 3 we study the behavior of the critical point. In section 4 we present the numerical result for realistic case to even-even ^{238}U nucleus and give some discussions. Finally in section 5, the conclusions of this work are made.

2 Potential Energy Surfaces in Geometric Collective Model

We start by writing the GCM Hamiltonian in terms of irreducible tensor operators of collective coordinates α's and conjugate momenta π as:

$$\begin{aligned} H = \frac{1}{2B_2}[\pi\times\pi]^{(0)} + C_2[\alpha\times\alpha]^{(2)} \\ + C_3[[\alpha\times\alpha]^{(2)}\times\alpha]^{(0)} \\ + C_4[\alpha\times\alpha]^{(0)}[\alpha\times\alpha]^{(0)} \end{aligned} \quad (1)$$

where B_2 is the common mass parameter of the kinetic energy term and C_2, C_3 and C_4 are the three stiffness parameters of collective potential energy. They are treated as adjustable parameters which have to be determined from the best fit to the experimental data, level energies, B(E2) transition strengths and two-neutron separation energy. The corresponding collective potential energy surface (PES) is obtained by transforming the collective coordinate $a_{2\nu}$ into the intrinsic coordinate $a_{2\nu}$. To separate the three rotational degree of freedom one only has to set

$$\alpha_{2\mu} = \sum_{\nu} D^{*2}_{\mu\nu}(\omega) a_{2\nu}. \quad (2)$$

Since the body axes are principle axes, the products of inertia are zero, which implies that $a_{21} = a_{2-1} = 0$ and $a_{22} = a_{2-2}$. The two remaining variables a_{20} and a_{22}, to gather with Eulerian angles ω, would completely describe the system replacing the five $\alpha_{2\mu}$. However, there is rather more direct physical significance in the variables β and γ defined by

$$a_{20} = \beta\cos\gamma \quad (3)$$

$$a_{22} = \frac{1}{\sqrt{2}}\beta \sin\gamma \tag{4}$$

where β is a measure of the total deformation of the nucleus and γ indicate the deviations from axial symmetry. In terms of such intrinsic parameters, we have

$$[\alpha \times \alpha]^{(0)} = \frac{\beta^2}{\sqrt{5}} \tag{5}$$

$$[[\alpha \times \alpha]^{(2)} \times \alpha]^{(0)} = -\sqrt{\frac{2}{35}}\,\beta^3 \cos 3\gamma. \tag{6}$$

The PES belonging to the Hamiltonian (1) then reads

$$E(\beta,\gamma) = C_2 \frac{1}{\sqrt{5}}\beta^2 - C_3\sqrt{\frac{2}{35}}\beta^3 \cos 3\gamma + C_4 \frac{1}{5}\beta^4. \tag{7}$$

The values of β and γ are restricted to the intervals $0 \le \beta \le \infty$, $0 \le \gamma \le \pi/3$. In other words the $\pi/3$ sector of the $\beta\gamma$ plane is sufficient for the study of the collective PES's.

3 Critical Point Symmetries

Minimization of the PES with respect to β gives the equilibrium value β_m defining the phase of the system. $\beta_m = 0$ corresponding to the symmetric phase and $\beta_m \neq 0$ to the broken symmetry phase. Since γ enters the potential (7) only through the $\cos 3\gamma$ dependence in the cubic term, the minimization in this variable can be performed separately. The global minimum is either at $\gamma_m = 0(2\pi/3, 4\pi/3)$ for $C_3 > 0$ or at $\gamma_m = \pi/3(\pi, 5\pi/3)$ for $C_3 < 0$. The second possibility can be expected via changing the sign of the corresponding β_m and simultaneously setting $\gamma_m = 0$. The phase can be described as follows:

1. For $C_3^2 < \frac{14C_2|C_4|}{\sqrt{5}}$, phase with $\beta_m = 0$ interpreted as spherical shape.
2. For $C_3^2 < \frac{14C_2|C_4|}{\sqrt{5}}, C_3 > 0$, phase with $\beta_m > 0, \gamma_m = 0$ interpreted as prolate deformed shape.
3. For $C_3^2 < \frac{14C_2|C_4|}{\sqrt{5}}, C_3 < 0$, phase with $\beta_m > 0, \gamma_m = \pi/3$ interpreted as oblate deformed shape.

For β non-zero the first derivative of equation (7) must be zero and the second derivative positive. This gives

$$\begin{aligned} \frac{4}{5}C_4\beta^2 - 3\sqrt{\frac{2}{35}}\,C_3\beta^3\cos 3\gamma + \frac{2}{\sqrt{5}}\,C_2 &= 0 \\ \frac{12}{5}\,C_4\beta^2 - 6\sqrt{\frac{2}{35}}\,C_3\beta^3\cos 3\gamma + \frac{2}{\sqrt{5}}\,C_2 &> 0 \end{aligned} \tag{8}$$

The solution of equation (8), yields $\beta_\pm = \frac{3}{4}\sqrt{\frac{5}{14}}(1 \pm r)e$ with $r = \sqrt{1-d}$, $d = \frac{112}{9\sqrt{5}}\frac{C_2C_4}{C_3^2}$ and $e = \frac{C_3}{C_4}$.

The minimum values of the potential are

$$E(\beta) = -\frac{135}{50176}(r \pm 1)^3(3r \mp 1)f \tag{9}$$

with $f = \frac{C_3^4}{C_4^3}$.

For $d > 1$ there is only one minimum located at $\beta = 0$. For $0 < d < 1$, minima are present both at non-zero β and at $\beta = 0$, with the deformed minimum lower $0 < d < 8/9$ and the undeformed minimum lower for $8/9 < d < 1$. For $d < 0$, the potential has both a global minimum and a saddle point at non-zero β. For harmonic vibrator shape $C_3 = C_4 = 0$, this yields

$$E(\beta) = \frac{C_2}{\sqrt{5}}\beta^2, \qquad C_2 > 0. \tag{10}$$

For γ-unstable shape, the solution for$\beta \neq 0$ are obtained if we set $C_3 = 0$ in equation (8). Then equation (8) gives

$$\frac{4}{5}C_4\beta^2 + \frac{2}{\sqrt{5}}\,C_2 = 0$$

or

$$\beta = \pm\sqrt{\frac{-\sqrt{5}}{2}\frac{C_2}{C_4}} \simeq \pm 1.057\sqrt{\frac{-C_2}{C_4}};$$

this requires C_4 and C_2 to have opposite sign. Since C_4 must be positive for bound solutions C_2 must be negative in deformed γ-unstable shape. That is the spherical — deformed phase transition is generated by a change in sign of C_2, while the prolate-oblate phase is corresponding to changing the sign of C_3. For symmetric rotor one needs with both a deformed minimum in β and a minimum in γ, at $\gamma = 0$ for prolate or $\gamma = \pi/3$ for oblate. For prolate shape this requires $C_3 > 0$, such a potential has a minimum in β at $\beta_\pm$ equation (7). For $\gamma = 0$ (to study the β-dependence), and providing that $C_2 > 0$ and $C_3 > 0$, then the critical point is located at $C_3^2 < 14C_2|C_4|/\sqrt{5}$.

In Fig. (1a) a typical vibrator is given, the minimum of the PES is at $\beta = 0$ and therefore the ground state is spherical. In

Table 1: The GCM parameters for shape-phase transition (a) from vibrator to rotor (b) from rotor to γ-soft.

	C_2	C_3	C_4
set (a)	1	0	0
	-0.25	0.7	10
	-1	1	20
	-2.5	1.7	29
set (b)	-3	2	40
	-4.2	1.5	80
	-4.5	1	120
	-5	0	170

Fig. (1b) a typical axially deformed prolate is given, where the minimum it as $\beta \neq 0$ and the ground state is deformed. In Fig. (1c) a case of γ-unstable shape is illustrated. Fig. (2a) gives the PES's calculated with GCM as a function of the shape poor rotor β for shape phase transition from spherical to prolate deformed and in Fig. (2b) from rotor to γ-soft. The model parameters are listed in Table (1).

For simplicity we write equation (7) when $\gamma = 0$ in form

$$E(\beta) = A_2\beta^2 + A_3\beta^3 + A_4\beta^4. \quad (11)$$

The extremism structure of the PES depends only upon the value A_2 as summarized in Table (2) and Fig. (3). For $A_2 < 0$ the potential has both a global minimum and a saddle point at non-zero β. For $A_2 > 0$, minima are present at both $\beta \neq 0$ and $\beta = 0$ with the deformed minimum lower for $A_2 = 109.066$ and the undeformed minimum lower for $A_2 = 161.265$. For $A_2 = 22.6$ there is only one minimum located at $\beta = 0$.

4 Application to $^{238}_{92}$U

We applied the GCM to the doubly even actinide nucleus ^{238}U. The optimized model parameter was adjusted by fitting procedure using a computer simulated search program in order to reproduce some selected experimental excitation energies $(2_1^+, 4_1^+, 6_1^+)$ and the two neutron separation energies. The PES versus the deformation parameter β for ^{238}U is illustrated in Fig. (4). The figure show that ^{238}U exhibit a deformed prolate shape.

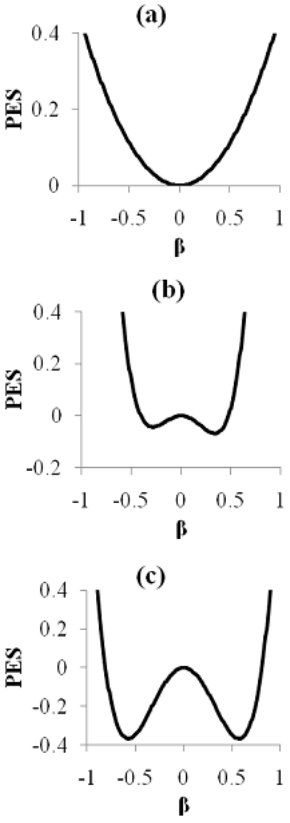

Fig. 1: Potential energy surface (PES's) in framework of GCM for three different shapes (a) harmonic vibrator shape ($C_2 = 1, C_3 = 0, C_4 = 0$) (b) strongly axially deformed prolate shape ($C_2 = -2.5, C_3 = 1.7, C_4 = 29$) (c) γ-unstable shape ($C_2 = -5, C_3 = 0, C_4 = 17$).

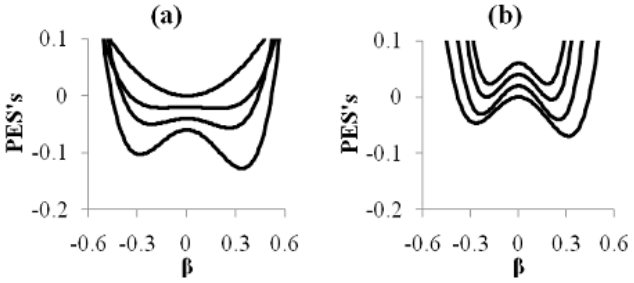

Fig. 2: Potential energy surface (PES's) in framework of GCM for two different shape transitions (a) from vibrator to rotor (b) from rotor to γ-soft rotor the set of parameters are listed in Table (1).

Table 2: Set of control parameters of the GCM to describe the nature of the critical points.

A_2	A_3	A_4
22.600	-1.120	0.234
66.412	-294.869	368.217
161.265	-935.148	1148.890
85.714	-573.709	960.000
109.066	-881.661	1603.589
0.000	-152.991	387.884
-15.581	-48.791	214.854
-22.098	-3.286	137.500

5 Conclusion

In this study we used the GCM to produce the PES's to investigate the occurrence of shape phase transitions. The critical point symmetries are obtained. The validity of the model is examined for ^{238}U. A fitting procedure was proposed to deforming the parameters of the geometric collective Hamiltonian for the axially symmetric deformed rotor.

Submitted on: September 21, 2013 / Accepted on: September 26, 2013

References

1. Iachello F. and Arima A. The Interacting Boson Model. Cambridge University Press, Cambridge, England, 1987.
2. Khalaf A.M. and Awwad T.M. A Theoretical Description of U(5)-SU(3) Nuclear Shape Transitions in the Interacting Boson Model. *Progress in Physics*, 2013, v. 1, 7–11.
3. Khalaf A.M. and Ismail A.M. The Nuclear Shape Phase Transitions Studied Within the Geometric Collective Model. *Progress in Physics*, 2013, v. 2, 51–55.

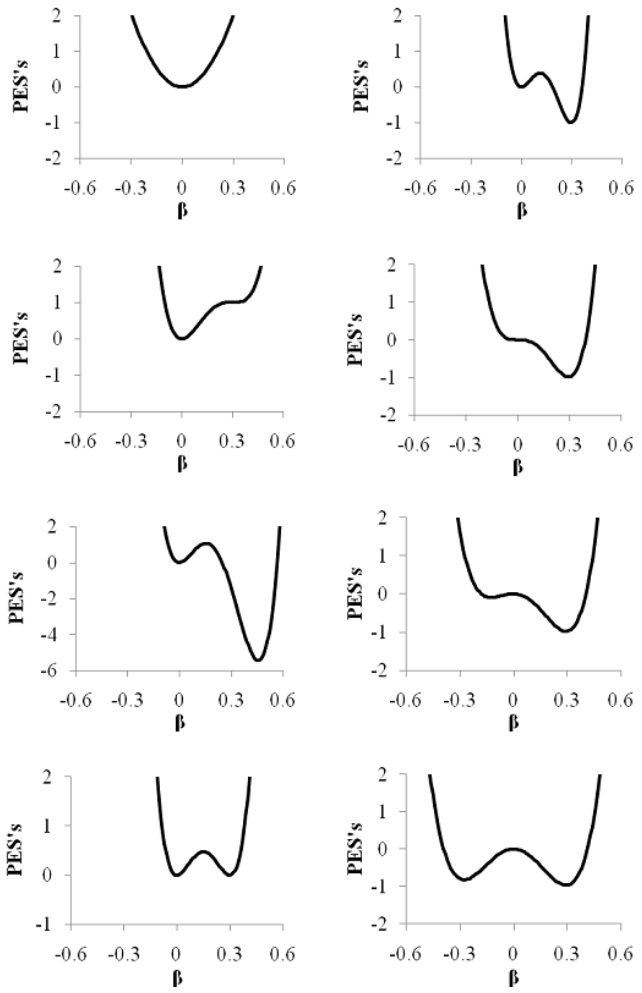

Fig. 3: Different shapes of PES's by varying the control parameters listed in Table (2).

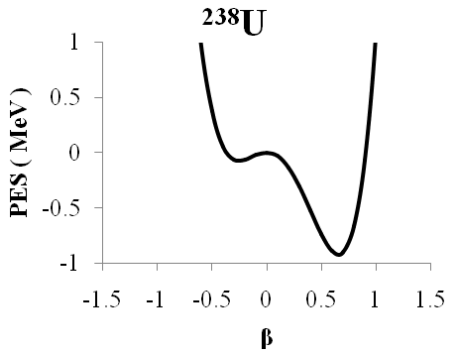

Fig. 4: The Potential energy surface (PES) as a function of deformation parameter β for ^{238}U and a cut through $\gamma = 0$ and $\gamma = \Pi/3$ are given with the parameters ($C_2 = -6.23928$, $C_3 = 18.63565$, $C_4 = 41.51437$).

4. Khalaf A.M. and Ismail A.M. Structure Shape Evolution in Lanthanide and Actinide Nuclei. *Progress in Physics*, 2013, v. 2, 98-104.

5. Zhang Y., Hau Z. and Liu Y.X. Distinguishing a First Order From a Second Order Nuclear Shape Phase Transition in The Interacting Boson Model. *Physical Review*, 2007, v. C76, 011305R–011308R.

6. Heinze S. et al. Evolution of spectral properties along the O(6)-U(5) transition in the interacting boson model. I. Level dynamics. *Physical Review*, 2006, v. C76, 014306–014316.

7. Liu Y.X., Mu L.Z. and Wei H. Approach to The Rotation Driven Vibrational to Axially Rotational Shape Phase Transition Along The Yrast Line of a Nucleus. *Physics Letters*, 2006, v. B633, 49–53.

8. Rosensteel G and Rowe D.J. Phase Transitions and Quasidynamical Symmetry in Nuclear Collective Models, III: The U(5) to SU(3) Phase Transition in the IBM. *Nuclear Physics*, 2005, v. A759, 92–128.

9. Casten R.F. and Zamfir N.V. Evidence for a Possible E(5) Symmetry in 134Ba. *Physical Review Letters*, 2000, v. 85, 3584–3586, Casten R.F. and Zamfir N.V. Empirical Realization of a Critical Point Description in Atomic Nuclei. *Physical Review Letters*, 2001, v. 87, 052503–052507.

10. Gneuss G., Mosel U. and Greiner W. A new treatment of the collective nuclear Hamiltonian. *Physics Letters*, 1969, v. B30, 397–399, Gneuss G., Mosel U. and Greiner W. On the relationship between the level-structures in spherical and deformed nuclei. *Physics Letters*, 1970, v. B31, 269–272.

11. Gneuss G. and Greiner W. Collective potential energy surfaces and nuclear structure. *Nuclear Physics*, 1971, v. A171, 449–479.

12. Troltenier D. Das Generalisierte Kollektivmodell. Frankfurt am Main, Germany, Report No. GSI-92-15, 1992.

13. Iachello F. Dynamic Symmetries at The Critical Point. *Physical Review Letters*, 2000, v. 85, 3580–3583.

14. Iachello F. Analytic Prescription of Critical Point Nuclei in a Spherical Axially Deformed Shape Phase Transtion. *Physical Review Letters*, 2001, v. 87, 052502–052506.

15. Iachello F. Phase Transitions in Angle Variables. *Physical Review Letters*, 2003, v. 91, 132502–132505.

Dynamical 3-Space: Observing Gravitational Wave Fluctuations and the Shnoll Effect using a Zener Diode Quantum Detector

David P. Rothall and Reginald T. Cahill

School of Chemical and Physical Sciences, Flinders University, Adelaide 5001, Australia
E-mail: David.Rothall@flinders.edu.au, Reg.Cahill@flinders.edu.au

Shnoll has investigated the non-Poisson scatter of measurements in various phenomena such as biological and chemical reactions, radioactive decay, photodiode current leakage and germanium semiconductor noise, and attributed the scatter to cosmophysical factors. A more recent model of reality leads to a description of space which is dynamic and fractal and exhibits reverberation effects, and which offers an explanation for the scatter anomaly. This paper is a correction to the work presented earlier which used data from a RF coaxial cable experiment, but had insufficient timing resolution to show the full effects of what Shnoll observed. Here we report a different way to produce the effects through studying current fluctuations in reverse biased zener diode gravitational wave detector with better timing resolution. The current fluctuations have been shown to be caused by dynamical 3-space fluctuations/turbulence, namely gravitational waves.

1 Introduction — Shnoll effect

For over half a century Simon Shnoll has studied the non-Poisson scatter anomalies in various phenomena such as biological and chemical reactions, radioactive decay, photodiode current leakage and germanium semiconductor noise. An example of this is Fig. 1, which shows a layered histogram of some 352,980 successive measurements of the α decay rate of a ^{239}Pu source [1] undertaken by Shnoll between May 28 — June 01, 2004. The layer lines taken every 6000 successive measurements show a fine structure which builds up over time instead of cancelling out as in the case of a typical random or Poisson distribution. This suggests that the radioactivity of ^{239}Pu takes on discrete (preferred) values, and is not completely random. It should be clarified here that the effects Shnoll studied in depth were those concerning the shapes of histograms taken using fewer measurements (usually between 60 and 100) instead of that of the non-Poisson scatter of measurements taken over a much larger data set as discussed in our previous paper [2]. Shnoll found that the shapes of histograms from either the same or different experiments correlated via both absolute (same time) and local (time delay due to Earth's rotation) time synchronism and that the phenomenon causing this had a fractal nature. Shnoll attributed the cause of this to cosmophysical factors, i.e. inhomogeneities in the "space-time continuum" [1, 4]. These inhomogeneities are "caused by the movement of an object in the inhomogeneous gravitational field", e.g. as the Earth rotates/orbits the Sun, as the moon orbits the Earth etc. While these inhomogeneities were not characterised by Shnoll there is a remarkable amount of evidence supporting this conclusion [1]. An experiment which studied the phase difference of two RF signals traveling through two coaxial cables [5] was reported to show similar non-Poisson characteristics to that of ^{239}Pu decay shown in Fig. 1.

An alternative model of reality leads to a description of space which is dynamic and fractal. The RF coaxial cable propagation experiment can be used to characterise gravitational waves. However the resolution of the data in the coaxial cable experiment proved to be insufficient to study changes in histogram shapes. It is reported here that a newer technique which studies the non-Poisson characteristics of the current fluctuations in zener diodes and may be used to study gravitational waves. This technique allows for faster recording of data (every second instead of every 5 seconds) and used much higher digital resolution.

2 Dynamical 3-space

An alternative explanation of the Shnoll effect has been proposed using the dynamical 3-space theory; see *Process Physics* [6]. This arose from modeling time as a non-geometric process, i.e. keeping space and time as separate phenomena, and leads to a description of space which is dynamic and fractal. It uses a uniquely determined generalisation of Newtonian Gravity expressed in terms of a velocity field $\boldsymbol{v}(\boldsymbol{r}, t)$, defined relative to an observer at space label coordinate $\boldsymbol{r}$, rather than the original gravitational acceleration field. The dynamics of space in the absence of vorticity, $\nabla \times \boldsymbol{v} = \boldsymbol{0}$, becomes*

$$\nabla\cdot\left(\frac{\partial \boldsymbol{v}}{\partial t} + (\boldsymbol{v}\cdot\nabla)\boldsymbol{v}\right) + \frac{5\alpha}{4}\left((trD)^2 - tr(D^2)\right) + ... = -4\pi G\rho, \quad (1)$$

where $D_{ij} = \partial v_i/\partial x_j$, and $\rho = \rho(\boldsymbol{r}, t)$ is the usual matter density. The 1st term involves the Euler constituent acceleration, while the $\alpha-$term describes the self interaction of space. Laboratory, geophysical and astronomical data suggest that α is

*The α term in (1) has recently been changed due to a numerical error found in the analysis of borehole data. All solutions are also altered by these factors. (1) also contains higher order derivative terms — see [7] .

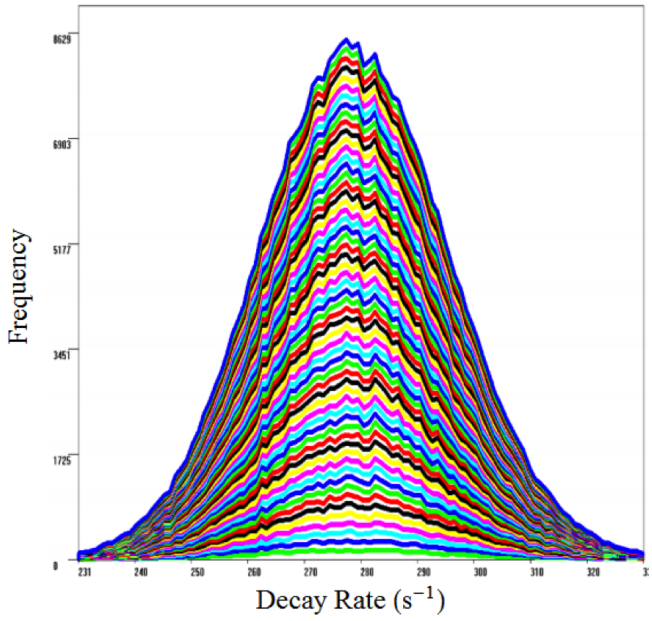

Fig. 1: Non-Poisson distribution of 352,980 measurements of ^{239}Pu α decay by Shnoll performed in 2004 (Fig. 2-2 of [1]). The layered histograms are taken every 6000 measurements. The x-axis denotes the number of decay events per second and the y-axis is the frequency of measurements.

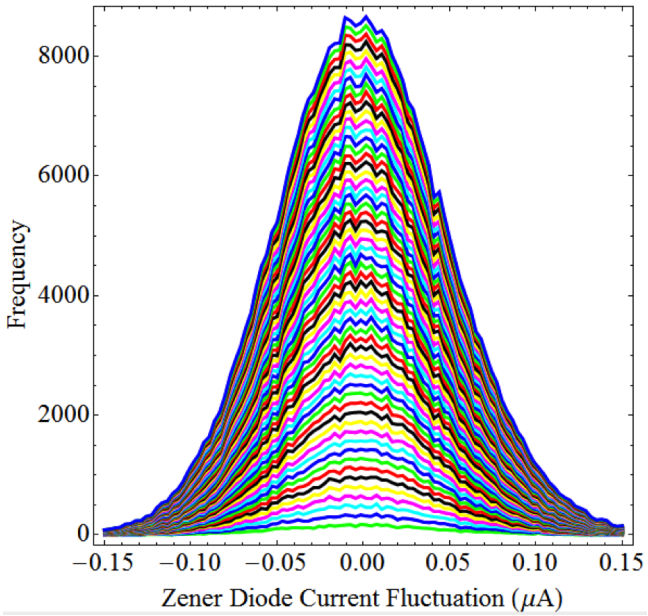

Fig. 2: Non-Poisson distribution of 376,101 measurements of zener diode current fluctuation (μA) observed from 20 — 27 Aug. 2013 in Adelaide. The layered histograms are taken every 6100 measurements to show a comparison with that of Fig.1.

the fine structure constant $\approx 1/137$. This velocity field corresponds to a space flow which has been detected in numerous experiments. In the spherically symmetric case and in the absence of matter $\rho = 0$, (1) contains solutions for black holes (spatial inflows) and an expanding universe (Hubble expansion) along with that for black holes embedded in an expanding universe [7]. Eqn.(1) also contains solutions for the inflow of space into a matter density. Perturbing the spatial inflow into matter (i.e. simulating gravitational waves) has shown to produce reverberations in which the wave generates trailing copies of itself [8]. This reverberation effect is caused by the non-linear nature of the flow dynamics evident in (1).

3 Zener diode quantum gravitational wave detector

A gravitational wave detector experiment performed in March 2012 measured the travel time difference of two 10MHz radio frequency (RF) signals propagating through dual coaxial cables [5]. This technique exploited the absence of the Fresnel drag effect in RF coaxial cables, at sufficiently low frequencies. This permitted the detection of gravitational waves at 1st order in v/c using one clock. The timing resolution of the results were however insufficient to study the effects Shnoll investigated, namely the changes in the histogram shapes over time.

A more recent experiment uses the current fluctuations in a reverse biased zener diode circuit. The circuit diagram is shown in Fig. 3. This detector exploits the discovery that the electron tunnelling current is not random, but caused by gravitational waves; namely fluctuations/turbulence in the passing dynamical 3-space [3]. A Fast Fourier Transform of the zener diode data was taken to remove low frequency artefacts, and then a histogram taken of the resultant 376,101 measurements (after inverse FFT) to generate the layered histogram plot shown in Fig. 2. Layer lines are inserted every 6100 measurements to show a comparison with the Shnoll plot in Fig. 1. Fig. 2 is remarkably comparable to Fig. 1, showng that the Shnoll effect is also present in zener diode experiments. The structure observed appears to build up over time instead of cancelling out and is also found to persist regardless of the time scale used for the phase difference, suggesting that the phenomenon causing this has a fractal nature as depicted in Fig.4. If this is indeed caused by a dynamical and fractal 3-space then the persisting structure observed in Figs. 1 and 2 correspond to regions of space passing the Earth that have preferred/discrete velocities, and not random ones, as randomly distributed velocities would result in a Poisson distribution, i.e. no features. A likely explanation for this is that the gravitational waves propagating in the 3-space inflow of the Earth or Sun could become phase locked due to the relative locations of massive objects [8]. This would cause reverberation effects, i.e. regions of space which have the same speed and direction, which then repeat over time. The reverberations would be detectable in many other experiments such as EM anisotropy, radiation decay, semiconductor noise generation etc. and could in the future be used to further characterise the dynamics of space.

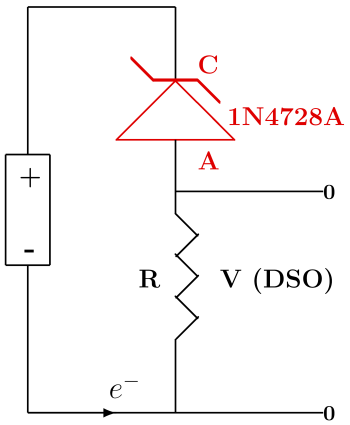

Fig. 3: Circuit of Zener Diode Quantum Gravitational Wave Detector, showing 1.5 AA battery, 1N4728A zener diode operating in reverse bias mode, and having a Zener voltage of 3.3 V, and resistor 10KΩ. Voltage V across resistor is measured and used to determine the space driven fluctuating tunneling current through the zener diode, [3]. Data is shown in Fig.2.

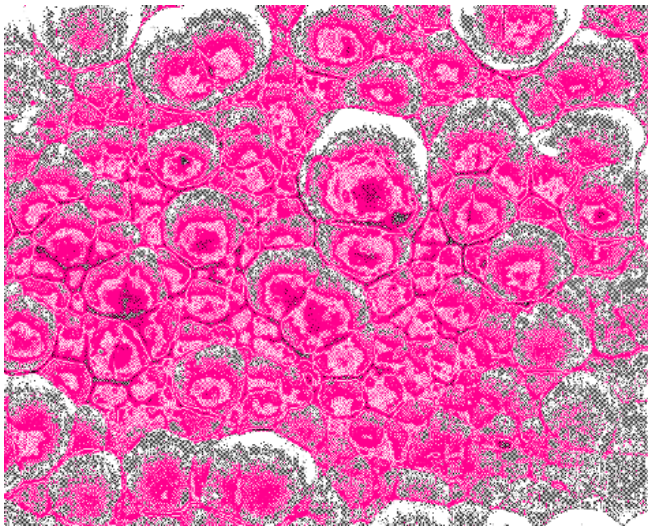

Fig. 4: Representation of the fractal wave data as revealing the fractal textured structure of the 3-space, with cells of space having slightly different velocities and continually changing, and moving wrt the earth with a speed of 500 km/s.

4 Conclusion

The data from a zener diode quantum gravitational wave experiment displays the non-Poisson characteristics Shnoll observed previously in radioactivity experiments. It is suggested that these two experiments (along with other work by Shnoll) are caused by the fractal nature of space, together with the reverberation effect from gravitational waves, as predicted by the Dynamical 3-Space theory.

5 Acknowledgments

Special thanks to Professor Simon Shnoll for permission to use data from his work — see ref [1] for details. Thanks also to Prof Simon Shnoll and Dr Dmitri Rabounski for drawing to our attention the limited digital resolution used in [2]. This report is from the Flinders University Gravitational Wave Detector Project, funded by an Australian Research Council Discovery Grant: *Development and Study of a New Theory of Gravity*.

Submitted on November 11, 2013 / Accepted on November 14, 2013

References

1. Shnoll S.E. Cosmophysical Factors in Stochastic Processes. American Research Press, Rehoboth, New Mexico, USA, 2012. Available from Progress in Physics website.
2. Rothall D.P. and Cahill R.T. Dynamical 3-space: gravitational wave detection and the Shnoll effect, *Progress in Physics*, 2013, v. 4, 44–47.
3. Cahill R.T. Nanotechnology quantum detectors for gravitational waves: Adelaide to London correlations observed. *Progress in Physics*, 2013, v. 4, 57–62.
4. Shnoll, S.E., Zenchenko T.A., Zenchenko K.I., Pozharskii E.V., Kolombet V.A. and Konradov A.A. Regular variation of the fine structure of statistical distributions as a consequence of cosmophysical agents. *Phys. Usp.*, 2000, v. 43(2), 205–209.
5. Cahill R.T. Characterisation of low frequency gravitational waves from dual RF coaxial-cable detector: fractal textured dynamical 3-space. *Progress in Physics*, 2012, v. 3, 3–10.
6. Cahill R.T. Process Physics: From Information Theory to Quantum Space and Matter. Nova Science Pub., New York, 2005.
7. Rothall D.P. and Cahill R.T. Dynamical 3-space: black holes in an expanding universe. *Progress in Physics*, 2013, v. 4, 25–31.
8. Cahill R.T. and Deane S.T. Dynamical 3-space gravitational waves: reverberation effects. *Progress in Physics*, 2013, v. 2, 9–11.

Kepler-47 Circumbinary Planets obey Quantization of Angular Momentum per Unit Mass predicted by Quantum Celestial Mechanics (QCM)

Franklin Potter

Sciencegems.com, 8642 Marvale Drive, Huntington Beach, CA 92646 USA. E-mail: frank11hb@yahoo.com

The Kepler-47 circumbinary system has three known planets orbiting its binary star barycenter and therefore can provide a precision test of the Quantum Celestial Mechanics (QCM) prediction of the quantization of angular momentum per unit mass in all gravitationally bound systems. Two of the planets are in the Habitable Zone (HZ), so system stability can be a primary concern. QCM may be a major contributor to the stability of this system.

1 Introduction

We report another precision test of quantum celestial mechanics (QCM) in the Kepler-47 circumbinary system that has three planets orbiting its two central stars. QCM, proposed in 2003 by H.G. Preston and F. Potter [1] as an extension of Einstein's general theory of relativity, predicts angular momentum per unit mass quantization states for bodies orbiting a central mass in all gravitationally bound systems with the defining equation in the Schwarzschild metric being

$$\frac{L}{\mu} = m\,\frac{L_T}{M_T}\,. \tag{1}$$

Here μ is the mass of the orbiting body with orbital angular momentum L and M_T is the total mass of the bound system with total angular momentum L_T. We determine that the quantization integers m are 4, 6, and 7, for the three circumbinary planets 47-b, -d, -c, respectively, with a linear regression fit $R^2 = 0.9993$. Note that in all systems we have considered, we assume that the orbiting bodies have been in stable orbits for at least a 100 million years.

In other two-star systems with one or two circumbinary planets, the two stars contributed more than 95% of the total angular momentum of the system. In Kepler-47, the three known planets are contributing at least 25% of the angular momentum, a significant fraction, so Kepler-47 provides an additional test of QCM.

As we determined in the paper cited above, in the Solar System the Oort Cloud dominates the total angular momentum, its contribution being nearly 60 times the angular momentum of the planets, but the value has large uncertainty. In the numerous multi-planetary systems around a single star for which we have checked the QCM angular momentum quantization restriction [2], not only do the planetary orbits contribute much more angular momentum than the star rotation, but also each was determined to require additional angular momentum contributions from more planets and/or the equivalent of an Oort Cloud.

We find also that Kepler-47 could have more angular momentum contributions beyond the angular momentum sum of the binary stars and the three planets.

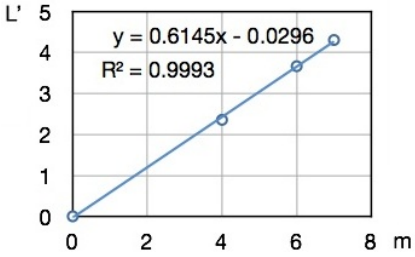

Fig. 1: Kepler-47 System m values predicted by QCM.

2 Results

W.F. Welsh, J.A. Orosz, et al. [3,4] have recently reported the properties of the Kepler-47 system:

- Stars A and B have masses 1.04 ± 0.06 $M_\odot$ and 0.36 $M_\odot$ with orbital period 7.45 days.
- Planet 47-b has mass < $2M_{Jup}$, orbital period 49.53 days and orbital eccentricity $e < 0.035$.
- Planet 47-c has mass < $28M_{Jup}$, orbital period 303.1 days and orbital eccentricity $e < 0.2$.
- Planet 47-d has orbital period 187.3 days, unknown eccentricity, and unknown mass value.

Planet-c is definitely within the Habitable Zone (HZ) and so is planet 47-d. As the authors state, Kepler-47 establishes that planetary systems can form and persist in the chaotic environment close to binary stars as well as have planets in the HZ around their host stars.

In order to use the angular momentum condition, one assumes that the orbiting body is at or near its QCM equilibrium orbital radius r and that the orbital eccentricity ϵ is low so that our nearly circular orbit approximation leading to the quantization equation holds true. Therefore, the L of the orbiting body will agree with its Newtonian value $L = \mu\sqrt{GM_T r(1-\epsilon^2)}$.

In Fig. 1 is shown a plot of $L' = L/\mu$ versus m for the three known planets in the Kepler-47 system. The circles about the data points contain the uncertainty bars for L'. The slope b of the line in this plot is used to predict the system's total angular momentum $L_T = bM_T$ multiplied by 10^{15} kg-m^2/s.

The QCM predicted value of 17.7×10^{44} kg-m^2/s is much larger than the estimated upper value of 12×10^{44} kg-m^2/s from the five bodies in orbit about the barycenter. Therefore, QCM predicts additional sources of angular momentum for this Kepler-47 system.

What are possible additional sources for the QCM predicted total angular momentum? There could be massive bodies at $m = 3, 5, 8, 9, \ldots$ However, massive bodies with sufficient orbital angular momentum at either $m = 3$ or $m = 5$ would have been detected already by their perturbation effects on the known planets, so the additional planetary angular momentum must be exterior to planet 47-c, i.e., will have $m > 7$. Perhaps new sources will be detected in the near future to provide another check on the QCM quantization condition.

3 Conclusions

The Kepler-47 system provides further evidence that angular momentum has a primary role in gravitationally bound systems at all scale sizes, particularly in determining the spacings of planetary orbits in solar systems, of satellites of planets [5], of planets in circumbinary systems, as well as determining physical properties of galaxies, clusters of galaxies, and the Universe.

Although the three known planets in Kepler-47 have an excellent fit to the QCM quantization condition, further orbiting bodies are predicted that could provide an additional test when they are detected. If they are located at orbital radii that do not agree with acceptable values, QCM will be challenged to explain the discrepancies.

Acknowledgements

The author thanks Sciencegems.com for encouragement and financial support.

Submitted on November 16, 2013 / Accepted on November 18, 2013

References

1. Preston H. G., Potter F. Exploring Large-scale Gravitational Quantization without h-bar in Planetary Systems, Galaxies, and the Universe. arXiv: gr-qc/030311v1.
2. Potter F. Multi-planet Exosystems All Obey Orbital Angular Momentum Quantization per Unit Mass predicted by Quantum Celestial Mechanics (QCM). *Progress in Physics*, 2013, v. 3, 60–61.
3. Welsh W. F., Orosz J. A., Carter J. A., Fabrycky D. C., and the *Kepler* Team. Recent Kepler Results On Circumbinary Planets. arXiv: 1308.6328.
4. Orosz J. A. The Confirmation of a Third Planet in the Kepler-47 Circumbinary System. http://nexsci.caltech.edu/conferences/KeplerII/agenda.shtml.
5. Potter F. Pluto Moons exhibit Orbital Angular Momentum Quantization per Mass. *Progress in Physics*, 2012, v. 4, 3–4.

Observed Gravitational Wave Effects: Amaldi 1980 Frascati-Rome Classical Bar Detectors, 2013 Perth-London Zener-Diode Quantum Detectors, Earth Oscillation Mode Frequencies

Reginald T. Cahill

School of Chemical and Physical Sciences, Flinders University, Adelaide 5001, Australia. E-mail: Reg.Cahill@flinders.edu.au

Amaldi *et al* in 1981 reported two key discoveries from the Frascati and Rome gravitational wave cryogenic bar detectors: (a) Rome events delayed by within a few seconds to tens of seconds from the Frascati events, and (b) the Frascati Fourier-analysed data frequency peaks being the same as the earth oscillation frequencies from seismology. The time delay effects have been dismissed as being inconsistent with gravitational waves having speed c. However using data from zener diode quantum detectors, from Perth and London, for January 1-3, 2013, we report the same effects, and in excellent agreement with the Amaldi results. The time delay effects appear to be gravitational wave reverberations, recently observed, and for gravitational wave speeds of some 500 km/s, as detected in numerous experiments. We conclude that the Amaldi *et al.* discoveries were very significant.

1 Introduction

On the basis of data from the new nanotechnology zener-diode quantum gravitational wave detectors [1] it is argued that the wave effects detected in 1980 by Amaldi *et al* [2,3], using two cryogenic bar detectors, located in Frascati and Rome, were genuine gravitational wave effects, together with earth oscillation effects, although not gravitational waves of the expected form.

The speed and direction of gravitational waves have been repeatedly detected using a variety of techniques over the last 125 years, and have a speed of some 500 km/s coming from a direction with RA $\sim$ 5 hrs, Dec $\sim 80^0$. These waves appear to be of galactic origin, and associated with the dynamics of the galaxy and perhaps the local cluster. This speed is that of the dynamical 3-space, which appears to have a fractal structure, and the significant magnitude waves are turbulence/fractal structure in that flowing space. The detection techniques include gas-mode Michelson interferometers, RF coaxial cable EM speed measurements, RF coaxial-cable - optical fiber RF/EM speed measurements, EM speed measurements from spacecraft Earth-flyby Doppler shifts, zener-diode quantum detectors, within Digital Storage Oscilloscopes, and in so-called Random Event Generators (REG) [1, 4, 5]. These zener diode devices have detected correlations between Adelaide and London, and between Perth and London, with travel time delays from 10 to 20 seconds, and with significant reverberation effects [1, 6]. The speed of some 500 km/s has also been observed as a time delay of some 500 ns in table-top zener-diode quantum detectors, separated by 25 cm in a S to N direction. The zener-diode gravitational wave quantum detectors operate by the process of the 3-space wave turbulence causing the quantum to classical transition, i.e. spatial localisation of the electron wave functions tunneling through a 10 nm quantum barrier, when the diode is operated in reverse bias. The earlier techniques rely on detecting EM radiation anisotropy.

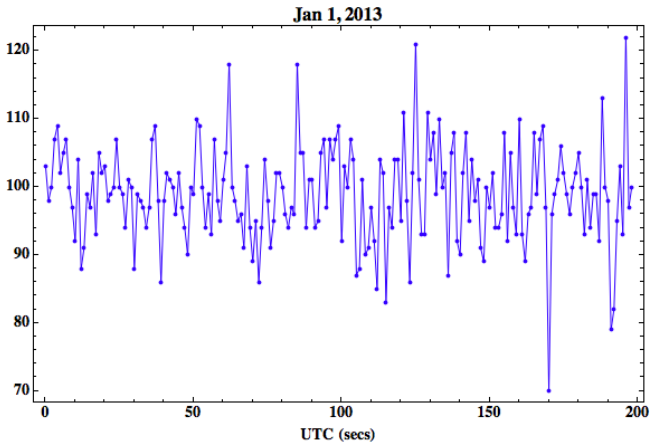

Fig. 1: Perth zener-diode quantum detector (REG) data, for January 1, 2013. The data points are at 1 s intervals. The data shows strong peaks at 5 - 30 s intervals, related to the reverberation effect [6]. This appears to be the time-delay effect detected between the Frascati and Rome cryogenic gravitational wave bar detectors [2, 3].

2 The Amaldi Frascati Rome gravitational wave detectors

Data was collected with two cryogenic resonant gravitational wave antennas operated simultaneously in Rome and Frascati. Coincidences were detected with pulses lasting about 1 second, and travel times differing from one second to twenty seconds ($\pm$0.5 s), with the NW Rome signal delayed relative to the Frascati events. These events were dismissed as gravi-

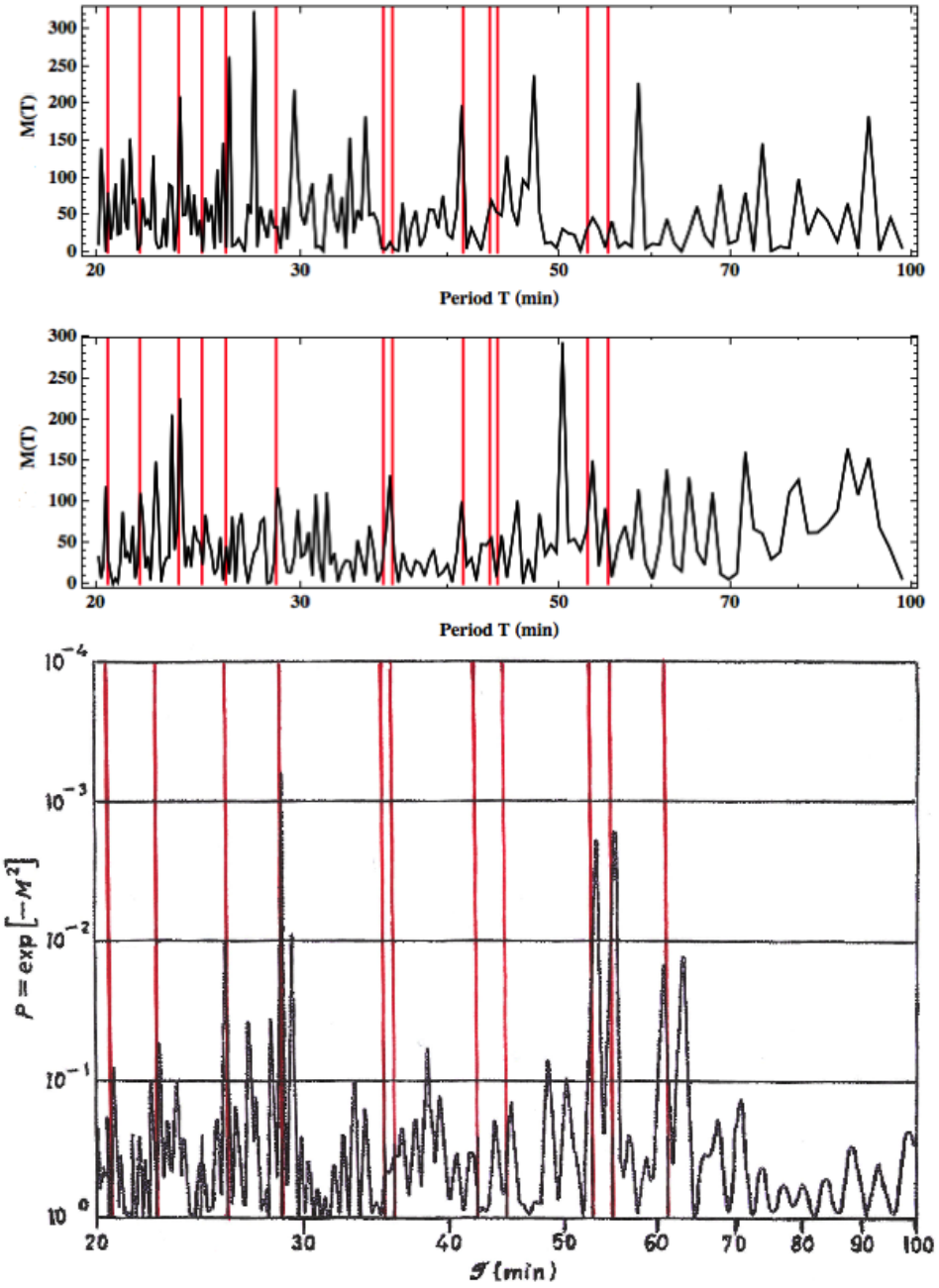

Fig. 2: Top: Power spectrum from Zener Diode detector in Perth, Jan 1-3, 2013. Middle: Power spectrum from Zener Diode detector in London, Jan 1-3, 2013. Bottom: Power spectrum from Frascati bar detector data, May 6-7, 1980, adapted from Amaldi *et al* [3]. Vertical lines (red) show various earth vibration periods, determined by seismology [9]. $M(T) = |F(T)|^2$ is the power spectrum, expressed as a function of period T, where $F(T)$ is the Fourier transform of the data time series. A 200 sec interval of the Perth data is shown in Fig.1. The spectra from all detectors show the same low frequency peaks, but with differing intensities. The peaks at 53.1 and 54.1 min equal the ${}_0S_2^{+1}$ and ${}_0S_2^{-1}$ Earth vibration modes.

tational wave events as the travel times, for the 20 km separation, far exceeded that expected if one assumes that gravitational waves travel at speed c, predicting travel times ∼0.1 ms. As well frequency analysis of the data revealed strong peaks at frequencies coinciding with known vibration frequencies of the earth, see bottom plot of Fig. 2. Amaldi *et al.* considered several mechanisms for the detection of such frequencies: (i) various instrumental couplings to the earth vibrations, (ii) gravitational field variations caused by a terrestrial source. However the very same results are obtained with the zener-diode quantum gravitational wave detectors.

3 Zener diode detectors

In [1] the discovery of the nanotechnology zener diode detection effect for gravitational waves was reported. This was established by detecting times delays between wave forms of 10-20 seconds for travel times Adelaide to London, and Perth to London, with that travel time variation following the earth's rotation with respect to the RA and Dec that had been reported in earlier experiments [4,5], and which displayed the sidereal effect, *viz* the earth time of the earth rotation phase was essentially fixed relative to sidereal time, i.e. the flow direction was fixed relative to the stars.

The zener diode detectors first used are known as Random Number Generators (RNG) or Random Event Generators (REG). There are various designs available from manufacturers, and all claim that these devices manifest hardware random quantum processes, as they involve the quantum to classical transition when a measurement, say, of the quantum tunneling of electrons through a nanotechnology potential barrier, ∼10 nm thickness, is measured by a classical/macroscopic system. According to the standard interpretation of quantum theory, the collapse of the electron wave function to one side or the other of the barrier, after the tunneling produces a component on each side, is purely a random event, internal to the quantum system. However that interpretation had never been tested experimentally, until [1]. Data from two REGs, located in Perth and London, was examined. The above mentioned travel times were then observed. The key features being a speed of ∼500 km/s, and strong reverberation effects, see Fig. 1.

This discovery revealed that current fluctuations through a zener diode in reverse bias mode are not random, and data from collocated zener diodes showed almost identical fluctuations [1]. Consequently the zener diode detectors can easily be increased in sensitivity by using zener diodes in parallel, with the sensitivity being proportional to the number of diodes used, see circuit diagram in [1]. That the quantum to classical transition, i.e. "collapse of the wave function", is induced by 3-space fluctuations, has deep implications for our understanding of quantum phenomena.

Using data from REG's located in Perth and London, for Jan. 1-3, 2013, and then doing a Fourier transform frequency analysis, we obtain the spectrum in the top two plots in Fig. 2. The unfiltered power spectra from the two REGs show remarkable similarity to each other, and to the spectrum from the Frascati data. Again the dominant frequencies correspond to known earth vibration frequencies [9], although there are long-period oscillations, common to all detectors, that are not known earth frequencies.

This new data shows that the time delays observed between Frascati and Rome are to be expected, because of the strong reverberation effects seen in the zener diode detector data. However the occurrence of the earth vibration frequencies is intriguing, and reveals new physics. Unlike the bar detectors it is impossible for any physical earth movement to mechanically affect the zener diodes, and so all detectors are responding to dynamical space fluctuations caused by the oscillations of the matter forming the earth. The key questions are: What causes this ongoing activation of the earth modes? Are they caused by earthquakes or by the fractal 3-space waves exciting the earth modes?

4 Conclusions

The discovery of the quantum detection of gravitational waves, showing correlations between well separated locations, that permitted the absolute determination of the 3-space velocity of some 500 km/s, in agreement with the speed and direction from a number of previous analyses, including in particular the NASA spacecraft Earth-flyby Doppler shift effect. This discovery enables a very simple and cheap nanotechnology zener-diode quantum gravitational wave detection technology, which will permit the study of various associated phenomena, such as solar flares, coronal mass ejections, earthquakes, eclipse effects, moon phase effects, non-Poisson fluctuations in radioactivity [7, 8], and other rate processes, and variations in radioactive decay rates related to distance of the earth from the Sun, as the 3-space fluctuations are enhanced by proximity to the sun. As an example of these possibilities we have confirmed that the Amaldi *et al* bar detectors did indeed detect gravitational wave events in 1980, but not of the form commonly expected, in particular gravitational waves do not travel at speed c, and there is no experimental or observational evidence supporting that claim.

5 Acknowledgements

This report is from the Flinders University Gravitational Wave Detector Project, Australian Research Council Discovery Grant: *Development and Study of a New Theory of Gravity*. Thanks to GCP and its director Dr Roger Nelson for the availability of extensive and valuable data from the REG international network: http://teilhard.global-mind.org/. Giovanni B. Bongiovanni, Turin, raised the earth vibration frequency effect observed using a zener diode detector, and also confirmed the strong correlations between collocated detectors.

Submitted on November 18, 2013 / Accepted on November 20, 2013

References

1. Cahill R. T. Nanotechnology quantum detectors for gravitational waves: Adelaide to London correlations observed. *Progress in Physics*, 2013, v. 4, 57–62.
2. Amaldi E., Coccia E., Frasca S., Modena I., Rapagnani P., Ricci F., Pallottino G. V., Pizzella G., Bonifazi P., Cosmelli C., Giovanardi U., Iafolla V., Ugazio S., and Vannaroni G. Background of gravitational-wave antennas of possible terrestrial origin — I. *Il Nuovo Cimento*, 1981, v. 4C (3), 295–308.
3. Amaldi E., Frasca S., Pallottino G. V., Pizzella G., Bonifazi P. Background of gravitational-wave antennas of possible terrestrial origin — II. *Il Nuovo Cimento*, 1981, v. 4C (3), 309–323.
4. Cahill R. T. Combining NASA/JPL one-way optical-fiber light-speed data with spacecraft Earth-flyby Doppler-shift data to characterise 3-space flow. *Progress in Physics*, 2009, v. 4, 50–64.
5. Cahill R. T. Characterisation of low frequency gravitational waves from dual RF coaxial-cable detector: fractal textured dynamical 3-space. *Progress in Physics*, 2012, v. 3, 3–10.
6. Cahill R. T. and Deane S.T. Dynamical 3-space gravitational waves: reverberation effects, *Progress in Physics*, 2013, v. 2, 9–11.
7. Shnoll S. E. Cosmophysical Factors in Stochastic Processes. American Research Press, Rehoboth, New Mexico, USA, 2012.
8. Rothall D. P. and Cahill R. T. Dynamical 3-Space: Observing Gravitational Wave Fluctuations and the Shnoll Effect using a Zener Diode Quantum Detector. *Progress in Physics*, 2014, v. 10 (1), 16–18.
9. Masters T. G. and Widmer R. Free oscillations: frequencies and attenuations. In: Ahrens I. J., Ed. Global Earth Physics, A Handbook of Physical Constants, AGU, 1995, 104–125.

LETTERS TO PROGRESS IN PHYSICS

Florentin Smarandache: A Celebration

Dmitri Rabounski

E-mail: rabounski@ptep-online.com

We celebrate Prof. Florentin Smarandache, the Associate Editor and co-founder of *Progress in Physics* who is a prominent mathematician of the 20th/21th centuries. Prof. Smarandache is most known as the founder of neutrosophic logic, which is a modern extension of fuzzy logics by introducing the neutralities and denials (such as "neutral A" and "non-A" between "A" and "anti-A"). He is also known due to his many discoveries in the filed of pure mathematics such as number theory, set theory, functions, etc. (see many items connected with his name in *CRC Encyclopedia of Mathematics*). As a multi-talented person, Prof. Smarandache is also known due to his achievements in the other fields of science, and also as a poet and writer. He still work in science, and continues his creative research activity.

Florentin Smarandache (born on December 10, 1954) — polymath, professor of mathematics, scientist, poet and writer (originally writting in Romanian, French, and English). He is a US citizen. He lives in the United States.

Florentin Smarandache was born in Bălceşti, a small village in province Vâlcea, Romania. His ancestors from father's side came to Romania from Greece, several generations before, but saved their Greek family name (which was romanized) over the centuries. He was the only child in the family.

In 1979, Florentin Smarandache was graduated from the Department of Mathematics at the University of Craiova (Romania). In 1997, the State University of Moldova at Kishinev bestowed upon him the PhD degree in mathematics. Then he continued his post-doctoral studies at various American Universities (such as University of Texas at Austin, University of Phoenix, etc.).

In the USA he worked as a software engineer for Honeywell (1990-1995), then as Adjunct Professor for Pima Community College (1995-1997). In 1997 he joined to the University of New Mexico, Gallup Campus, as Adjunct Professor. Then he was promoted to Associate Professor of Mathematics (2003), and to Full Professor (2008). During 2007-2009 he was the Chair of Department of Mathematics and Sciences.

During Ceausescu's dictatorship in Romania, Florentin Smarandache was enrolled into a conflict with the Romanian authorities. In 1986 he claimed a hungry strike for being refused to attend the International Congress of Mathematicians at the University of Berkeley. Then he published an open letter in the Notices of the American Mathematical Society, for the freedom of circulating of scientists. He thus became a political dissident in Romania. As a consequence, he was faired from the academic job, and survived during two years from private tutorship. Dr. Olof G. Tandberg, Foreign Secretary of Swedish Royal Academy, supported him by phone talking from Bucharest.

Not being allowed to publish, he tried to get his manuscripts out of the country through the French School of Bucharest and tourists, but for many of them he lost track. Finally, in September 1988, Florentin Smarandache escaped from Romania, then stayed for almost two years in Turkey, in a refugee camp. Here he kept in touch with the French Cultural Institutes that facilitated him the access to books and rencontres with personalities. Before leaving the country he buried some of his manuscripts in a metal box in his parents vineyard, near a peach tree, that he retrieved four years later, after the 1989 Revolution, when he returned for the first time to his native country. Other manuscripts, that he tried to mail to a translator in France, were confiscated by the secret police and never returned. He wrote hundreds of pages of the diaries about his life under the Romanian dictatorship, about

Prof. Florentin Smarandache

his being as a cooperative teacher in Morocco ("Professor in Africa", 1999), in the Turkish refugee camp ("Escaped... Diary From the Refugee Camp", vol.1, vol.2, 1994, 1998). In March 1990, Florentin Smarandache emigrated to the United States.

Florentin Smarandache is also known as the founder of "paradoxism" (established in 1980). This is the literary movement which has many followers in the world. Paradoxism is based on an excessive use of antitheses, antinomies, contradictions, paradoxes in creation paradoxes — both at the small level and the entire level of the work — making an interesting connection between mathematics, philosophy, and literature. He introduced paradoxist distiches, tautologic distiches, and dualistic distiches, which were inspired by the mathematical logic. The literary experiments were realized by him in the dramas: "Country of the Animals", "An Upside-Down World", "MetaHistory", "Formation of the New Man", and the others. Florentin Smarandache did many poetical experiments in the framework of his avant-garde. He published paradoxist manifestos: "Le Sens du Non-Sens" (1983), "Antichambres, Antipoésies, Bizarreries" (1984, 1989), "NonPoems" (1990), where he changed the French and respectively English linguistics clichés. While "Paradoxist Distiches" (1998) introduces new species of poetry with fixed form. Eventually he edited three International Anthologies on Paradoxism (2000-2004) with texts from about 350 writers from around the world in many languages. Twelve books were published that analyze his literary creation, including "Paradoxism's Aesthetics" by Titu Popescu (1995), and "Paradoxism and Postmodernism" by Ion Soare (2000).

Florentin Smarandache is also known as an artist working in the style of modernism. His experimental art albums comprises over-paintings, non-paintings, anti-drawings, superphotos, foreseen with a manifesto: "Ultra-Modernism?" and "Anti-manifesto".

In mathematics Prof. Smarandache introduced the degree of negation of an axiom or of a theorem in geometry: Smarandache geometries (1969), which can be partially Euclidean and partially non-Euclidean. He also introduced multi-structures (Smarandache n-structures, where a weak structure contains an island of a stronger structure), and multi-spaces (a combination of heterogeneous spaces). He introduced and developed many sequences and functions in number theory. Florentin Smarandache also generalized fuzzy logics to "nueutrosophic logic" and, similarly, he generalized fuzzy set to "neutrosophic set". Also, he suggested an extension of the classical probability and imprecise probability to "neutrosophic probability". Together with Dr. Jean Dezert (ONERA, France), he generalized Dempster-Shafer theory to a new theory of plausible and paradoxist fusion, which is now known as Dezert-Smarandache theory (2002). In 2004 he designed an algorithm for the unification of fusion theories (UFT) used in bioinformatics, robotics, and military.

In physics, Prof. Smarandache introduced a series of paradoxes (quantum Smarandache paradoxes). On the basis of neutrosophic logics, he also considered a theoretical possibility of a third form of matter, called as unmatter, which is a combination of matter and antimatter (2010). Based on his early 1972 publication (when he was a student in Romania), Prof. Smarandache suggested the hypothesis that "there is no speed barrier in the universe and one can construct any speed". This hypothesis was partially validated on September 22, 2011, when researchers at CERN experimentally proved that the muon neutrino particles travel with a speed greater than the speed of light. Upon his hypothesis he suggested a modification of Einstein's theory of relativity, where the relativistic paradoxes are only the observable effects registered by a particular observer, not the true reality. The speed of light in vacuum is thus considered to be a variable value, which is dependent on the type of synchronization of the particular observer. It is a constant for only the observer who uses light beams as the medium of synchronization. Therefore, the cosmological redshift and the other relativistic effects are true only for the social community of the observers whose picture of the world is "painted" on the basis of information obtained from the light signals.

In philosophy, Florentin Smarandache introduced neutrosophy (1995), which is a new generalization of Hegel's dialectic. Neutrosophy has a basis in his researches in mathematics and economics, such as "neutrosophic logic", "neutrosophic set", "neutrosophic probability", and "neutrosophic statistics". Neutrosophy is a new branch of philosophy that studies the origin, nature, and scope of neutralities, as well as their interactions with different ideational spectra. This theory considers every notion or an idea <A> together with its opposite or negation <Anti-A> and the spectrum of "neutralities" <Neut-A>. The <Neut-A> and <Anti-A> ideas together are referred to as <Non-A>. According to this theory every idea <A> tends to be neutralized and balanced by <Anti-A> and <Non-A> ideas as the state of equilibrium.

International Conference on Neutrosophy and Neutrosophic Logics was held in December 2001 at the University of New Mexico, USA. International Conference on Smarandache Type Notions in Number Theory was held in August 1997 at University of Craiova, Romania. International Conference on Smarandache Geometries was held in May 2003 at Griffith University in Queensland, Australia.International Conference on Smarandache Algebraic Structures was held in December 2004 at Loyola College in Madras, India.

Prof. Smarandache authored numeous monographs, and about 200 research papers published in about 50 scientific journals. He also was the editor of more than a hundred of scientific books authored by the other scientists. In addition to his scientific research, Prof. Smarandache gives lectures throughout the world for over many years. He was an invited lecturer at Bloomsburg University (USA, 1995), University of Berkeley (USA, 2003), NASA Langley Research Center (USA, 2004), Jadavpur University (India, 2004), NATO Ad-

vanced Studies Institute (Bulgaria, 2005), Institute of Biophysics (Russia, 2005), University Sekolah Tinggi Informatika and University Kristen Satya Wacana Salatiga (Indonesia, 2006), Minufiya University (Egypt, 2007), Universitatea din Craiova (Romania, (2009), Air Force Research Lab and Griffiss Institute (USA, 2009), Air Force Institute of Technology at Wright-Patterson AFB (USA, 2009), Air Force Research Lab of State University of NY Institute of Technology in Rome (NY, USA, 2009), COGIS (France, 2009), ENSIETA — National Superior School of Engineers and Study of Armament in Brest (France, 2010), Institute of Solid Mechanics and Commission of Acoustics (Romania, 2011), Guangdong University of Technology in Guangzhou (China, 2012), Okayama University (Japan, 2013), etc.

In 2011, Academia DacoRomana in Bucharest bestowed upon Prof. Smarandache the Doctor Honoris Causa degree. In the same year, Beijing Jiaotong University in China bestowed the Doctor Honoris Causa degree upon him as well.

We all, who know Prof Florentin Smarandache closely over decades, point out his benignity, enthusiasm, and scientific creativity. He never rests in mind, but always works on different fields of science, literature, and art. We wish him to be always full of energy, pink health, and to have happy life for many years.

Submitted on December 10, 2013 / Accepted on December 10, 2013

On Some General Regularities of Formation of the Planetary Systems

Anatoly V. Belyakov

E-mail: belyakov.lih@gmail.com

J. Wheeler's geometrodynamic concept has been used, in which space continuum is considered as a topologically non-unitary coherent surface admitting the existence of transitions of the input-output kind between distant regions of the space in an additional dimension. This model assumes the existence of closed structures (micro- and macrocontours) formed due to the balance between main interactions: gravitational, electric, magnetic, and inertial forces. It is such macrocontours that have been demonstrated to form — independently of their material basis — the essential structure of objects at various levels of organization of matter. On the basis of this concept in this paper basic regularities acting during formation planetary systems have been obtained. The existence of two sharply different types of planetary systems has been determined. The dependencies linking the masses of the planets, the diameters of the planets, the orbital radii of the planet, and the mass of the central body have been deduced. The possibility of formation of Earth-like planets near brown dwarfs has been grounded. The minimum mass of the planet, which may arise in the planetary system, has been defined.

1 Introduction

Wheeler's geometrodynamic concept, in which microparticles are considered as vortical oscillating deformations on a non-unitary coherent surface and the idea about transitions between distant regions of space in the form of Wheeler's "wormholes", made it possible to substantiate the existence of closed structures (micro- and macrocontours) acting at various levels of organization of matter [1–3].

These contours are material, based on the balance between main interactions: electrical, magnetic, gravitational, and inertial forces. They are not associated to the specific properties of the medium; they determine the important properties of objects and allow using analogies between objects of various scales.

Such approach allows using a model that best are independent of the properties of an object or medium. In this paper the concept is used to establish some of the basic laws of the formation of planetary systems. Here, as in paper [2], there is no need to consider the nature of the cosmological medium, i.e. protoplanetary nebula, from which the planets formed, and other specific features of the process. Idea of the planetary system consisting of some amount of macrocontours, from which planets formed, and the contours of a higher order integrating the planets and a central body was enough to get the general regularities.

2 Initial assumptions

As was shown earlier [1], from the purely mechanistic point of view the so-called *charge* only manifests the degree of the nonequilibrium state of physical vacuum; it is proportional to the momentum of physical vacuum in its motion along the contour of the vortical current tube. Respectively, the *spin* is proportional to the angular momentum of the physical vacuum with respect to the longitudinal axis of the contour, while the *magnetic interaction* of the conductors is analogous to the forces acting among the current tubes. It is given that the elementary unit of such tubes is a unit with the radius and mass equal to those of a classical electron (r_e and m_e).

It should be noted that in [1, 2] the expressions for the electrical and magnetic forces are written in a "Coulombless" form with charge replaced by electron limiting momentum.

In this case, the electrical and magnetic constants (ε_0 and μ_0) are expressed as follows:

$$\varepsilon_0 = m_e/r_e = 3.33 \times 10^{-16} \text{ kg/m}, \quad (1)$$

$$\mu_0 = 1/\varepsilon_0 c^2 = 0.0344 \text{ N}^{-1}, \quad (2)$$

where c is the velocity of light.

Thus, the electric constant ε_0 makes sense the linear density of the vortex tube current, and the magnetic constant μ_0 makes sense the reciprocal value of the interaction force between two elementary charges.

In [2] the relative comparison of various interactions have been carried out and the basic relationships were obtained, some of which are necessary for the understanding of this article.

1. *The balance of electric and magnetic forces* gives a geometric mean — a characteristic linear parameter that is independent of the direction of the vortex tubes and the number of charges:

$$R_s = (r_0 L)^{1/2} = (2\pi)^{1/2}\, c \times [sec] = 7.52 \times 10^8 \text{ m} \quad (3)$$

– a magnitude close to the Sun radius and the sizes of typical stars, where r_0, and L are the rotary radius or the distance between the vortex tubes (thread) and their length.

2. *The balance of gravitational and inertial (centrifugal) forces* gives the maximum gravitational mass of the object satisfying the condition (3):

$$M_m = \frac{R_s c^2}{\gamma} = f R_s \varepsilon_0 = 1.01 \times 10^{36} \text{ kg}. \quad (4)$$

3. *The balance of magnetic and gravitational forces* also results in a geometrical mean:

$$(r_0 L)^{1/2} = \left(\frac{\varepsilon}{f}\right)^{1/2} R_s, \quad (5)$$

where the ratio of the products $\varepsilon = (z_{g1} z_{g2})/(z_{e1} z_{e2})$ is an *evolutionary parameter*, which characterizes the state of the medium and its changes, as the mass carriers become predominant over the electrical ones and, as a matter of fact, shows how the material medium differs from vacuum. Here z_e and z_g are the relative values of charge and mass in the parameters of electron charge and mass, f — is the ratio of electrical-to-gravitational forces, which under the given conditions is expressed as follows:

$$f = \frac{c^2}{\varepsilon_0 \gamma} = 4.16 \times 10^{42}, \quad (6)$$

where γ is the gravitational constant. In the general case, expression (5) gives a family of lengthy contours consisting of contra-directional closed vortex tubes (*mg-contours*).

4. The vortex tubes can consist, in their turn, of a number of parallel unidirectional vortex threads, whose stability is ensured by the *balance of magnetic and inertial forces* forming *mi-zones*.
5. Structurizations of the primary medium, where there is more than one pair of balanced forces, results in complication an originally unstructured mass by forming in it local *mi*-zones. In particular, the number of *mi*-zones in the object of arbitrary mass M_i will be:

$$z_i = \left(\frac{M_m}{M_i}\right)^{1/4}. \quad (7)$$

3 Planetary systems

Let us assume there is a cloud of the originally protoplanetary material having an evolutionary parameter ε, in which a planetary system with a central mass M_0 and planets with a mass m_p on a radius r_p, with a rotary velocity v_0 is being formed. Let us assume that the central body is a point-like mass, and the mass of the planet is formed of contours of total number z_p and axis sizes $d_p \times l_p$. Then the mass of the planet can be expressed as the total mass of contours:

$$m_p = z_p \varepsilon \varepsilon_0 l_p. \quad (8)$$

The characteristic size of the *mg*-contour by analogy to (5):

$$\left(l_p d_p\right)^{1/2} = \left(\frac{\varepsilon}{f}\right)^{1/2} R_s. \quad (9)$$

Suppose the number of *mg-contours* constituting the mass of the planet is proportional to the distance to the central body, i.e. a planet contour is a *structural unit for the contour of higher order* that integrates planet with the central body:

$$z_p = \frac{r_p}{d_p}. \quad (10)$$

This is true for a flat homogeneous disk of the initial nebula, where the *mg*-contour is *one-dimensional*, but in general, density of medium may be different and, of course, decrease toward the periphery. The protoplanetary disk may have a local rarefaction or condensation, i.e. have sleeves or be *flat-spiral*. Therefore, in general, we have:

$$z_p = \left(\frac{r_p}{d_p}\right)^n, \quad (11)$$

where the coefficient n reflects the "packaging" of contours in the model object (planet).

The orbital velocity of the planet can be expressed from the balance of centrifugal and gravitational forces:

$$v_0 = \left(\frac{\gamma M_0}{r_p}\right)^{1/2}. \quad (12)$$

On the other hand, we can use the analogy of the Bohr atom, where in the proton-electron system the orbital velocity of the electron at the radius of r_i is equal to

$$v_0 = c\left(\frac{r_e}{r_i}\right)^{1/2}. \quad (13)$$

Then for the contour integrating the planet with the central body, taking the parameter l_p as the unit of length, an analogous relation can be written:

$$v_0 = c\left(\frac{l_p}{r_p}\right)^{1/2}. \quad (14)$$

The number of *mg*-contour z_0 for the stable state of the object, as given in [2], should be taken equal to the number of *mi*-zones:

$$z_p = z_i = \left(\frac{M_m}{m_p}\right)^{1/4}. \quad (15)$$

Share further the dimensionless parameter: $M = M_0/M_m$, $m = m_p/M_m$, $v = v_0/c$, $r = r_p/R_s$, $l = l_p/R_s$, $d = d_p/R_s$, and $z = m^{-1/4}$. Taking into account (8-15), after transformations we obtain expressions describing the dependence of the planet mass on its orbit radius and mass of the central body:

$$m = \left(rM^2\right)^{4n/(5n-1)}, \quad (16)$$

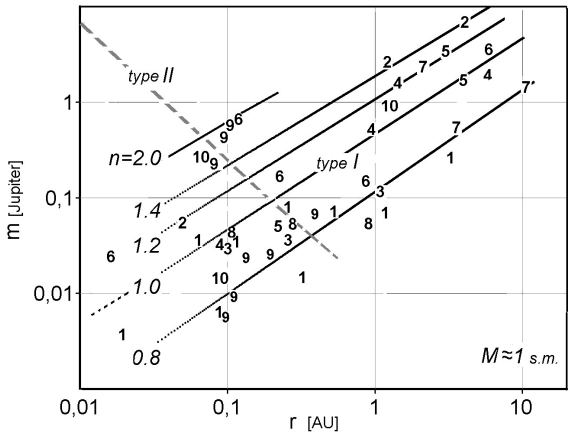

Fig. 1: Dependence of the mass of Type I planets on their orbital radius at $M \approx 1$ s.m. 1 — HD10180, 2 — HD125612, 3 — HD134606, 4 — HD160691, 5 — HD204313, 6 — HD75732, 7 — HD95128, 8 — HD31527, 9, 10 — KOI.

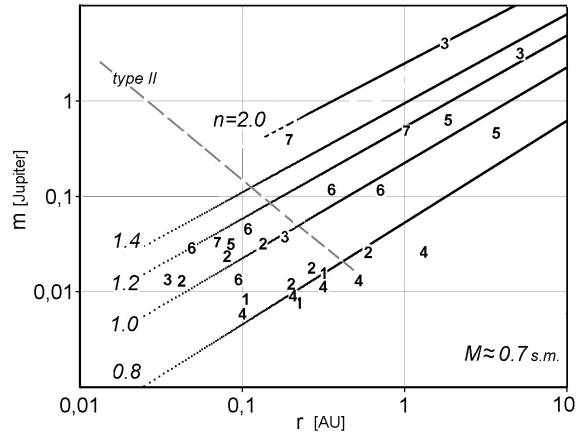

Fig. 2: Dependence of the mass of Type I planets on their orbital radius at $M \approx 0.7$ s.m. 1 — HD20794, 2 — HD40307, 3 — GJ676A, 4 — HD10700, 5 — HD181433, 6 — KOI 701, 7 — HIP57274.

proportions of *mg*-contour

$$d = \frac{m^{5/4}}{M^2}, \tag{17}$$

$$l = M, \tag{18}$$

and the value of the evolutionary parameter

$$\varepsilon = \frac{fm^{5/4}}{M}. \tag{19}$$

However, this model also admits a second case of orientation of *mg*-contour according to another to its axis. In this case an expression for z_p analogous to (11) can be written:

$$z_p = \left(\frac{r_p}{l_p}\right)^k; \tag{20}$$

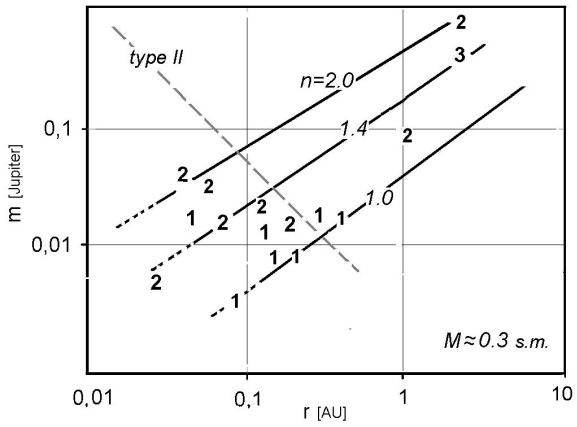

Fig. 3: Dependence of the mass of Type I planets on their orbital radius at $M \approx 0.3 \ldots 0.4$ s.m. 1 — GJ, 2 — Gliese, 3 — OGLE.

then relation $m(r)$ taking into account (15), (18), (20) will look as follows:

$$m = \left(\frac{M}{r}\right)^{4k}. \tag{21}$$

In this variant the emerging masses of planets quickly decrease to the periphery of the protoplanetary disk, and it can be assumed that such initial nebulae are *lenticular in nature*. We call planets corresponding relations of (16) and (20) as *Type I planets and Type II planets*, accordingly.

The actual data relating to the planets in extrasolar planetary systems having three or more planets plotted on diagrams in the coordinates of r — m, where r — the size of the major semiaxis, (Fig. 1-3).

The results of the site *http://www.allplanets.ru/index.htm* have been used. The numbers in the figures correspond to the position of the experimental points and point to the sections of the catalog of extrasolar planets.

The calculated dependencies $m(r)$ according with formula (16) converted to coordinates expressed in the masses of Jupiter and astronomical units by multiplying m by $M_m/1.87 \times 10^{27}$ and r by $R_s/1.5 \times 10^{11}$. These dependencies correspond to the period of planet formation, but several isolines n are shown, because the conditions of formation of the planets and their further evolution is unknown. A large scatter in the values is present on this and others diagrams; in this case it is inevitable. However, the dependence of the masses of extrasolar planets on their orbital radii and on the masses of central stars is revealed quite clearly in agreement with the expression (16). These regularities, i.e. increase in the mass of planets with increasing distance to the central star and with increasing the mass of central stars, also confirmed in [4–7] and others.

Types II planets do not fit into this pattern. In (Fig. 1-3) they would be located near the dashed line. They have masses of the order of the mass of Jupiter and greater than one and are in orbits close to the central star (hot Jupiters).

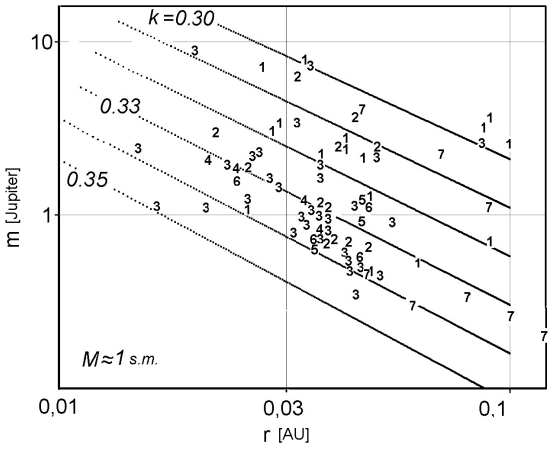

Fig. 4: Dependence of the mass of Type II planets on their orbital radius at $M \approx 1$ s.m. 1 — CoRoT, 2 — HAT-P, 3 — WASP, 4 — TrES, 5 — XO, 6 — OGLE, 7 — HD.

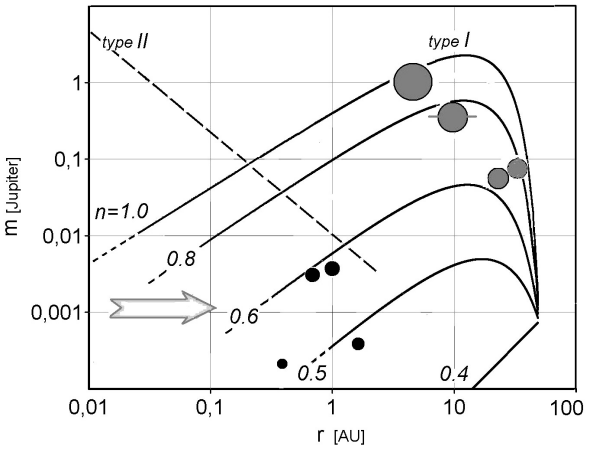

Fig. 6: Dependence of the mass of the solar system planets on their orbital radius.

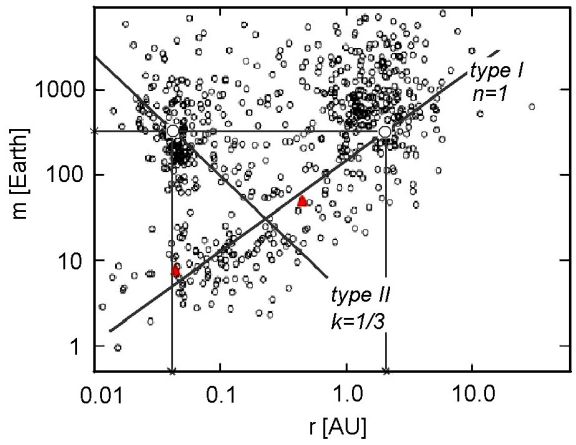

Fig. 5: The calculated dependence $m(r)$ on the background of distribution of all known extrasolar planets in the semimajor axis-mass parameter spaces. Triangles represent the planets of the system GJ 221. Masses are expressed in the masses of the Earth.

Figure 4 shows the actual data on extrasolar Type II planets, which are in agreement with the expression (21) at a coefficient k, whose value differs very little from 1/3. When comparing (11) and (20), given that $k \approx 1/3$, one comes to the conclusion that in this case *mg*-contour is *a three-dimensional* element. With decreasing the density of medium towards the periphery of the disc the dimension of *mg*-contour can be reduced.

These planets are mainly found in single-planet systems. The existence of systems of this type was unexpected for astrophysicists. It is supposed that their formation or dynamical history occurred in another way when the planets were formed on the periphery of the initial disc and then migrated to closer orbits [8]. In the framework of the proposed model the existence of such planetary systems *is natural*. Moreover, this situation by Type II occurs in systems of planetary satellites, such as the Earth-Moon, Neptune-Triton, and Pluto-Charon.

Figure 5, taken from the article [9], shows a large array of data on extrasolar planets in the coordinates r — m (star masses are different). In order to confirm these regularities isolines $m(r)$ by (16) and (21) at $M = 1$ s.m. superimposed on the diagram; they just pass through areas, where the planets are at the most grouped. Moreover, the model allows us to explain the presence of the large number of massive planets and indicate the area, where they are concentrated.

In paper [2] it is shown that for the central star there is a period of evolution when the number of *mg*-contours is equal to the number of *mi*-zones, which should correspond to the most *stable or balanced state*. It is this period is most favorable for the formation of the most massive planets. In this case, the evolutionary parameter ε receives the expression:

$$\varepsilon = fM^{11/12}. \tag{22}$$

Then, as it follows from (19) and (22),

$$m = M^{23/15}. \tag{23}$$

For the mass of the Sun $M = 2 \times 10^{-6}$. Then $m_p = (2 \times 10^{-6})^{23/15} M_m$ or 1.85×10^{27} kg, which is almost exactly the mass of Jupiter. Depending on the type of planetary system this mass can arise in orbit size of 0.038 au (hot Jupiters), or 2.3 au (cold Jupiter), (Fig. 5). More massive stars give rise greater mass of the planet.

Figure 6 shows the dependencies of $m(r)$ by (16) at different n and by (21) at $k = 1/3$ as well as the position of the planets in the solar system. Decrease in the value of index n with increasing radius and decreasing density of protoplanetary disk is interpreted by expression $n - (n - 0.4)r/50$, assuming that the disk was limited of radius 50 au wherein n was reduced to a value 0.4 at the periphery.

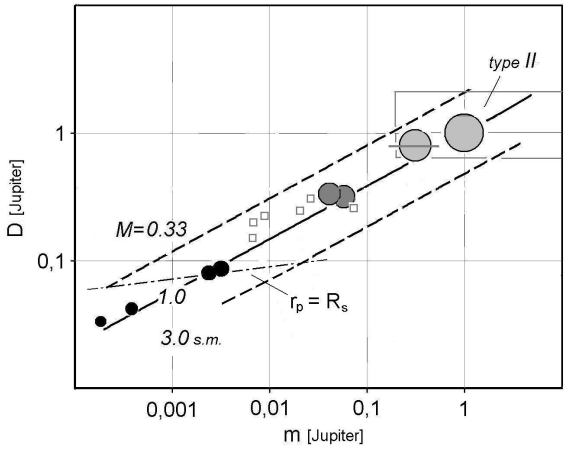

Fig. 7: Dependence of the diameter of the planets on their mass for Type I planets. The squares marked planets of the system Kepler-11. Rectangle roughly bounded region of massive Type II planets at $M \approx 1$. Dash-dot line shows the boundary of the minimum planetary masses, determined from the condition $r_p = R_s$ at $n = 1$.

In general, the initial protoplanetary cloud of the solar system would fit the flat model at $n \approx 1$ if it is assumed that the small planets were formed close to the Sun, but later moved to a more distant orbit under the influence of massive planets that were formed later. Detection of Earth-like planets that are very close to the central star [10, 16] confirms this assumption. It is also possible that the initial cloud had a low density on the orbits where small planets have been formed.

4 On the parameters of planets

For Type I planets calculations show that $d \gg l$, i.e. a *mg*-contour is actually a one-dimensional structure and when "packaging" it in a volume ratio of its linear dimensions, i.e. ratio of the diameters of planets averaged over density, taking into account (17), must meet the relationship:

$$D = d^{1/3} = m^{5/12} M^{-2/3}. \tag{24}$$

These parameters are here dimensionless and can be expressed as, for example, the parameters of Jupiter and the Sun.

Figure 7 shows the dimensionless dependence $D(m)$ by (24) for Type I planets reduced to the parameters of Jupiter and mass of the Sun. The planets of the solar system are located along a solid line. It also shows the position of the six planets of the sistem Kepler-11 having an intermediate density [11], which generally corresponds to the calculated dependence.

It is interesting to note that the expression (24) obtained solely on the basis of general provisions and being adequate to a wide range for Type I planets, in fact, coincides with the analogous dimensionless dependence derived by the authors in the paper [7]. However, this dependence was obtained by the authors by solving the equation of state, which describes the relationship between density, pressure, and temperature for the substance under conditions of thermodynamic equilibrium. The position of the terrestrial planets corresponds exactly to the general trend and confirms the assumption that these planets were formed by Type I near the Sun.

During evolution first planets were formed when ***the orbital angular momentum of the planet is compared to the rotational angular momentum of the central body***. Let us compare the corresponding expression: to the central body derived in [2] and, referring to (10), (12), (17), (19), at $n = 1$, analogous one to the planet:

$$M \frac{\varepsilon}{f} M_m c R_s = M^{7/10} \left(\frac{\varepsilon}{f} \right)^{6/5} M_m c R_s. \tag{25}$$

As follows from (25):

$$\varepsilon = f M^{3/2}, \tag{26}$$

and then one can obtain:

$$m = M^2, \tag{27}$$

$$r = 1, \tag{28}$$

Radius $r_p = R_s$ is the natural limit for *the minimum masses of Type I planets*. The outer planets, whose mass is *greater*, have the orbital angular momentum greater than the rotational angular momentum of the central star. With $M = 1$ s.m. $m_{p\,min} = 4 \times 10^{-12}$ $M_m = 4 \times 10^{24}$ kg, which just corresponds to the average mass of the terrestrial planets. Thus, in this model the existence of Earth-like planets near the central star is natural.

The size of the planets of type II can be estimated by the value of the orbital radius, having on a *mg*-contour, r/z. Keeping in mind the formula (20) at $k = 1/3$, and expressing r from (21), we obtain:

$$D \sim \frac{M}{m^{1/2}}, \tag{29}$$

There is a need additionally to take account the fact that the unit *mg*-contour is in this case not one-dimensional, and the mass of the model object is proportional to the parameter ε, formula (8). Thus, the relation (29) should be supplemented. Using (19) and moving from the mass ratio to the ratio of linear sizes the final expression gets the following forms:

– in the case of a three-dimensional *mg*-contour

$$D = \frac{M}{m^{1/2}} \left(m^{5/4} M^{-1} \right)^{1/3} = \frac{M^{2/3}}{m^{1/12}}; \tag{30}$$

– for the less dense medium, in the case of two-dimensional *mg*-contour, formula (30) takes the form:

$$D = \frac{M}{m^{1/2}} \left(m^{5/4} M^{-1} \right)^{1/2} = \frac{M^{1/2}}{m^{1/8}}; \tag{30a}$$

The obtained dimensionless relationships are generally in agreement with the actual laws. Figure 8 shows the dependence of $D(M)$, and Figure 9 shows the dependence of $D(m)$ calculated from formulas (30) and (30a) at different M, which are for illustrative purposes superimposed on the chart taken from the article [12].

In particular, it becomes clear both the existence of planets with similar sizes but sharply differing masses and having the same mass at various sizes. Planets with a relatively small mass, for example, GJ 1214b [13], Kepler-87c (they are shown in Figure 8 and 9), and others, formed probably by type II; their diameters varied greatly and correspond to the values, which are calculated by the option (30a).

The densities of Type I and Type II planets through their mass and the mass of a star in dimensionless units (in units of the Jupiter's mass and the Sun's mass), having in mind that $\rho \sim mD^{-3}$, have radically different character and can be expressed as follows:

$$\rho_1 = m^{-1/4} M^2, \tag{31}$$

$$\rho_2 = m^{5/4} M^{-2}, \tag{32}$$

$$\rho_{2a} = m^{5/8} M^{-3/2}. \tag{32a}$$

Of course, obtained dependences are not precise or definitive. They only reflect the general trends uniting the diameter of the planet to its mass and the mass of stars in the period of the formation of planetary systems. By equating the orbital angular momentum of the planet and the rotational angular momentum of the central body one can obtain the relations similar to (25-28) for Type II planets at $k = 1/3$:

$$M\left(\frac{\varepsilon}{f}\right) M_m c R_s = M^{3/2}\left(\frac{\varepsilon}{f}\right)^{1/2} M_m c R_s, \tag{33}$$

$$\varepsilon = fM, \tag{34}$$

$$m = M^{8/5}, \tag{35}$$

$$r = M^{-1/5}, \tag{36}$$

which determine their specific mass and orbital radius. At $M = 1$ s.m. $m_p = 7.6 \times 10^{-10} M_m = 7.6 \times 10^{26}$ kg or 0.4 Jupiter's masses, $r_p = 13.8\ R_s = 1.03 \times 10^{10}$ m or 0.07 au. The inner planets with a greater mass have angular momentum that *is less* than that of the central star.

As follows from (21) and (32) Type II planet masses decrease with increasing distance from the central star as well as their density decreases. This is illustrated by the planet Kepler 87c having a very low density with its orbital radius of 136 R_s or 0.68 au. Formation of the planets in more remote orbits it is unlikely, where the less often they exist, the more massive major planet [8].

Low-mass rocky planets of type II can not be formed near Sun's mass stars and having greater masses, but, as follows from (32), their formation is possible in the system of

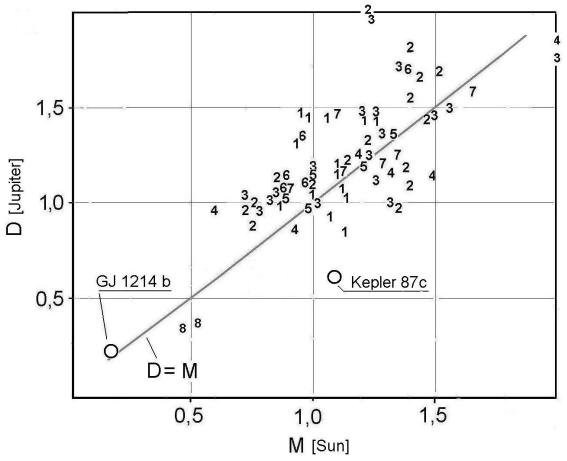

Fig. 8: Dependence of the diameter of the planets on the mass of the central star (masses of the planets are different). 1 — CoRoT, 2 — HAT-P, 3 — WASP, 4 — KOI, 5 — XO, 6 — TrES, 7 — OGLE, 8 — GJ.

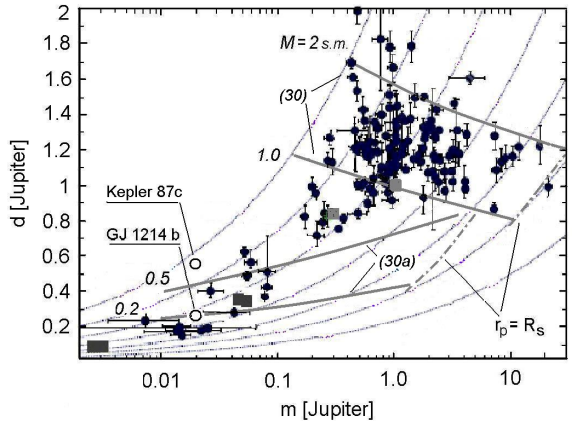

Fig. 9: The calculated dependences $D(m)$ of Type II planet on the background of distribution of known transit extrasolar planets in the planet mass-radius spaces. Squares shows the planets in the solar system. Dotted lines are lines of equal density — 0.1, 0.3, 0.9, 3.0, 9.0, 25.0, and 100 g/cm^3. Dash-dotted line limits the maximum masses of the planets, $k = 1/3$.

dwarf stars when $M < 1$ s.m. Indeed, another test of the correctness of the presented model may serve determination the masses of stars, at which planets with masses and sizes like the Earth can be formed. Let their mass is in the range from 0.001 . . . 0.01 Jupiter's mass and the density is 3 . . . 5 Jupiter's density.

Then for the Type I planets formula (31) gives: $M = 0.73 \ldots 1.26$ s.m. and for Type II planets formulas (32) and (32a) give: $M = 0.006 \ldots 0.032$ and $M = 0.019 \ldots 0.07$ s.m. The first solution is obvious and corresponds to the stars

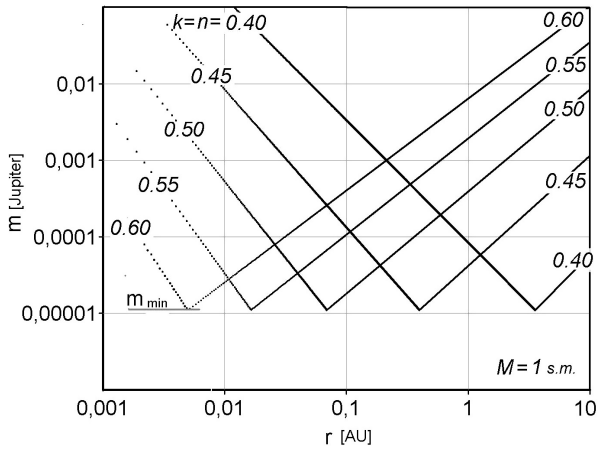

Fig. 10: Dependence of the mass of the planets on their orbital radius at $l = d$.

with a mass close to the mass of the Sun and the second solutions just correspond to the very low-mass stars — *brown dwarfs*.

This prediction proved to be correct. Indeed, recent observations have shown that is quite possible the formation of Earth-like planets around of brown dwarfs and there may be created suitable conditions for emergence of life [14]. These types of planetary systems even more preferable since no need planets to migrate to more distant (as in the case of the Earth) and the suitable masses of the brown dwarfs vary within a more wide range. The question arises whether there are conditions under which the formation of planets in the evolution of both types is equally probable?

It is logical to assume that in the initial period there had been rarefied initial spherical cloud around the central body, which is then transformed into or flatspiral disk, or lenticular in shape, from which Type I planets or Type II planets, respectively, have been formed. Hypothetically, this would correspond to the initial state of complete equality of conditions of planets formation in both types, i.e. $l = d = M$, $n = k$, masses of planets by (16) and (21) are equal.

Having in mind (16), (17), (21), we find:

$$n = k = 0.2\left(\frac{\lg\left(rM^2\right)}{\lg\left(M/r\right)} + 1\right), \tag{37}$$

$$m = M^{12/5}. \tag{38}$$

Thus, this mass depending on the coefficient n may occur at any orbit (Fig. 10). The size of the planet in this case is uncertain since dependences (24) and (30) are here incorrect. One can specify the maximum size of an object if mg-counters are packaged in a linear structure, $D_{max} = zl$. Since $z = m^{-1/4}$ and $l = M$, using (38), we obtain:

$$D_{max} = M^{2/5}. \tag{39}$$

Convergence coefficient values of n and k indicate a decrease formally in the density of medium in any variant evolution that, obviously, corresponds to the moust low mass. The average value of the coefficient equal to 0.5 at $M = 1$ s.m. corresponds to the orbital radius of 0.07 au, which coincides with the specific radius for Type II planets.

For the mass of the Sun, $m_{p\,lim} = 2.1 \times 10^{-14} M_m = 2.1 \times 10^{22}$ kg, $D_{p\,max} = 0.0053\, R_s = 3.9 \times 10^6$ m. It is unknown whether such planets form in reality. In any case, in the solar system there are no regular planet's masses less than $m_{p\,lim}$, except Pluto having a similar mass of 1.3×10^{22} kg, the status of which is uncertain. The same can be said of the satellite systems of the major planets. Masses less settlement not observed to date also among extrasolar planets.

The existence of lowest masses for the planets formed and, accordingly, their lowest diameters explains fact of rapid decrease of the planets having a small radius as well as existence of a maximum of the planetary radii specified in [15].

5 Conclusion

Planetary systems can be quite diverse as their structure depends on the initial composition of the protoplanetary cloud, mass and type of stars, formation history of the planetary system, and the random factors. Nevertheless, there are some general patterns.

There are two types of planetary systems. In the system of the first type planets are formed from flatspiral protoplanetary cloud. Masses of Type I planets increase to the periphery passing through their maximum (cold Jupiters) that occur in the distance from the center in the local condensations of the medium (the sleeves, spirals), supposedly, in later periods of the evolution. Earth-like planets are formed near the central star and maybe can migrate to the more remote orbits.

In the second type of planetary systems planets are formed from a protoplanetary cloud lenticular or elliptical type. The masses and densities of Type II planets decrease to the periphery of the disc. Massive planets (hot Jupiters) are formed in condensations near the central star; the formation of other planets in more distant orbits is unlikely. Low-mass rocky planets in these systems can be formed only at low-mass stars (brown dwarfs).

The possibility of the formation of Earth-like planets in the planetary systems of brown dwarfs has been predicted.

The regularities among the masses, sizes, orbital radii of the planets and masses of the central stars have been obtained.

Submitted on: July 03, 2013 / Accepted on: July 21, 2013

References

1. Belyakov A. V. Charge of the electron, and the constants of radiation according to J.A.Wheeler's geometrodynamic model. *Progress in Physics*, 2010, v. 4, 90–94.
2. Belyakov A. V. Evolution of Stellar Objects According to J. Wheeler's Geometrodynamic Concept. *Progress in Physics*, 2013, v. 1, 25–40.

3. Belyakov A. V. On the independent determination of the ultimate density of physical vacuum. *Progress in Physics*, 2011, v. 2, 27–29.
4. Stephane Udry. *Geneva University*, Debra Fischer. *San Francisco State University*, Didier Queloz. *Geneva University*. A Decade of Radial-Velocity Discoveries in the Exoplanet Domain.
5. Montet B. T., Crepp J. R. et al. The trends high-contrast imaging survey. iv. the occurrence rate of giant planets around m-dwarfs. 24 July 2013, arXiv: astro-ph/1307.5849 v1.
6. Jones M. I., Jenkins J. S. et al. Study of the impact of the post-MS evolution of the host star on the orbits of close-in planets. A giant planet in a close-in orbit around the RGB star HIP63242. June 2013, arXiv: astro-ph/1306.3939 v1.
7. Seager S., Kuchner M., Hier-Majumder C., Militzer B. Mass-Radius Relationships for Solid Exoplanets. 19 Jul 2007, arXiv: 0707.2895.
8. Steffen J. H., Ragozzine D. et al. Kepler constraints on planets near hot Jupiters. 10 May 2012, arXiv: astro-ph.EP/1205.2309 v1.
9. Arriagada P., Anglada-Escud G. et al. Two planetary companions around the K7 dwarf GJ 221: a hot super-Earth and a candidate in the sub-Saturn desert range. 9 May 2013, arXiv: astro-ph/1305.2203 v1.
10. Sanchis-Ojeda R., Rappaport S. et al. Transits and occultations of an earth-sized planet in an 8.5-hour orbit. 17 May 2013, arXiv: astro-ph/1305.4180 v1.
11. Lissauer J. J., Jontof-Hutter D. et al. All Six Planets Known to Orbit Kepler-11 Have Low Densities. 14 Jun 2013, arXiv: astro-ph/1303.0227 v2.
12. Sato B., Hartman J. D. et al. HAT-P-38b: A Saturn-Mass Planet Transiting a Late G Star. 24 Jan 2012, arXiv: astro-ph/1201.5075 v1.
13. Charbonneau D., Berta Z. K. et al. A super-Earth transiting a nearby low-mass star. http://fr.arxiv.org/ftp/arxiv/papers/0912/0912.3229.pdf. Nature 2009.
14. Ricci L., Testi L., Natta A., Scholz A., Gregorio-Monsalvo L. Alma observations of ρ-oph 102: grain growth and molecular gas in the disk around a young brown dwarf. 28 Nov 2012, arXiv: astro-ph.SR/1211.6743 v1.
15. Morton T. D., Swift J. The radius distribution of small planets around cool stars. 14 Mar 2013, arXiv: astro-ph/1303.3013 v1.
16. Charpinet S., Fontaine G. et al. A compact system of small planets around a former red-giant star. 22 Dec 2011, Nature, 480, 496–499.

LETTERS TO PROGRESS IN PHYSICS

The Liquid Metallic Hydrogen Model of the Sun and the Solar Atmosphere VIII. 'Futile' Processes in the Chromosphere

Joseph Luc Robitaille[1] and Pierre-Marie Robitaille[2]

[1]P.O. Box 21025, Columbus, Ohio, 43221.
[2]Department of Radiology, The Ohio State University, 395 W. 12th Ave, Columbus, Ohio 43210, USA.
robitaille.1@osu.edu

In the liquid metallic hydrogen solar model (LMHSM), the chromosphere is the site of hydrogen condensation (P.M. Robitaille. The Liquid Metallic Hydrogen Model of the Sun and the Solar Atmosphere IV. On the Nature of the Chromosphere. *Progr. Phys.*, 2013, v. 3, L15–L21). Line emission is associated with the dissipation of energy from condensed hydrogen structures, CHS. Previously considered reactions resulted in hydrogen atom or cluster addition to the site of condensation. In this work, an additional mechanism is presented, wherein atomic or molecular species interact with CHS, but do not deposit hydrogen. These reactions channel heat away from CHS, enabling them to cool even more rapidly. As a result, this new class of processes could complement true hydrogen condensation reactions by providing an auxiliary mechanism for the removal of heat. Such 'futile' reactions lead to the formation of activated atoms, ions, or molecules and might contribute to line emission from such species. Evidence that complimentary 'futile' reactions might be important in the chromosphere can be extracted from lineshape analysis.

In order to explain the occurrence of the dark lines in the solar spectrum, we must assume that the solar atmosphere incloses a luminous nucleus, producing a continuous spectrum, the brightness of which exceeds a certain limit. The most probable supposition which can be made respecting the Sun's constitution is, that it consists of a solid or liquid nucleus, heated to a temperature of the brightest whiteness, surrounded by an atmosphere of somewhat lower temperature.

Gustav Robert Kirchhoff, 1862 [1]

1 Introduction

During a solar eclipse, the flash spectrum associated with the chromosphere of the Sun becomes readily visible [2–5]. This spectrum is dominated by emission lines from hydrogen, most notably H-α, which gives rise to its characteristic color. However, the flash spectrum also contains a wide array of emission lines generated from neutral atoms, ions, or molecules [2–5]. Within the context of the Standard Solar Models (SSM) [6], these emission lines are produced by random temperature related excitation processes in this region of the Sun. Because the SSM adopt a gaseous solar body, the chromosphere is devoid of function and line emission does not help to account for structure.

In sharp contrast, within the Liquid Metallic Hydrogen Solar Model (LMHSM) [7, 8], the chromosphere is a site of hydrogen and proton capture, while the corona is responsible for harvesting electrons [8–12]. Condensation reactions have therefore been advanced to account for the production of emission lines in the chromosphere. These reactions facilitate the deposit of atomic hydrogen onto condensed hydrogen structures, CHS [9, 11, 12]. Line emission in the chromosphere is fundamentally linked to the dissipation of heat associated with exothermic condensation reactions. The role of condensation reactions in the chromosphere of the Sun has previously been presented in substantial detail [9, 11, 12]. For the sake of clarity, it is briefly readdressed herein.

One can consider an atom, A, reacting with hydrogen, H, to give rise to a molecular species, AH [8, 9, 11]. It should be possible for AH and CHS in the chromosphere to form an activated complex, CHS + AH $\rightarrow$ CHS-HA*. This would then be followed by an exothermic step involving the expulsion of an activated atom, CHS-HA* $\rightarrow$ CHS–H + A*, followed by the line emission from A*, A* $\rightarrow$ A + $h\nu$. In such a manner, a viable scheme is presented to account for line emission from neutral atoms, including those from hydrogen itself.

An analogous process could also be applied to a cation, A^{+n}, reacting with hydrogen, H, to give rise to a molecular species, AH^{+n}, where n=1, 2, etc [8, 9, 11]. Reaction of AH^{+n} with a condensed hydrogen structure (CHS) in the chromosphere leads to an activated complex, CHS + AH^{+n} $\rightarrow$ CHS-HA^{+n*}. This would then be followed by an exothermic step involving the expulsion of an activated ion, CHS-HA^{+n*} $\rightarrow$ CHS–H + A^{+n*}, followed by the line emission from the cation, A^{+n*}, A^{+n*} $\rightarrow$ A^+ + $h\nu$. Such reactions have been postulated to play an important role in the chromosphere and can explain the HeII lines, if HeH^+ triggers the condensation [8, 11]. When Ca^+ acts as the initial cation, such a mechanism can account for the strong CaII lines in the Sun [9].

2 'Futile' reactions

There is another class of reactions which may play a role in the Sun, but has previously been overlooked. It is possible for interactions to take place with condensed hydrogen structures, but without the net transfer of a hydrogen atom. This new set of 'futile' reactions is important for three reasons: 1) it offers new insight relative to line emission arising from neutral atoms and molecules, 2) it adds an important new mechanism, which can complement previous reactions [9, 11, 12], in describing spectroscopic linewidths in the chromosphere, and 3) it provides a mechanism which can facilitate condensation reactions in the chromosphere by offering yet another means to dissipate heat.

In biochemistry, futile reactions tend to be cyclic in nature. They involve chemical processes which do not lead to any useful work, but which are exothermic.

A classic example of a futile cycle would involve the reactions of fructose-6-phosphate in glycolysis and gluconeogenesis. During glycolysis, we have a reaction catalyzed by phosphofructokinase: fructose-6-phosphate + ATP → fructose-1,6-bisphosphate + ADP. The reaction is reversed in gluconeogenesis using fructose-1,6-bisphosphatase: fructose-1,6-bisphosphate + H_2O → fructose-6-phosphate + P_i. The overall reaction involves the simple wastage of ATP and energy dissipation without net work: ATP + H_2O→ ADP + P_i + heat. The cell, of course, had to work to make the ATP and as a result, such a cycle is truly futile.

Let us consider the simplest futile reaction in the chromosphere. A hydrogen atom, H, interacts directly with a condensed hydrogen structure to form a weak activated complex, CHS + H → CHS–H^*. But this time, the reaction is reversed and no hydrogen is deposited: CHS–H^* → CHS + H^*. This would then be followed by line emission from activated hydrogen H^*, H^* → H + $h\nu$, as hydrogen is allowed to relax back to the ground state. The reaction appears futile, as no net change has taken place. But on closer examination, it is noted that heat has been removed from the condensed hydrogen structure. As a result, though no additional condensation has occurred, such a futile process can cool the condensing structure, thereby facilitating its growth when other true condensation reactions [8–12] are occurring in parallel.

It is now readily apparent that a wide array of 'futile' processes may exist in the chromosphere. For instance, an atom, A, could react with hydrogen, H, to give rise to a molecular species, AH [8, 9, 11]. AH could interact with CHS in the chromosphere to form an activated complex, CHS + AH → CHS–HA^*. The reaction is reversed and no hydrogen is deposited: CHS–HA^* → CHS + AH^*. This would then be followed by line emission from the molecular species AH^*, AH^* → AH + $h\nu$. In such a manner, a viable scheme is presented to account for line emission from small neutral molecules, such as H_2, CaH, LiH, etc. Similar reactions could also be invoked which involve small molecules such as H_2O or NH_3. The result would be line emission from these molecular species.

The analysis of spectroscopic lineshapes in the Sun is an area of considerable complexity for current models. The wings and cores of many lines appear to change with altitude above the solar surface (see [3, 4, 8, 13] and references therein). Such findings suggest that the mechanism involved in line production might well involve both true condensation reactions and futile processes. As previously stated [8], it is unlikely that Stark mechanisms are truly responsible for the lineshapes we observe in the Sun.

Dedication

Dedicated to past, present, and future astronomers.

Submitted on: January 13, 2014 / Accepted on: January 15, 2014
First published online on: January 18, 2014

References

1. Kirchhoff G. The physical constitution of the Sun. In: *Researches on the Solar Spectrum and the Spectra of the Chemical Elements*. Translated by H.E. Roscoe, Macmillan and Co., Cambridge, 1862, p. 23.
2. Menzel D.H. A Study of the Solar Chromosphere. *Publications of the Lick Observatory*, University of California Press, Berkeley, CA, v. 17, 1931.
3. Thomas R.N. and Athay R.G. Physics of the Solar Chromosphere. Interscience Publishers, New York, N.Y., 1961.
4. Bray R.J. and Loughhead R.E. The Solar Chromosphere (The International Astrophysics Series), Chapman and Hall, London, U.K., 1974.
5. Zirin H. The mystery of the chromosphere. *Solar Phys.*, 1996, v. 169, 313–326.
6. Bahcall J.N. and Pinsonneault M.H. Standard solar models, with and without helium diffusion, and the solar neutrino problem. *Rev. Mod. Phys.*, 1992, v. 64, no.4, 885–926.
7. Robitaille P.M. Liquid metallic hydrogen: A building block for a liquid Sun. *Progr. Phys.*, 2011, v. 3, 60–74.
8. Robitaille P.M. Forty lines of evidence for condensed matter — The Sun on trial: Liquid metallic hydrogen as a solar building block. *Progr. Phys.*, 2013, v. 4, 90–142.
9. Robitaille P.M. The liquid metallic hydrogen model of the Sun and the solar atmosphere IV. On the nature of the chromosphere. *Progr. Phys.*, 2013, v. 3, L15–L21.
10. Robitaille P.-M. The LMH model of the Sun and the solar atmosphere V. On the nature of the corona. *Progr. Phys.*, 2013, v. 3, L22–L25.
11. Robitaille P.M. The liquid metallic hydrogen model of the Sun and the solar atmosphere VI. Helium in the chromosphere. *Progr. Phys.*, 2013, v. 3, L26–L28.
12. Robitaille P.M. The LMH model of the Sun and the solar atmosphere VII. Further insights into the chromosphere and corona. *Progr. Phys.*, 2013, v. 3, L30–L36.
13. Przybilla N. and Butler K. The solar hydrogen spectrum in non-local thermodynamic equilibrium. *Astrophys. J.*, 2004, v. 610, L61–L64.

LETTERS TO PROGRESS IN PHYSICS

Further Insight Relative to Cavity Radiation: A Thought Experiment Refuting Kirchhoff's Law

Pierre-Marie Robitaille

Department of Radiology, The Ohio State University, 395 W. 12th Ave, Columbus, Ohio 43210, USA.
robitaille.1@osu.edu

Kirchhoff's law of thermal emission demands that all cavities contain blackbody, or normal, radiation which is dependent solely on the temperature and the frequency of observation, while remaining independent of the nature of the enclosure. For over 150 years, this law has stood as a great pillar for those who believe that gaseous stars could emit a blackbody spectrum. However, it is well-known that, under laboratory conditions, gases emit in bands and cannot produce a thermal spectrum. Furthermore, all laboratory blackbodies are constructed from nearly ideal absorbers. This fact strongly opposes the validity of Kirchhoff's formulation. Clearly, if Kirchhoff had been correct, then laboratory blackbodies could be constructed of any arbitrary material. Through the use of two cavities in temperature equilibrium with one another, a thought experiment is presented herein which soundly refutes Kirchhoff's law of thermal emission.

If a space be entirely surrounded by bodies of the same temperature, so that no rays can penetrate through them, every pencil in the interior of the space must be so constituted, in regard to its quality and intensity, as if it had proceeded from a perfectly black body of the same temperature, and must therefore be independent of the form and nature of the bodies, being determined by temperature alone. . . In the interior therefore of an opake red-hot body of any temperature, the illumination is always the same, whatever be the constitution of the body in other respects.

Gustav Robert Kirchhoff, 1860 [1]

1 Introduction

Kirchhoff's law [1, 2] is generally considered to be the first amongst the laws governing thermal emission [3–6]. With its formulation, blackbody radiation achieved a magical presence within every cavity. Based on Kirchhoff's law, Planck believed that blackbody radiation had universal significance [6]. It is because of Kirchhoff that Boltzmann's and Planck's constants are viewed as sharing the same quality [5–10]. As such, the collapse of Kirchhoff's law [7–10] has great implication throughout physics. It touches not only condensed matter, but also the very makeup of the stars and our understanding of the microwave background (see [11–13] and references therein). Consequently, many refuse to accept that there can be problems with Kirchhoff's formulation. In so doing, they deny Balfour Stewart proper credit for correctly noting that the emissivity of a material is equal to its absorptivity at thermal equilibrium [14]. Furthermore, *cavity radiation is actually dependent on the nature of the enclosure* [7–10]. As such, a simple thought experiment is now presented which elegantly exposes the error in Kirchhoff's claims.

Cavity radiation revisited

Let us begin with a large perfectly absorbing enclosure - an ideal blackbody (Emissivity (ϵ) = 1, Reflectivity (ρ) = 0; at all temperatures and frequencies), as depicted in Fig. 1. The contents of this cavity are kept under vacuum. Within this outer cavity, let us place a somewhat smaller perfectly reflecting enclosure with 5 sides closed and 1 open ($\epsilon = 0$, $\rho = 1$; at all temperatures and frequencies). Guided by Max Planck [6], both cavities will be large compared to those dimensions which would require the consideration of diffraction. Since the inner cavity is perfectly reflecting, it will also be highly conducting, as good reflectors tend to be good conductors.*

Throughout his classic text on heat radiation [6], Planck makes use of perfectly reflecting enclosures. Therefore, it is appropriate to consider both the perfect emitter ($\epsilon = 1$) and the perfect reflector ($\epsilon = 0$) in this exercise.

At the onset, the experiment requires a mechanical means of closing the inner enclosure. This can be achieved with a mechanism which crosses the walls of the outer cavity while preserving the vacuum. The mechanism is allowed, because laboratory blackbodies are known to possess a small hole in their outer walls through which radiation is typically sampled.

Once this has been accomplished, place the perfectly absorbing enclosure ($\epsilon = 1$, $\rho = 0$), which contains the inner perfectly reflecting cavity ($\epsilon = 0$, $\rho = 1$), in a large helium bath at 4 K. The inner open cavity, is permitted to rest directly on the floor of the outer perfectly absorbing cavity (see Fig. 1). Under these conditions, the inner cavity will achieve temperature equilibrium with the outer cavity using conduction. Radiation inside the perfectly absorbing cavity will correspond

*For example, silver is amongst the best conductors with a resistivity of only ~1.6 x 10^{-8} Ω m at 300 K and of ~0.001 x 10^{-8} Ω m at 4 K [15]. It is also an excellent reflector in the infrared, our frequency range of interest.

Fig. 1: Schematic representation of our thought experiment. A large outer cavity acts as an ideal blackbody ($\epsilon = 1$, $\rho = 0$) and is initially immersed in a helium bath at 4 K. Within this cavity, a perfectly reflecting enclosure ($\epsilon = 0$, $\rho = 1$) rests of the floor with one of its sides initially remaining open.

to black radiation at 4 K. It will fill both the large cavity and the smaller open cavity.

When temperature equilibrium has been reached, permit the inner cavity to be sealed mechanically. At that moment, 4 K blackbody radiation has been trapped inside the smaller perfectly reflecting enclosure.

One can then permit the outer perfectly absorbing enclosure to rise in temperature to 300 K. It will now contain black radiation at that temperature. As for the perfectly reflecting enclosure, it will also move to 300 K, because it can reach temperature equilibrium through conduction (we can use any of 3 mechanisms to reach equilibrium - radiation, conduction, and convection). The inner cavity walls are thus also brought to 300 K. However, unlike the outer cavity which is filled with blackbody radiation at 300 K, the inner cavity remains filled with blackbody radiation at 4 K. Thereby, Kirchhoff's law is proven to be false.

Under these conditions, the only way to enable the inner cavity to hold 300 K blackbody radiation would be to permit a violation of the first and zeroth laws of thermodynamics. Namely, once temperature equilibrium has been reached through conduction, the inner cavity will not be allowed to spontaneously emit photons in search of a new radiative condition, while denying the zeroth law. Photons will not be created where no mechanism exists for their generation.*

In addition, the zeroth law of thermodynamics defines the conditions under which temperature equilibrium exists. These conditions refer to real objects. As long as the outer cavity is in temperature equilibrium with the bath/room and is in temperature equilibrium with the inner cavity; then by definition, the inner cavity is in temperature equilibrium with the bath/room. The nature of the field contained within the inner cavity is not covered by the zeroth law of thermodynamics. As is appropriate, the zeroth and first laws of thermodynamics must guide our judgment relative to Kirchhoff's formulation. Thermal equilibrium is defined as that condition which prevails in the absence of all net changes in conduction, convection, and radiation. Thus, thermal equilibrium has been met when the inner cavity reaches 300 K, despite the fact that it contains 4 K radiation, as there can no longer be any change in net conduction, convection, or radiation, across cavity walls. To argue otherwise implies that the temperature of an object depends on the radiation field it contains. This constitutes a direct violation of the zeroth law of thermodynamics which is independent of radiation fields.

Summary

In this thought experiment, two cavities have been considered and temperature equilibrium between them ensured using conduction. The perfectly absorbing cavity ends up holding perfectly black radiation at all temperatures because its emissivity is 1. But the situation is not the same for the inner cavity, as its emissivity is 0 at all temperatures.

Max Planck previously noted in his classic text on heat radiation that: *"... in a vacuum bounded by totally reflecting walls any state of radiation may persist"* [6, § 51]. In order to ensure that a perfectly reflecting cavity could contain black radiation, he inserted a small particle of carbon (see [9] for a detailed discussion). However, when Planck does so, it is as if he had lined the entire cavity with an excellent absorber, because the carbon particle was identical to graphite, a *nearly perfect absorber*, almost by definition [9]. Planck remains incapable of demonstrating that cavity radiation will always be black, independent of the nature of the walls [7–10].

When the temperature was brought to 300 K, the two cavities responded in different ways as a result of their inherent emissivities. The outer cavity has a perfect emissivity ($\epsilon = 1$) and is able to pump out additional photons, as required by Stefan's law [4]. Since Stefan's law has a fourth power dependence on temperature (T^4), the outer cavity now contains 3.2 x 10^7 times more photons than it did when its temperature was a 4 K. However, the radiation within the inner cavity *persists*, just as Max Planck stated. That is because this cavity lacks the physical mechanism to emit a photon. Until it is opened, it will forever contain black radiation which had cor-

*The emissivity of a material is defined relative to the emissivity of a blackbody at the temperature in question. Selecting an emissivity value for the surface of a cavity therefore implies thermal equilibrium by definition. Yet, in modeling the blackbody problem, computer simulations often perpetually pump photons into cavities, invoke reflection, and build up radiation until they achieve the blackbody spectrum. But real materials cannot act as perpetual sources of photons without dropping in temperature. Obviously, the temperature of a cavity which is already at equilibrium, by definition, cannot be allowed to drop. The pumping of ever more photons into an arbitrary cavity while invoking reflection as a means to justify the buildup of the blackbody spectrum is forbidden by the first law of thermodynamics [10].

responded to that initially produced by the outer cavity when it was at 4 K.

The perfectly absorbing cavity ends up holding perfect black radiation at all temperatures because its emissivity is 1. The perfectly reflecting cavity maintains 4 K radiation, because its emissivity is zero. There is no violation of the first law and the zeroth law guarantees the equilibrium arguments. It is permitted to utilize a perfectly reflecting ($\epsilon = 0$) cavity in this work using the same logic which allows the physics community to hypothesize that perfectly absorbing cavities ($\epsilon = 1$) exist. In reality, both objects cannot be found either in nature, or in the laboratory, over the range of frequencies and temperatures which might be of interest.

The discussion can be extended further to hypothesize, of course, that initial conditions (before the inner cavity was sealed) were at absolute zero. In that case, the inner cavity will always be devoid of radiation once it is closed. Should another initial condition be selected, then, when it is sealed, the inner cavity will contain black radiation at that temperature.

What becomes clear is that the radiation contained in the inner cavity can be made to be absolutely dependent on initial conditions (unrelated to final temperature) and dependent on the nature of the cavity walls. Stewart's law [8, 14] and not Kirchhoff's [1, 2] properly describes the relationship between emission and absorption under conditions of thermal equilibrium.

At the same time, it should be recognized that temperature equilibrium can be achieved without a detailed balance between emission and absorption. This can occur if there is net conduction, convection, or radiation into, or out of, an object whose temperature does not change. For instance, heat could enter through radiation and leave through conduction, while the temperature remains constant. Under these conditions, the object is under temperature equilibrium, but not under thermal equilibrium. Namely, its emission can be much less than its absorption, even if the temperature is not changing. When considering thermal equilibrium and the laws of emission *there must be no net conduction, convection, or radiation*.

This should sufficiently address, in the simplest form, the truth of Kirchhoff's formulation. Based on this presentation, Kirchhoff's law is not valid and the constants of Planck and Boltzmann are not universal.

Acknowledgment

Luc Robitaille is acknowledged for the preparation of Fig. 1.

Dedication

This work is dedicated to my first grandchild, Simone, as this thought experiment was envisioned on the day of her birth while I was driving alone from my home in Columbus to the hospital in Indiana.

Submitted on: January 13, 2014 / Accepted on: January 15, 2014
First published online on: January 18, 2014

References

1. Kirchhoff G. Über das Verhältnis zwischen dem Emissionsvermögen und dem Absorptionsvermogen. der Körper fur Wärme und Licht. *Poggendorfs Annalen der Physik und Chemie*, 1860, v. 109, 275–301. (English translation by F. Guthrie: Kirchhoff G. On the relation between the radiating and the absorbing powers of different bodies for light and heat. *Phil. Mag.*, 1860, ser. 4, v. 20, 1–21).
2. Kirchhoff G. Über den Zusammenhang zwischen Emission und Absorption von Licht und. Wärme. *Monatsberichte der Akademie der Wissenschaften zu Berlin*, sessions of Dec. 1859, 1860, 783–787.
3. Wien W. Über die Energieverteilung in Emissionspektrum eines schwarzen Körpers. *Ann. Phys.*, 1896, v. 58, 662–669.
4. Stefan J. Über die Beziehung zwischen der Warmestrahlung und der Temperature. *Sitzungsberichte der mathematisch naturwissenschaftlichen Classe der kaiserlichen Akademie der Wissenschaften*, Wien 1879, v. 79, 391–428.
5. Planck M. Über das Gesetz der Energieverteilung im Normalspektrum. *Annalen der Physik*, 1901, v. 4, 553–563 (English translation by ter Haar D.: Planck M. On the theory of the energy distribution law in the normal spectrum. The old quantum theory. Pergamon Press, 1967, 82–90; also Planck's December 14, 1900 lecture *Zur Theorie des Gesetzes der Energieverteilung in Normalspectrum*, which stems from this paper, can be found in either German, or English, in: Kangro H. Classic papers in physics: Planck's original papers in quantum physics. Taylor & Francis, London, 1972, 6–14 or 38–45).
6. Planck M. The theory of heat radiation. P. Blakiston's Son & Co., Philadelphia, PA, 1914.
7. Robitaille P.-M. On the validity of Kirchhoff's law of thermal emission. *IEEE Trans. Plasma Sci.*, 2003, v. 31, no. 6, 1263–1267.
8. Robitaille P.-M. A critical analysis of universality and Kirchhoff's law: A return to Stewart's law of thermal emission. *Progr. Phys.*, 2008, v. 3, 30–35.
9. Robitaille P.-M. Blackbody radiation and the carbon particle. *Progr. Phys.*, 2008, v. 3, 36–55.
10. Robitaille P.-M. Kirchhoff's law of thermal emission: 150 Years. *Progr. Phys.*, 2009, v. 4, 3–13.
11. Robitaille P.-M. Blackbody radiation and the loss of universality: Implications for Planck's formulation and Boltzmann's constant. *Progr. Phys.*, 2009, v. 4, 14–16.
12. Robitaille P.-M. Water, hydrogen bonding, and the microwave background. *Progr. Phys.*, 2009, v. 2, L5–L8.
13. Robitaille P.-M. Fourty lines of evidence for condensed matter - The Sun on trial: Liquid metallic hydrogen as a solar building block. *Progr. Phys.*, 2013, v. 4, 90–142.
14. Stewart B. An account of some experiments on radiant heat, involving an extension of Prévost's theory of exchanges. *Trans. Royal Soc. Edinburgh*, 1858, v. 22, no. 1, 1–20 (also found in Harper's Scientific Memoirs, edited by J.S. Ames: The Laws of Radiation and Absorption: Memoirs of Prévost, Stewart, Kirchhoff, and Kirchhoff and Bunsen, translated and edited by D.B. Brace, American Book Company, New York, 1901, 21–50).
15. Electrical Resistivity of Pure Metals. In, *CRC Handbook of Chemistry and Physics*, 2013–2014, CRC Press, Baca Raton, FL, p. 12-42.

ΔI=2 Nuclear Staggering in Superdeformed Rotational Bands

Madiha D. Okasha

Physics Department, Faculty of Science (Girls College), Al-Azhar University, Cairo, Egypt. E-mail: mady200315@yahoo.com

A four parameters model including collective rotational energies to fourth order is applied to reproduce the ΔI=2 staggering in transition energies in four selected super deformed rotational bands, namely, ^{148}Gd (SD6), ^{194}Hg (SD1, SD2, SD3). The model parameters and the spin of the bandhead have been extracted assuming various values to the lowest spin of the bandhead at nearest integer, in order to obtain a minimum root mean square deviation between calculated and the experimental transition energies. This allows us to suggest the spin values for the energy levels which are experimentally unknown. For each band a staggering parameter represent the deviation of the transition energies from a smooth reference has been determined by calculating the fourth order derivative of the transition energies at a given spin. The staggering parameter contains five consecutive transition energies which is denoted here as the five-point formula. In order to get information about the dynamical moment of inertia, the two point formula which contains only two consecutive transition energies has been also considered. The dynamical moment of inertia decreasing with increasing rotational frequency for $A \sim 150$, while increasing for $A \sim 190$ mass regions.

1 Introduction

The observation [1] of a very regular pattern of closely spaced γ-transitions in the spectrum of ^{152}Dy, which assigned to a rotational cascade between levels of spin ranging from $60\hbar$ to $24\hbar$ and excitation energy varying from ~ 30 to 12 MeV may adopt a superdeformed (SD) at high angular momentum. The moment of inertia of the associated band was found to be close to that of a rigid rotor with a 2:1 axis rotation. Now more than 350 settled superdeformed rotational bands (SDRB's), in more than 100 nuclei have been studied in nuclei of mass A ~ 30, 60, 80, 130, 150, 160, 190 [2, 3]. Such nuclei are associated with extremely large quadrupole $\beta_2 = 0.6$ in the mass A ~ 150 region and $\beta_2 = 0.47$ in the mass A ~ 190 region. Hence, they are expected to have a different structures to normal deformed nuclei.

Unfortunately, despite the rather large amount of experimental information on SDRB's, there are still a number of very interesting properties, which have not yet been measured. For example, the spin, parity and excitation energy relative to the ground state of the SD bands. The difficulty lies with observing the very weak discrete transitions which link SD levels with levels of normal deformation (ND). Several related approaches to assign the spins of SDRB's in terms of their observed γ-ray transition energies were proposed [4–10]. For all approaches an extrapolation fitting procedure was used.

It was found that some SDRB's show an unexpected ΔI=2 staggering in their γ-ray transition energies [11–20]. The SD energy levels are consequently separated into two sequences with spin values I, I+4, I+8, ...and I+2, I+6, I+10, ... respectively. The magnitude of splitting is found to be of some hundred eV to a few keV. Several theoretical explanation have been made. One of the earliest ones being based on the assumption of a C4 symmetry [21]. Also it was suggested that [22] the staggering is associated with the alignment of the total angular momentum along the axis perpendicular to the long deformation axis of a prolate nucleus. The staggering phenomenon was interpreted also as due to the mixing of a series of rotational bands differ by ΔI=4 [23] or arise from the mixing of two bands near yrast line [24] or by proposing phenomenological model [25, 26]. The main purpose of the present paper is to predict the spins of the bandhead of four SDRB's in A ~ 150 and A ~ 190 mass regions, and to examine the ΔI=2 staggering and the properties of the dynamical moments of inertia in framework of proposed four parameters collective rotational model.

2 Nuclear SDRB's in Framework of Four Parameters Collective Rotational Model

On the basis of collective rotational model [27] in adiabatic approximation, the rotational energy E for an axial symmetric nucleus can be expanded in powers of I(I+1), where I is the spin of state:

$$E(I) = A[I(I+1)]+B[I(I+1)]^2+C[I(I+1)]^3+D[I(I+1)]^4 \quad (1)$$

where A is the well-known rotational parameter for sufficiently small values of I and B, C, D are the corresponding higher order parameters. In the view of the above mentioned, it seems that the ground state energy bands of deformed even-even nucleus have quantum number K=0 (K is the projection of I along the symmetry axis), together with even parity and angular momentum. In SD nuclei, the experimentally determined quantities are the gamma ray transition energies between levels differing by two units of angular momentum, then we could obtain the reference transition energy

$$E_\gamma^{ref} = E(I)-E(I-2) \quad (2)$$

Table 1: The calculated adopted best parameters and the bandhead spins for the selected SD nuclei to investigate the $\Delta I = 2$ staggering.

SD-Band	A (keV)	B (keV) $\times 10^4$	C (keV) $\times 10^8$	D (keV) $\times 10^{12}$	I ($\hbar$)	E_γ (MeV)
^{148}Gd (SD-6)	4.33360	1.17108	0.001135	-0.04435	41	802.200
^{194}Hg (SD-1)	5.40524	-1.86747	0.000338	-0.00213	8	211.700
^{194}Hg (SD-2)	5.24253	-1.577380	0.003991	-0.00269	8	200.790
^{194}Hg (SD-3)	5.21638	-1.48121	0.0006129	-0.006501	9	222.000

$$\begin{aligned} E_\gamma^{ref} &= 2(2I-1)[A+2(I^2-I+1)B \\ &+ (3I^4-6I^3+13I^2-10I+4)C \\ &+ 4(I^6-3I^5+10I^4-15I^3+15I^2-8I+2)D]. \end{aligned} \quad (3)$$

The rotational frequency is not directly measurable but it is related to the observed excitation energy E.

Let us define the angular velocity of nuclear rotation as the derivative of the energy E with respect to the angular momentum I in analogy with classical mechanics. Instead of I it is convenient to use the quantum mechanical analogies $\sqrt{(I(I+1))}$

$$\hbar\omega = \frac{dE}{d\left(\sqrt{(I(I+1))}\right)} \quad (4)$$

$$\begin{aligned} &= 2A[I(I+1)]^{1/2} + B[I(I+1)]^{3/2} \\ &+ 6C[I(I+1)]^{5/2} + 8D[I(I+1)]^{7/2}. \end{aligned} \quad (5)$$

The rotational energy spectra can be discussed in terms of the dynamical moment of inertia calculated from the reciprocal second order derivative:

$$\frac{J^{(2)}}{\hbar^2} = \left(\frac{d^2E}{d\left(\sqrt{I(I+1)}\right)^2}\right)^{-1} \quad (6)$$

$$\begin{aligned} &= \Big([2A + 12B[I(I+1)] \\ &+ 30C[I(I+1)]^2 + 56D[I(I+1)]^3]\Big)^{-1}. \end{aligned} \quad (7)$$

The experimental $\hbar\omega$ and $J^{(2)}$ for the SDRB's are usually extracted from the observed energies of gamma transition between two consecutive transitions within the band from the following formulae:

$$\hbar\omega = [E_\gamma(I) + E_\gamma(I+2)]/4, \quad (8)$$

$$J^{(2)} = \frac{4}{E_\gamma(I+2) - E_\gamma(I)}. \quad (9)$$

We notice that $\hbar\omega$ and $J^{(2)}$ does not depend on the knowledge of the spin I, but only on the measured gamma ray energies.

In order to see the variation in the experimental transition energies $E_\gamma(I)$ in a band, we subtract from them a calculated reference. The corresponding five-point formula is the fourth order derivative of the transition energies at a given spin

$$\begin{aligned} \Delta^4 E_\gamma(I) &= \frac{1}{16}[E_\gamma(I+4) - 4E_\gamma(I+2) \\ &+ 6E_\gamma(I) - 4E_\gamma(I-2) + E_\gamma(I-4)]. \end{aligned} \quad (10)$$

One can easily see that $\Delta^4 E_\gamma(I)$ vanishes if our model contains two parameters A and B, due to the fact that the five-point formula is a normalized discrete approximation of the fourth derivatives of the function $E_\gamma(I)$. We define the staggering parameter $S^{(4)}(I)$ as the difference between the experimental transition energies and the auxiliary reference.

$$S^{(4)}(I) = 2^4[\Delta^4 E_\gamma^{exp}(I) - \Delta^4 E_\gamma^{ref}(I)] \quad (11)$$

3 Numerical Calculations and Discussions

The transition energies $E_\gamma(I)$ of equation (2) is used to fit the observed transition energies for our selected SDRB's with A, B, C, D and spin value of the bandhead I_0 as free parameters. I_0 is taken to the nearest integer of the fitting, the another fit is made to determine A, B, C and D by using a simulated search program [9] in order to obtain a minimum root mean square deviation

$$\chi = \left[\frac{1}{N}\sum_{i=1}^{N}\left(\frac{E_\gamma^{exp}(I) - E_\gamma^{Cal}(I)}{\triangle E_\gamma^{exp}(I)}\right)\right]^{1/2}$$

of the calculated transition energies E_γ^{Cal} from the measured energies E_γ^{exp}, where N is the number of data points considered, and ΔE_γ^{exp} is the uncertainty of the γ-transition energies. The experimental data for transition energies are taken from ref. [2]. Table (1) summarize the model parameters A, B, C, D and the correct bandhead lowest level spin I_0 and also the lowest γ- transition energies $E_\gamma(I_0 + 2 \rightarrow I_0)$ for our 4 SDRB's.

To investigate the appearance of staggering effects in the γ-transition energies of our selected SDRB's, for each band, the deviation of the γ-transition energies $E_\gamma(I)$ from a smooth reference (rigid rotor) was determined by calculating fourth-derivatives of $E_\gamma(I)$ (d^4E_γ/dI^4) at a given spin I by using the finite difference approximation. The resulting staggering parameters values against spin are presented in Figure (1). A significant ΔI=2 staggering was observed. At high spins the

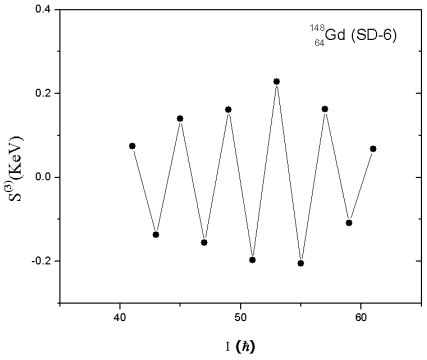

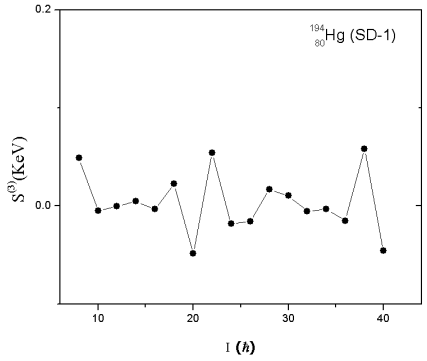

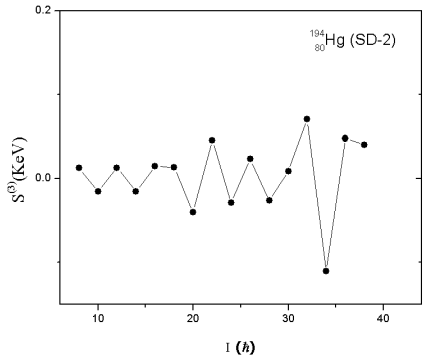

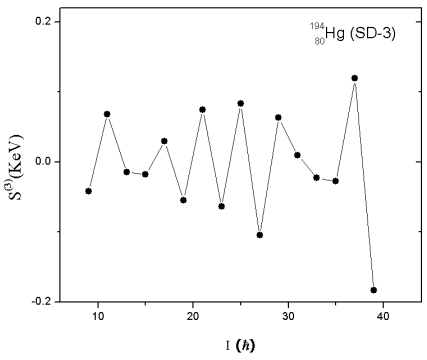

Fig. 1: The calculated $\Delta I = 2$ staggering parameters $S^{(4)}(I)$ obtained by five-point formula versus nuclear spin I for the SDRB's in ^{148}Gd and ^{194}Hg.

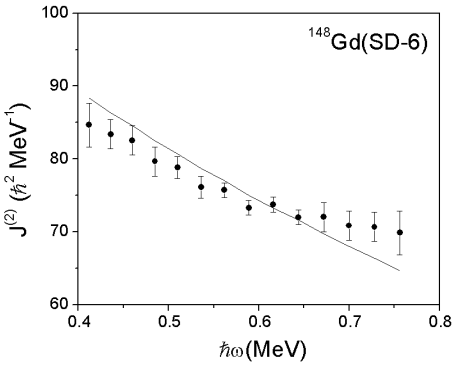

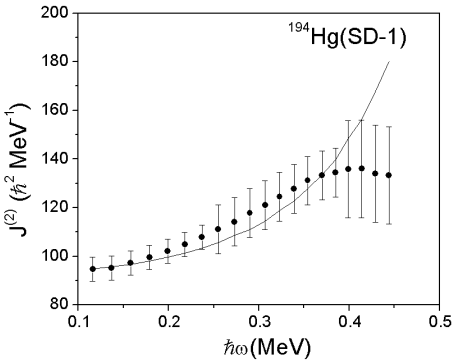

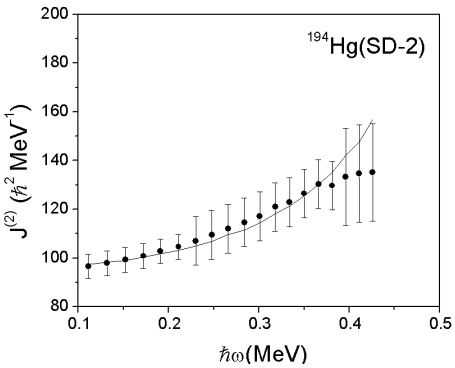

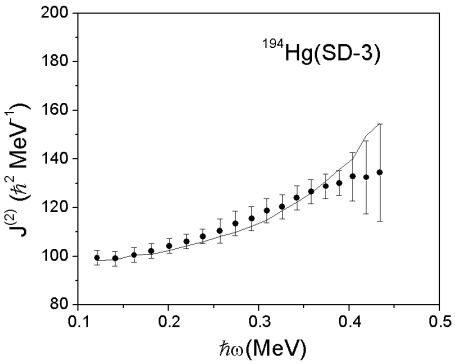

Fig. 2: The dynamical moment of inertia $J^{(2)}$ plotted as a function of the rotational frequency $\hbar\omega$ for the SDRB's in ^{148}Gd and ^{194}Hg nuclei. The solid curve represents the calculated results extracted from the proposed four parameters model. The experimental solid circles with error bars are presented for comparison.

ΔI=2 rotational band is perturbed and two ΔI=4 rotational sequences emerge with an energy splitting of some hundred eV. That is the E2 cascades obtained from our model exhibit for spins I, I+4, I+8, ... and I+2, I+6, I+10, ... staggering behavior.

The systematic behavior of the dynamic moment of inertia $J^{(2)}$ is very useful to understand the properties and structure of SDRB's. Our best fitted parameters were used to calculate the theoretical $J^{(2)}$. The evolution of the dynamical moment of inertia $J^{(2)}$ against rotational frequency $\hbar\omega$ are illustrated in Figure (2). It is seen that the agreement between the calculated (solid lines) and the values extracted from the observed data (closed circles) are excellent. For A∼190, the SDRB's have nearly the same $J^{(2)}$ which typically increase smoothly as rotational frequency increases due to gradual angular momentum alignment of a pair of nucleons occupying specific high-N intruder orbitals and the disappearance of pairing correlations. For A∼150 a smooth decrease of $J^{(2)}$ with increasing $\hbar\omega$ is reproduced well.

Submitted on January 02, 2014 / Accepted on January 10, 2014

References

1. Twin P.J., Nyak B.M. Observation of a Discrete-Line Superdeformed Band up to 60$\hbar$ in ^{152}Dy. *Physical Review Letters*, 1986, v. 57, 811–814.
2. Singh Balraj. Table of Superdeformed Nuclear Bands and Fission Isomers. *Nuclear Data Sheets*, 2006, v. 107, 1–224.
3. Singh Balraj, Zywine Roy, Richard B. Firestone. Table of Superdeformed Nuclear Bands and Fission Isomers. *Nuclear Data Sheets*, 2002, v. 97 (1), 241–592.
4. Draper J.E., Stephens F.S. et al. Spins in superdeformed bands in the mass 190 region. *Physical Review*, 1990, v. C42, R1791–R1795 .
5. Stephens F.S. Spin alignment in superdeformed rotational bands. *Nuclear Physics*, 1990, v. A520, c91–c104.
6. Becker J.A., Henry E.A. et al. Level spin for superdeformed nuclei near A=194. *Physical Review*, 1992, v. C46, 889–903.
7. Khalaf A.M., Allam M.A. and Sirag M.M. Bandhead Spin Determination and Moments of inertia of Superdeformed Nuclei in Mass Region 60-90 Using Variable Moment of inertia Model. *Egypt Journal of Physics*, 2010, v. 41(2), 13–27.
8. Khalaf A.M., Taha M.M. and Kotb M. Studies of Superdeformation in Gadolinium Nuclei Using Three-Parameters Rotational Formula. *Progress in Physics*, 2012, v. 4(2), 39–44.
9. Khalaf A.M. et al. Bandhead Spin Determination and Moments of inertia of Superdeformed Nuclei in Mass Region 60-90 Using Variable Moment of inertia Model. *Progress in Physics*, 2013, v. 3(2), 39–44.
10. Khalaf A.M., Sirag M.M. and Taha M.M. Spin Assignment and Behavior of Superdeformed Bands in A∼150 Mass Region. *Turkish Journal of Physics*, 2013, v. 37, 49–54.
11. Flibotte S. et al. ΔI=4 bifurcation in a superdeformed band: Evidence for a C_4 symmetry band. *Physical Review Letters*, 1993, v. 71, 4299–4302.
12. Cederwall B. et al. New features of superdeformed bands in ^{194}Hg. *Physica Scripta*, 1994, v. 72, 3150–3153.
13. Flibotte S., Hackman G. et al. Multi-particle excitations in the superdeformed ^{149}Gd nucleus. *Nuclear Physics*, 1995, v. A584, 373–396.
14. Carpenter M.P., Janssens R.V.F. Identification of the unfavored N=7 superdeformed band in ^{191}Hg. *Physical Review*, 1995, v. 51, 2400–2405.
15. Farris L.P., Henry E.A. et al. Neutron blocking and delayed proton pair alignment in superdeformed ^{195}Pb. *Physical Review*, 1996, v. C51, R2288–R2292.
16. Bernstein L.A. and Hughes J.R. Superdeformation in ^{154}Er. *Physical Review*, 1995, v. C52, R1171–R1174.
17. de Angelis G. and Wyss R. Spectroscopy in the second well of the^{148}Gd nucleus. Two quasiparticle and collective excitations. *Physical Review*, 1996, v. C53, 679–688.
18. Fischer S.M., Carpenter M.P. et al. Alignment additivity in the two-quasiparticle superdeformed bands of ^{192}Tl. *Physical Review*, 1996, v. C53, 2126–2133.
19. Semple A.T. and Nolan P.J. Energy Staggering in Superdeformed bands in ^{131}Ce, ^{132}Ce and ^{133}Ce. *Physical Review Letters*, 1996, v. 76, 3671–3674.
20. Haslip D.S., Flibotte1 S. and de France G. ΔI= 4 Bifurcation in Identical Superdeformed Bands. *Physical Review Letters*, 1997, v. 78, 3447–3450.
21. Hamamoto I. and Mottleson B. Superdeformed rotational bands in the presence of $_{44}$Y deformation. *Physics Letters*, 1994, v. B333, 294–298.
22. Pavlichenkov I.M. and Flibotte S. C_4 symmetry and bifurcation in superdeformed bands. *Physical Review*, 1995, v. C51, R460–R464.
23. Macchiavell A.O. et al. C_4 symmetry effects in nuclear rotational motion. *Physical Review*, 1995, v. C51, R1–R4.
24. Sun Y., Zhang Z. and Guidry M. ΔI = 4 Bifurcation without Explicit Fourfold Symmetry. *Physical Review Letters*, 1995, v. 75(1), 3398–3401.
25. Khalaf A.M. and Sirag M.M. Analysis of ΔI = 2 Staggering in Nuclear Superdeformed Rotational Bands. *Egypt Journal of Physics*, 2004, v. 35(2), 359–375.
26. Sirag M.M. Reexamination of ΔI = 2 Energy Staggering in Nuclear Superdeformed Rotational Bands. *Egypt Journal of Physics*, 2007, v. 35(1), 1–14.
27. Bohr A. and Mottelson B. Nuclear Structure. W. A. Benjamin Inc., New York 1975.

Lorentzian Type Force on a Charge at Rest

Rudolf Zelsacher

Infineon Technologies AG, Siemensstrasse 2 A-9500 Villach, Austria. E-mail: Rudolf.zelsacher2@infineon.com

A remarkable achievement of theoretical physics is the explanation of magnetic effects, described by the Lorentz force, to be corollaries of charge invariance, Coulombs Law and the Lorentz transformation. The relativistic explanation of magnetism is based essentially on the calculation of Coulomb forces between moving charges in the laboratory reference system. We will show presently that the ideas used for the relativistic explanation of magnetism also lead to a force on a charge at rest by moving charges, which we dub "Lorentzian type force on a charge at rest".

1 Introduction

1.1 Miscellaneous

We will follow very closely the chain of thought taken by Edward Mills Purcell in [1]. We will use the Gaussian CGS units in order to underline the close relationship between electric field $\mathbf{E}(x, y, z, t)$ and magnetic field $\mathbf{B}(x, y, z, t)$. We will use as our reference frame $F[x, y, z, t]$, the idealized laboratory inertial frame, abbreviated to lab, to describe the location of particles and fields at time t. We will use other reference systems like $F'[x', y', z', t']$ with axes parallel with respect to F, with the origins of these systems coinciding at $t = t' = 0$ and with F' being in uniform relative motion with respect to F in either the positive or negative x direction.

Table 1: Definition of symbols

symbol	description
F	inertial frame/system
$\mathbf{F}$	also for force
$\mathbf{p}$	momentum
q	charge
$\mathbf{B}$	magnetic field
$\mathbf{E}$	electric field
a	surface
S	surface
(x, y, z)	space coordinates
t	time
c	speed of light in vacuum
v	velocity
I	current
l	length
β	$\frac{v}{c}$
γ	$\frac{1}{\sqrt{1-\beta^2}}$
m	rest mass
$\hat{\mathbf{x}}, \hat{\mathbf{y}}, \hat{\mathbf{z}}, \hat{\mathbf{r}}$	unit vector in the indicated direction

1.2 The charge and the mass of moving charged particles

The conclusion of the experimental findings is that charge is quantized and invariant in all stages of relative motion, and can be calculated by Gauss's Law [1]

$$q' = q\,. \tag{1}$$

Mass changes with velocity, charge does not. The fact that mass changes with velocity finds its mathematical formulation through the introduction of relativistic momentum [2]

$$\mathbf{p} = m\mathbf{v}\gamma \tag{2}$$

and relativistic energy $E = mc^2\gamma$. Eq. 2 is the starting point for the derivation of forces in inertial systems connected by the Lorentz transformation.

1.3 The electric fields E in F arising from a point charge q at rest in F' and moving with v in F

The electric field $\mathbf{E}$ in F of a charge moving uniformly in F, at a given instant of time, is generally directed radially outward from its instantaneous position and given by [1]

$$\mathbf{E}(\mathbf{R}, \vartheta) = \frac{q\left(1-\beta^2\right)}{R^2\left(1-\beta^2\sin^2\vartheta\right)^{\frac{3}{2}}}\,\hat{\mathbf{R}}\,. \tag{3}$$

R is the length of $\mathbf{R}$, the radius vector from the instantaneous position of the charge to the point of observation; ϑ is the angle between the direction of motion of the charge q $\mathbf{v}\Delta t$ and $\mathbf{R}$. Eq. 3, multiplied by Q, tells us the force on a charge Q at rest in F caused by a charge q moving in F (q is at rest in F').

1.4 The relativistic explanation of magnetism

In Fig. 1 we have sketched the model given in [1] to explain magnetic effects by relativistic arguments. The calculation of the force on q gives

$$F'_y = \frac{dp'_y}{dt'} = qE' = \frac{2q}{\gamma_0 r'}\left(\gamma'_+\lambda_+ + \gamma'_-\lambda_-\right) = \frac{\gamma 4q\lambda v v_0}{r'c^2}. \tag{4}$$

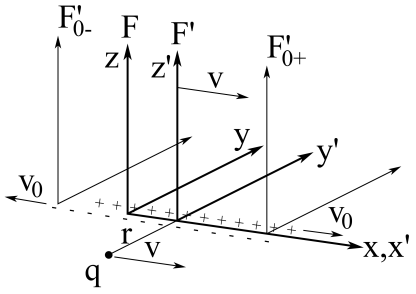

Fig. 1: We show a positive line charge distribution λ_+, stationary in reference frame F'_{0+}, moving in F in the positive x-direction with v_0, and a negative line charge distribution λ_- at rest in F'_{0-}, moving in F in the negative x-direction with v_0. A positive charge q, at rest in F', moves with v in F in the positive x-direction In F the electric fields sum up to **0** because by definition $\lambda_+ + \lambda_- = 0$. In F', the rest frame of charge q, there is an electric field **E' ≠ 0** due to fields transformed from the rest frame of λ_+ and λ_- to F'. The resulting force in F' on q, $d\mathbf{p}'/dt'$, is then transformed to F, the *lab* frame, where we observe the charge q.

The resulting force $d\mathbf{p}'/dt'$ on charge q in F' is transferred to F, the *lab* system, where we do the experiments, giving $F_y = \frac{dp_y}{dt} = \frac{dp'_y}{\gamma dt'}$, and has the value [1]

$$\mathbf{F} = \frac{4q\lambda v v_0}{rc^2}\,\hat{\mathbf{y}} = \frac{2qvI}{rc^2}\,\hat{\mathbf{y}} = \frac{qv}{c}\,\frac{2I}{rc}\,\hat{\mathbf{y}} \qquad (5)$$

with $\lambda = |\lambda_+| = |\lambda_-|$.

As was discovered well before the advent of relativity, the overall effect of currents on a moving charge can also be described completely by introducing the magnetic field **B** in the *lab* frame F and equating the Lorentz force to $d\mathbf{p}/dt$. The magnetic field **B** is calculated with Biot-Savart's Law. The main purpose of the derivation, which results in Eq. 5, is to explain how nature works, and to demonstrate how the physical entity "magnetic field" can be revealed using more fundamental physical laws, specifically Coulomb's law and the laws of special relativity [1].

2 Lorentzian type force on a test charge Q at rest

We consider now two very narrow wires isolated along their length, but connected at the ends, each having length 2a and lying in lab coaxial to the x-axis of F from $x = -a$ to $x = a$. In addition the system has a source of electromotive force applied so that a current I is flowing through the wires: in one of the wires I flows in the positive x direction and in the other wire I flows in the negative x direction. We also have in mind two wires forming a thermocouple or two superconducting wires. On the z-axis of F fixed (at rest) at (0, 0, h) a test charge Q is located.

The system is sketched in Fig. 2. We will now calculate the force $\mathbf{F}_{Lt}$ on the stationary test charge Q fixed at (0, 0, h)

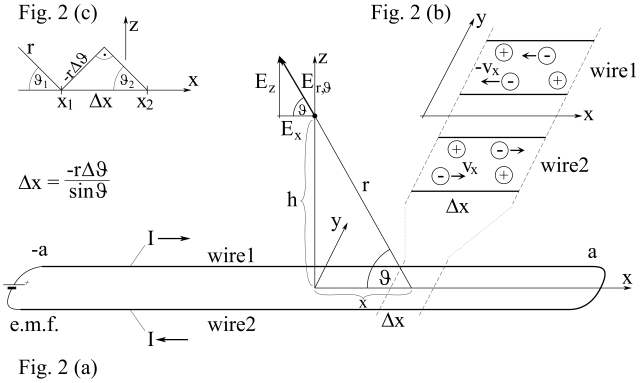

Fig. 2: (a) (b) (c): We show in Fig. 2(a) the two wires carrying the current I extended along the x axis of F from $x = -a$ to $x = a$ and the charge Q at rest in F at (0, 0, h). Additionally on the right-hand side a magnification of a small element Δx containing the two wires and labeled Fig. 2(b) can be seen. Fig. 2(b) shows some moving electrons and for each of these the nearest neighboring proton situated in the tiny element. We calculate the force on Q by precisely these pairs of charges. The effects of the other immobile electrons and protons of element Δx sum up to **0**. On the left-hand side another magnification of element Δx labeled Fig. 2(c) can be seen, showing some geometrical relations useful for integration.

due to the electrons of current I and their nearest stationary protons.

The two wires are electrically neutral before the current is switched on. Therefore after the current is switched on we have an equal number of N electrons and N protons in the system — the same number N, as with the current switched off. We look at the system at one instant of lab time t_0, after the current I is switched on and is stationary. We divide the wires into sections having lengths Δx_i. In each such element we consider the k_i electrons that make up the current I. For each of these k_i electrons e_{ij} with $j = 1, 2, \ldots k_i$, having velocity $\pm v_x$, which are defining the current I in Δx_i, we select the nearest neighboring stationary proton p_{ij} with $j = 1, 2, \ldots k_i$, with the restriction that the proton must lie in Δx_i. "Stationary" means that the charges retain their mean position over time. The effects on Q by the residual K_i stationary protons and K_i stationary electrons present in this element Δx_i sum up to **0**. The number of electrons and protons in the system is given by $N = \sum_i (K_i + k_i)$. For each charge of the mobile electron-stationary proton pairs present in Δx_i, we use the same $\mathbf{r}_i$ as the vector from each of the charges to Q. We use $\vartheta_i = \arcsin\frac{h}{r_i}$, the angle between the x-axis and $\mathbf{r}_i$, for each charge of the pairs of charges present in Δx_i. In Fig.3 we have sketched the situation for one pair of charges.

Referring to Fig. 2 we conclude that the line charge density λ and k_i, the number of current electrons moving with $|v_x|$ in Δx_i, and the line charge density λ and the k_i immobile

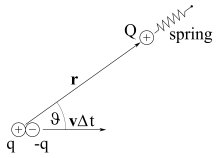

$$\mathbf{F}_Q = \frac{d\left(m\mathbf{v}_Q\gamma_Q\right)}{dt} =$$

$$-\frac{qQ}{r^2}\left(\frac{\left(1-\beta^2\right)}{\left(1-\beta^2\sin^2\vartheta\right)^{\frac{3}{2}}}-1\right)\hat{\mathbf{r}}+\mathbf{F}_{spring}=\mathbf{0}$$

$q \quad \mathbf{v}=\mathbf{0}$ at rest in laboratory

$-q \quad \mathbf{v}\neq\mathbf{0}$ moving in laboratory

$Q \quad \mathbf{v}_Q=\mathbf{0}$ at rest in laboratory

$$\beta=\frac{v^2}{c^2} \quad \gamma_Q=\left(1-\frac{v_Q{}^2}{c^2}\right)^{-\frac{1}{2}}$$

Fig. 3: We show a positive immobile charge q at rest in *lab* and a negative moving charge $-q$ moving in *lab* and the resulting electrical force on a positive charge Q at rest in *lab*. q and $-q$ are one of the pairs of charges that we select at time t_0 in Δx to calculate the effects of the current I on charge Q at rest in *lab*.

protons of Δx_i are both related by

$$k_i = \frac{|\lambda|\Delta x_i}{e} \tag{6}$$

with $e = 4.803^{-10}[esu]$. By doing so we replace the use of the relativistic length contraction by counting charges. We use the same distance $r_i(t_0)$ from Q to the k_i moving electrons and from Q to the k_i immobile protons. We now calculate the force on Q from exactly these charges, i.e. k_i electrons moving with $|v_x|$ and k_i immobile protons. In Figure 2(c) we sketched the model and some geometrical relations which are used below.

With

$$\Delta x = -\frac{r\Delta\vartheta}{\sin\vartheta} \tag{7}$$

and with

$$r = \frac{h}{\sin\vartheta} \tag{8}$$

we get

$$\Delta E_z = \frac{\lambda\left(1-\beta^2\right)\sin\vartheta\Delta\vartheta}{h\left(1-\beta^2\sin^2\vartheta\right)^{\frac{3}{2}}} - \frac{\lambda\sin\vartheta\Delta\vartheta}{h}. \tag{9}$$

Now we have to sum up over all elements Δx_i (or $\Delta\vartheta_i$). We do this by multiplying Eq. 9 by 4 and by integrating from $\vartheta = \frac{\pi}{2}$ to $\vartheta_{min} = \arctan\frac{h}{a}$. For the first term we substitute $u = \beta\cos\vartheta$ and use $\int \frac{du}{\left(a^2+u^2\right)^{\frac{3}{2}}} = \frac{u}{a^2\left(a^2+u^2\right)^{\frac{1}{2}}}$ and finally obtain

$$E_z = \frac{4\lambda\cos\vartheta_{min}}{h}\left(1-\frac{1}{\left(1-\beta^2\sin^2\vartheta_{min}\right)^{\frac{1}{2}}}\right) \approx$$

$$-\frac{2Iv_x\cos\vartheta_{min}\sin^2\vartheta_{min}}{hc^2}.$$

The force on Q, — the "Lorentzian type force on a charge at rest" — is then

$$\mathbf{F}_{Lt} = -\frac{Q\,2Iv_x\cos\vartheta_{min}\sin^2\vartheta_{min}}{hc^2}\,\hat{\mathbf{z}}; \tag{10}$$

q.e.d.

The force described by Eq. 10 is of the same order (e.g. for $\vartheta_{min} = \frac{\pi}{3}$) of magnitude as magnetic forces, as can be seen by comparing it to Eq. 5 (repeated below), but it acts on a charge Q which has zero velocity. Find Eq. 5 written again below

$$\mathbf{F} = \frac{4q\lambda v v_0}{rc^2}\,\hat{\mathbf{y}} = \frac{2qvI}{rc^2}\,\hat{\mathbf{y}} = \frac{qv}{c}\frac{2I}{rc}\,\hat{\mathbf{y}} \qquad \text{(5 repeated)} \tag{11}$$

for easier comparison with Eq. 10.

Discussion

Whenever new concepts and ideas are introduced in physics, it is to be expected that they not only adequately explain the existing findings, but also enable new predictions that are falsifiable by experimental means. The Lorentz force leaves no room for a force on a charge at rest caused by moving charges, because the velocity of the charge at rest is, of course, zero. But the ideas and methods of special relativity, when used to explain magnetism, show that such a force — a force of moving charges which are part of a neutral piece of matter containing the same number of electrons and protons — exerted on a charge at rest, a certain distance away of the above mentioned piece of matter, is possible. We have shown this by reproducing the derivation of magnetism by relativistic arguments given in [1] step-by-step and applying it to our system of wires and charges. We could have calculated the fields and forces on Q in a reference system F' where Q is at rest and transformed the result to F or lab to formally and completely reproduce the derivation of magnetism using relativity, resulting in Eq. 5 as shown in [1] and section 1.4. But as Q is at rest in lab, and therefore at rest in reference frame F, we have calculated the effects on Q due to moving charges directly in F using Eq. 3. Of course we then no longer need to transfer the rate of change of momentum to F because it is directly given in the frame F in which Q is at rest. In addition we have replaced the line charge variations in different reference frames due to the Lorentz-Fitzgerald length contraction used in [1] by defining pairs of moving current electrons and their nearest neighbor immobile protons to calculate the effects on the charge Q. In other words we have replaced the use of the Lorentz-Fitzgerald contraction by counting charges, and counting is relativistically invariant. The basic idea for the calculation of $\mathbf{F}_{Lt}$ manifestations is the use of pairs of moving and immobile charges. If the Lorentzian type force on a charge at rest cannot be found by experiment, and we have no hint that it exists, at least the derivation leading to Eq. 3, written down in [1], should be subject to a revision.

Acknowledgements

I am grateful to Thomas Ostermann for typesetting the equations and to Andrew Wood for correcting the English.

Submitted on January 14, 2014 / Accepted on January 24, 2014

References

1. Purcell E. M. Electricity and Magnetism. McGraw-Hill Book Company, New York, 1964.
2. Kittel C. et al. Mechanics. 2nd Edition, McGraw-Hill Book Company, New York, 1973.

Flow of Viscous Fluid between Two Parallel Porous Plates with Bottom Injection and Top Suction

Hafeez Y. Hafeez[1] and Chifu E. Ndikilar[2]

[1]Physics Department, Federal University Dutse, Nigeria. E-mail: hafeezyusufhafeez@gmail.com
[2] Physics Department, Federal University Dutse, Nigeria. E-mail: ebenechifu@yahoo.com

This paper deals with the problem of steady laminar flow of viscous incompressible fluid between two parallel porous plates with bottom injection and top suction. The flow is driven by a pressure gradient $\frac{\partial p}{\partial x}$ and uniform vertical flow is generated i.e. the vertical velocity is constant everywhere in the field flow i.e. $v = v_w = constant$. Also a solution for the small and large Reynold number is discussed and the graph of velocity profile for flow between parallel plates with the bottom injection and top suction for different values of Reynold numbers is drawn.

1 Introduction

The two dimensional steady laminar flow in channels with porous walls has numerous application in field of Science and Engineering through boundary layer control, transpiration cooling and biomedical enginering.

Berman (1953) was the first reasercher who studied the problem of steady flow in an incompressible viscous fluid through a porous channel with rectangular cross section, when the Reynold number is low and the pertubation solution assuming normal wall velocity to be equal was obtained [1].

Sellars (1955), extended problem studied by Berman by using very high Reynold numbers [2].

Yuan (1956) [3] and Terill (1964) [4] analysed the same problem assuming different normal velocity at the wall.

Terrill and Shrestha (1965) analysed the problem for a flow in a channel with walls of different permeabilities [5].

Green (1979) studied the flow in a channel with one porous wall [7].

In this paper, we considered the flow of an incompressible viscous fluid between two parallel porous plates with bottom injection and top suction and assume that the wall velocity is uniform.

2 Formulation of the problem

The study laminar flow of an incompressible viscous fluid between two parallel porous plates with bottom injection and top suction at walls and uniform cross flow velocity is considered. The well known governing equations of the flow are:

Continuity equation:

$$\frac{\partial u}{\partial x} + \frac{\partial v}{\partial y} = 0. \tag{1}$$

Momentum equations (without body force):

$$u\frac{\partial u}{\partial x} + v\frac{\partial u}{\partial y} = -\frac{1}{\rho}\frac{\partial p}{\partial x} + \nu\left(\frac{\partial^2 u}{\partial x^2} + \frac{\partial^2 u}{\partial y^2}\right), \tag{2}$$

$$u\frac{\partial v}{\partial x} + v\frac{\partial v}{\partial y} = -\frac{1}{\rho}\frac{\partial p}{\partial y} + \nu\left(\frac{\partial^2 v}{\partial x^2} + \frac{\partial^2 v}{\partial y^2}\right). \tag{3}$$

The flow between two porous plates at y=+h and y=-h, respectively is considered.THe flow is deriven by a pressure gradient $\frac{\partial p}{\partial x}$. It is assumeed that a uniform vertical flow is generated i.e the vertical velocity component is constant everywhere in the flow field i.e $v = v_w = constant$. Again the continuity equation shows that $u = u(y)$ only, the momentum equation (2) becomes:

$$v_w\frac{du}{dy} = -\frac{1}{\rho}\frac{dp}{dx} + \nu\frac{d^2u}{dy^2}. \tag{4}$$

Re-arranging eqn. (4), we have

$$\frac{d^2u}{dy^2} - \frac{v_w}{\nu}\frac{du}{dy} = \frac{1}{\mu}\frac{dp}{dx}. \tag{5}$$

Homogeneous part of eqn. (5) becomes

$$\frac{d^2u}{dy^2} - \frac{v_w}{\nu}\frac{du}{dy} = 0. \tag{6}$$

Eqn. (6) is differential equation, with auxiliary equation of

$$p^2 - \frac{v_w}{\nu}p = 0$$

with roots

$$p_1 = 0, p_2 = \frac{v_w}{\nu}.$$

The solution of eqn. (6) is of the form

$$u(y) = Ae^{p_1 y} + Be^{p_2 y},$$

where A and B are constant.

$$u(y) = A + Be^{\frac{v_w}{\nu}y} \tag{7}$$

For particular integral of eqn. (5), we set

$$u(y) = ay^2 + by + c, \tag{8}$$

where a, b, and c are constants.

$$\frac{du}{dy} = 2ay + b, \Rightarrow \frac{d^2u}{dy^2} = 2a \tag{9}$$

Substituting eqn. (9) in eqn. (5) we get

$$\left(2a - \frac{v_w}{\nu}b\right) - 2a\frac{v_w}{\nu}y = \frac{1}{\mu}\frac{dp}{dx}.$$

Comparing the co-efficients, we get

$$a = 0 \Rightarrow b = -\frac{\nu}{v_w}\frac{1}{\mu}\frac{dp}{dx}. \tag{10}$$

Now, eqn. (8) becomes

$$u(y) = -\frac{\nu}{v_w}\frac{1}{\mu}\frac{dp}{dx}y + c. \tag{11}$$

The final solution formes by adding eqn. (7) and eqn. (11)

$$u(y) = D + Be^{\frac{v_w}{\nu}y} - \frac{\nu}{v_w}\frac{1}{\mu}\frac{dp}{dx}y. \tag{12}$$

Since v_w is constant, the equation is linear. We retain the no-slip condition for the main flow.

$$u(+h) = u(-h) = 0$$

$$u(h) = D + Be^{\frac{v_w}{\nu}h} - \frac{\nu}{v_w}\frac{1}{\mu}\frac{dp}{dx}h \tag{13}$$

$$u(-h) = D + Be^{-\frac{v_w}{\nu}h} + \frac{\nu}{v_w}\frac{1}{\mu}\frac{dp}{dx}h. \tag{14}$$

Subtracting eqn. (14) from eqn. (13), we get

$$B = \frac{2\frac{\nu}{v_w}\frac{h}{\mu}\frac{dp}{dx}}{e^{\frac{v_w}{\nu}h} - e^{-\frac{v_w}{\nu}h}} = \frac{2\frac{\nu}{v_w}\frac{h}{\mu}\frac{dp}{dx}}{2\sinh\left(\frac{v_w}{\nu}h\right)} = \frac{\frac{\nu}{v_w}\frac{h}{\mu}\frac{dp}{dx}}{\sinh\left(\frac{v_w}{\nu}h\right)}. \tag{15}$$

Substituting eqn. (15) into eqn. (13), we get

$$D = -\frac{\frac{\nu}{v_w}\frac{h}{\mu}\frac{dp}{dx}e^{\frac{v_w}{\nu}h}}{\sinh\left(\frac{v_w}{\nu}h\right)} + \frac{\nu}{v_w}\frac{h}{\mu}\frac{dp}{dx}. \tag{16}$$

Eqn. (12) reduces to

$$u(y) = -\frac{\frac{\nu}{v_w}\frac{h}{\mu}\frac{dp}{dx}e^{\frac{v_w}{\nu}h}}{\sinh\left(\frac{v_w}{\nu}h\right)} + \frac{\nu}{v_w}\frac{h}{\mu}\frac{dp}{dx} + \frac{\frac{\nu}{v_w}\frac{h}{\mu}\frac{dp}{dx}e^{\frac{v_w}{\nu}y}}{\sinh\left(\frac{v_w}{\nu}h\right)} - \frac{\nu}{v_w}\frac{y}{\mu}\frac{dp}{dx}. \tag{17}$$

But wall Reynold number is $Re = \frac{v_w}{\nu}h$, $\frac{Re}{h} = \frac{v_w}{\nu} \Rightarrow \frac{h}{Re} = \frac{\nu}{v_w}$.

Re-arranging eqn. (17), we get

$$u(y) = -\frac{h^2}{Re}\frac{1}{\mu}\frac{dp}{dx}\left[\frac{y}{h} - 1 + \frac{e^{Re} - e^{Re\frac{y}{h}}}{\sinh(Re)}\right]. \tag{18}$$

The final solution of eqn. (5),

$$\frac{u(y)}{u_{max}} = \frac{2}{Re}\left[\frac{y}{h} - 1 + \frac{e^{Re} - e^{Re\frac{y}{h}}}{\sinh Re}\right]. \tag{19}$$

Where $u_{max} = \frac{h^2}{2\mu}(-\frac{dp}{dy})$ is the centerline velocity for imporous or poiseuille.

For very small Re (or small vertical velocity), then the last terms in the parentheses of of eqn. (19) can be expanded in a power series and $\sinh Re \approx Re$ i.e.

$$\frac{u(y)}{u_{max}} = \frac{2}{Re}\left[\frac{y}{h} - 1 + \frac{1 + Re + \frac{(Re)^2}{2} + .. - \left(1 + Re\frac{y}{h} + \frac{(Re)^2}{2}\frac{y^2}{h^2} + ..\right)}{Re}\right],$$

$$\frac{u(y)}{u_{max}} = \frac{2}{Re}\left[\frac{y}{h} - 1 + \frac{Re\left(1 + \frac{Re}{2} - \frac{y}{h} - \frac{Re}{2}\frac{y^2}{h^2}\right)}{Re}\right],$$

$$\frac{u(y)}{u_{max}} = 1 - \frac{y^2}{h^2}. \tag{20}$$

Eqn. (20) shows that, the poiseuille solution recovered.

For very large Re (or large vertical velocity), eqn. (19) can be written as

$$\frac{u(y)}{u_{max}} = \frac{2}{Re}\left[\frac{y}{h} - 1 + 2\frac{e^{Re} - e^{Re\frac{y}{h}}}{e^{Re} - e^{-Re}}\right],$$

$$\frac{u(y)}{u_{max}} = \frac{2}{Re}\left[\frac{y}{h} - 1 + 2\frac{1 - e^{-Re\left(1 - \frac{y}{h}\right)}}{1 - e^{-2Re}}\right].$$

For $Re \to \infty$ and $\frac{y}{h} > 1$, except for $y = +h$, we get

$$\frac{u(y)}{u_{max}} = \frac{2}{Re}\left[\frac{y}{h} - 1 + 2\right],$$

$$\frac{u(y)}{u_{max}} = \frac{2}{Re}\left[1 + \frac{y}{h}\right], \tag{21}$$

so that a straight line variation which suddenly drops to zero at the upper wall.

3 Discussion

The velocity profiles have been drawn for different values of Reynold numbers (i.e. Re = 0, 3, 5, 10). From Fig. (1), its observed that for $Re \geq 0$ in the region $-1 \leq y^* \leq 1$, the shapes change smoothly with Reynold numbers and the average velocity is decreasing and Reynold number increases; i.e. the friction factor increases as we apply more cross flow through the wall.

4 Conclusion

In the above analysis a class of solution of flow of viscous fluid between two parallel porous plates with bottom injection and top suction is presented when a cross flow velocity along the boundary is uniform, the convective acceleration is linear and the flow is deriven from pressure gradient.

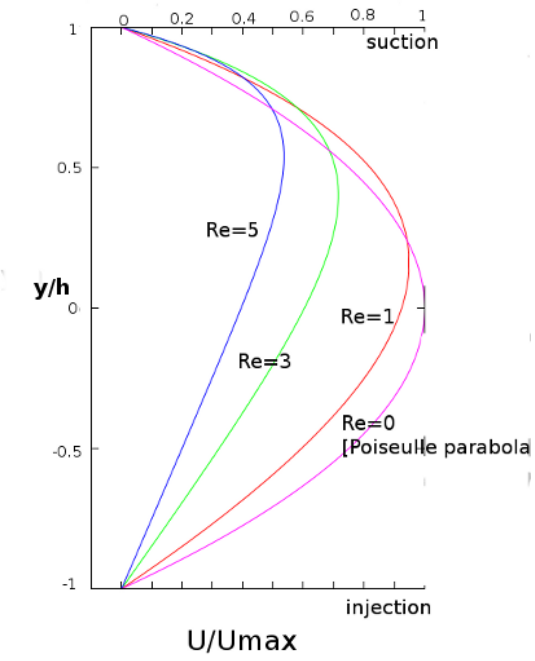

Fig. 1: Velocity profiles for flow between parallel plates with bottom injection and top suction for different values of Re.

Nomenclature

A,B,C,D: Constants
h: Height of the channel
P: Pressure
x: Axial distance
y:Lateral distance
v_w: Lateral wall velocity
u(x,y): Axial velocity component
v(x,y): Lateral velocity component
$y^* = \frac{y}{h}$: Dimensionless lateral distance
$Re = \frac{v_w h}{\nu}$: Wall Reynold number

Greek Symbols

μ: Shear viscosity
ν: Kinematic viscosity
ρ: Fluid density

Submitted on January 20, 2014 / Accepted on January 25, 2014

References

1. Berman A.S. Laminar flow in channels with porous walls. *Journal of Applied Physics*, 1953, v. 24, 1232.
2. Sellars J.R. Laminar flow in channels with porous walls at high suction Reynold number. *Journal of Applied Physics*, 1955, v. 26, 489.
3. Yuan S.W. Further Investigation of Laminar Flow in Channels with Porous Walls. *Journal of Applied Physics*, 1956, v. 27(3), 267–269.
4. Terrill R.M. Homotopy Analysis Solutions for the Asymmetric Laminar Flow in a Porous Channel with Expanding or Contracting Walls. *Aeronautical Quarterly*, 1964, v. 15, 299–310.
5. Terrill R.M., Shrestha G.M. Journal of Applied Mathematical Physics, 1965, v. 16, 470–482.
6. White F. Viscous fluid flow. 2nd edition, Mc Graw-Hill company, New York, 1991.
7. Green G.A. *Laminar flow through a channel with one porous wall*. Course project in Advanced fluid mechanics, 1979, Department of Chemical and Environmental Engineering.

Orbits in Homogeneous Time Varying Spherical Spacetime

Chifu E. Ndikilar

Physics Department, Federal University Dutse, P.M.B 7156, Dutse, Jigawa State, Nigeria. E-mail: ebenechifu@yahoo.com

The solution to Einstein's gravitational field equations exterior to time varying distributions of mass within regions of spherical geometry is used to study the behaviour of test particles and photons in the vicinity of the mass distribution. Equations of motion are derived and an expression for deflection of light in this gravitational field is obtained. The expresion obtained differs from that in Schwarzschild's field by a multiplicative time dependent factor. The concept of gravitational lens in this gravitational field is also studied.

1 Introduction

In [1], the covariant metric tensor exterior to a homogeneous time varying distribution of mass within regions of spherical geometry is defined as:

$$g_{00} = -\left[1 + \frac{2}{c^2} f(t,r)\right] \tag{1}$$

$$g_{11} = \left[1 + \frac{2}{c^2} f(t,r)\right]^{-1} \tag{2}$$

$$g_{22} = r^2 \tag{3}$$

$$g_{33} = r^2 \sin^2\theta \tag{4}$$

where $f(t,r)$ is a function dependent on the mass distribution within the sphere that experiences radial displacement. Einstein's gravitational field equations were constructed in [1] and an approximate expression for the analytical solution of the lone field equation was obtained as

$$f(t,r) \approx -\frac{k}{r} \exp\, i\omega\left(t - \frac{r}{c}\right) \tag{5}$$

where $k = GM_0$ with G being the universal gravitational constant and M_0 the total mass of the spherical body. ω is the angular frequency of the radial displacement of mass within the sphere.

In this article, we use this solution of Einstein's field equations to study the behaviour of light in the vicinity of a time varying spherical mass distribution.

2 Orbits in Time Varying Spherical Spacetime

In order to study the motion of planets and light rays in a homogeneous time varying spherical spacetime, there is need to derive the geodesic equations [2]. The Lagrangian (L) for this gravitational field can be defined using the metric tensor as:

$$L = \frac{1}{c}\left[-g_{00}\left(\frac{dt}{d\tau}\right)^2 - g_{11}\left(\frac{dr}{d\tau}\right)^2 - g_{22}\left(\frac{d\theta}{d\tau}\right)^2 - g_{33}\left(\frac{d\phi}{d\tau}\right)^2\right]^{\frac{1}{2}} \tag{6}$$

Assuming that the orbits remain permanently in the equatorial plane (as in Newtonian Theory), then $\theta = \frac{\pi}{2}$ and the Lagrangian reduces to

$$L = \frac{1}{c}\left[-g_{00}\left(\frac{dt}{d\tau}\right)^2 - g_{11}\left(\frac{dr}{d\tau}\right)^2 - g_{33}\left(\frac{d\phi}{d\tau}\right)^2\right]^{\frac{1}{2}} \tag{7}$$

or more explicitly as

$$L = \frac{1}{c}\left[\left(1 + \frac{2}{c^2} f(t,r)\right)\dot{t}^2 - \left(1 + \frac{2}{c^2} f(t,r)\right)^{-1} \dot{r}^2 - r^2\dot{\phi}^2\right]^{\frac{1}{2}} \tag{8}$$

where the dot denotes differentiation with respect to proper time (τ).

Now, using the Euler-Lagrange equations and considering the fact that in a gravitational field is a conservative field, it can be shown that the law of conservation of energy in this field is given as

$$\left(1 + \frac{2}{c^2} f(t,r)\right)\dot{t} = d\,(constant) \tag{9}$$

or more explicitly as

$$\left[1 - \frac{2GM}{rc^2} \exp\, i\omega\left(t - \frac{r}{c}\right)\right]\dot{t} = d \tag{10}$$

which differs from that in Schwarzschild's field by the exponential factor that describes the radial displacement of mass with time.

It can also be shown that the law of conservation of angular momemtum in this gravitational field is given as

$$r^2\dot{\phi} = h\,(constant) \tag{11}$$

which is the same as that in Schwarzschild's field.

Let $L = \varepsilon$, and equation (8) becomes

$$\varepsilon^2 = \left(1 + \frac{2}{c^2} f(t,r)\right)\dot{t}^2 - \frac{1}{c^2}\left[\left(1 + \frac{2}{c^2} f(t,r)\right)^{-1} \dot{r}^2 - r^2\dot{\phi}^2\right]. \tag{12}$$

Substituting equation (10) in (12) yields

$$\frac{1}{2}\left[\dot{r}^2 + r^2\dot{\phi}^2\left(1 + \frac{2}{c^2} f(t,r)\right)\right] + \varepsilon^2 f(t,r) = \frac{1}{2}c^2\left(d^2 - \varepsilon^2\right). \tag{13}$$

This is the Newtonian energy equation with a modification to the $\dot{\phi}^2$ term. It is similar to that obtained in Schwarzschild's field except for the time dependent radial diplacement. Also, using equation (11), it can be shown that

$$\dot{r} = \frac{dr}{d\phi}\frac{d\phi}{d\tau} = \dot{\phi}\frac{dr}{d\phi} = \frac{h}{r^2}\frac{dr}{d\phi}. \tag{14}$$

Now, let $u(\phi) = \frac{1}{r(\phi)}$ then

$$\dot{r} = -h\frac{du}{d\phi}. \tag{15}$$

Substituting equation (5) and (15) into equation (13) yields

$$\left(\frac{du}{d\phi}\right)^2 + u^2\left[1 - \frac{2k}{c^2}u\ \exp\ i\omega\left(t - \frac{1}{uc}\right)\right] + \frac{2\varepsilon^2 k}{h^2}u\ \exp\ i\omega\left(t - \frac{1}{uc}\right) = \frac{c^2}{h^2}\left(d^2 - \varepsilon^2\right) \tag{16}$$

It is worthnoting that integrating equation (16) directly leads to elliptical integrals which are ackward to handle; thus differentiating yields the following second order differential equation

$$\frac{d^2u}{d\phi^2} + u\left[1 - \frac{2k}{c^2}u\ \exp\ i\omega\left(t - \frac{1}{uc}\right)\right] - \frac{2k}{c^2}u^2\left(1 - \frac{1}{u}\right)\exp\ i\omega\left(t - \frac{1}{uc}\right) + \frac{2k\varepsilon^2}{h^2}\left(1 + \frac{1}{u^2}\right)\exp\ i\omega\left(t - \frac{1}{uc}\right) = 0. \tag{17}$$

This equation has additional terms not found in Schwarzschild's field.

3 Timelike Orbits and Precession

For timelike orbits $\varepsilon = 1$ and equation (17) becomes

$$\frac{d^2u}{d\phi^2} + u\left[1 - \frac{2k}{c^2}u\ \exp\ i\omega\left(t - \frac{1}{uc}\right)\right] - \frac{2k}{c^2}u^2\left(1 - \frac{1}{u}\right)\exp\ i\omega\left(t - \frac{1}{uc}\right) + \frac{2k}{h^2}\left(1 + \frac{1}{u^2}\right)\exp\ i\omega\left(t - \frac{1}{uc}\right) = 0. \tag{18}$$

Now as a first approximation, suppose $uc \gg 1$ and $k \ll h^2u^2$ then equation (8) reduces to

$$\frac{d^2u}{d\phi^2} + u = k\left[\frac{3}{c^2}u^2 + \frac{1}{c^2}u - \frac{1}{h^2}\right]\exp\ i\omega t. \tag{19}$$

The Newtonian equation for a spherical mass is

$$\frac{d^2u}{d\phi^2} + u = \frac{k}{h^2} \tag{20}$$

and that obtained in Schwarzschild's field is

$$\frac{d^2u}{d\phi^2} + u = \frac{k}{h^2} + \frac{3k}{c^2}u^2. \tag{21}$$

Apart from the first and second terms of equation (19) that are similar to Newton's equation and that in Schwarzschild's field, the other terms have terms dependent on the time rate of rotation of the mass content within the sphere [3].

Solution of the Newtonian equation (20) yields the well known conics

$$u_0 = \frac{1}{l}\left(1 + e\cos\theta\right) \tag{22}$$

where $l = \frac{h^2}{GM}$ and e is the eccentricity of the orbit. Attempting an approximate solution for equation (19) by substituting the Newtonian solution into the quadratic term in u on the right hand side and neglecting the term in u, a particular integral u_1 satisfies equation (19) such that

$$\frac{d^2u_1}{d\phi^2} + u_1 = k\left[\frac{3}{l^2c^2}\left(1 + e\cos\theta\right)^2 - \frac{1}{h^2}\right]\exp\ i\omega t. \tag{23}$$

Now suppose u_1 takes the form:

$$u_1 = A\ +\ B\phi\sin\phi\ +\ C\ \cos 2\phi \tag{24}$$

where A, B and C are constants, then it can be shown that

$$u_1 = \frac{k}{c^2}\left(\frac{3}{l^2} - \frac{1}{l} - \frac{1}{h^2}\right)\exp\ i\omega t + \frac{ke\phi}{2c^2}\left(\frac{3}{l^2} - \frac{1}{2l}\right)\sin 2\phi\ \exp\ i\omega t + \frac{ke^2}{l^2c^2}\cos 2\phi. \tag{25}$$

Then the approximate solution for u can be given as

$$u\ =\ u_0\ + u_1 \tag{26}$$

or

$$u = \frac{1}{l}\left(1 + e\cos\theta\right) + \frac{k}{c^2}\left(\frac{3}{l^2} - \frac{1}{l} - \frac{1}{h^2}\right)\exp\ i\omega t + \frac{ke\phi}{2c^2}\left(\frac{3}{l^2} - \frac{1}{2l}\right)\sin 2\phi\ \exp\ i\omega t + \frac{ke^2}{l^2c^2}\cos 2\phi. \tag{27}$$

Hence, this approximate solution introduces corrections to u_0 and hence depicts that the orbits of massive objects is only approximately elliptical and also accounts for the perihelion precession of planetary orbits in this gravitational field.

4 The Bending of Light

For null geodesics, $\varepsilon = 0$ and equation (17) yields

$$\frac{d^2u}{d\phi^2} + u = \left[\frac{3k}{c^2}\exp\ i\omega\left(t - \frac{1}{uc}\right)\right]u^2 + \left[\frac{k}{c^2}\exp\ i\omega\left(t - \frac{1}{uc}\right)\right]u. \tag{28}$$

In the limit of Special Relativity, equation (28) reduces to

$$\frac{d^2u}{d\phi^2} + u = 0. \tag{29}$$

The general solution of equation (29) is given as

$$u = \frac{1}{b}\sin(\phi - \phi_0) \tag{30}$$

where b is the closest approach to the origin (or impact parameter). This is the equation of a straight line as ϕ goes from ϕ_0 to $\phi_0 + \pi$. The straight line motion of light is the same as that predicted by Newtonian theory.

Now, solving the General Relativity problem (equation 28) by taking the general solution (u) to be a pertubation of the Newtonian solution, and setting $\phi_0 = 0$, then

$$u = u_0 + u_1 \tag{31}$$

where $u_0 = \frac{1}{b}\sin\phi$. Thus, u_1 satisfies the equation

$$\frac{d^2u_1}{d\phi^2} + u_1 = \frac{3k}{b^2c^2}\sin^2\phi \exp i\omega\left(t - \frac{b}{c\sin\phi}\right) + \frac{k}{bc^2}\sin\phi \exp i\omega\left(t - \frac{b}{c\sin\phi}\right). \tag{32}$$

Now, by considering a particular integral of the form

$$u_1 = A + B\sin^2\phi \tag{33}$$

and substituting in equation (32), it can be shown that

$$u_1 = \frac{2k}{b^2c^2}\left(1 - \frac{1}{2}\sin^2\phi\right)\exp i\omega\left(t - \frac{b}{c\sin\phi}\right) \tag{34}$$

and thus

$$u = \frac{1}{b}\sin\phi + \frac{2k}{b^2c^2}\left(1 - \frac{1}{2}\sin^2\phi\right)\exp i\omega\left(t - \frac{b}{c\sin\phi}\right). \tag{35}$$

Now, consider the deflection of a light ray from a star which just grazes the time varying homogeneous spherical mass (such as the Sun approximately); as in Fig. 1, then as $r \to \pm\infty$, $u \to 0$, so

$$0 = \frac{1}{b}\sin\phi + \frac{2k}{b^2c^2}\left(1 - \frac{1}{2}\sin^2\phi\right)\exp i\omega\left(t - \frac{b}{c\sin\phi}\right). \tag{36}$$

At the asymptotes, $\phi = -\psi_1$ and $\phi = \psi_2 + \pi$ and taking $\phi \ll 1$ then equation (36) reduces to

$$0 = \frac{1}{b}\psi_1 + \frac{2k}{b^2c^2}\exp i\omega\left(t + \frac{b}{c\psi_1}\right) \tag{37}$$

and

$$0 = \frac{1}{b}\psi_2 + \frac{2k}{b^2c^2}\exp i\omega\left(t + \frac{b}{c\psi_2}\right). \tag{38}$$

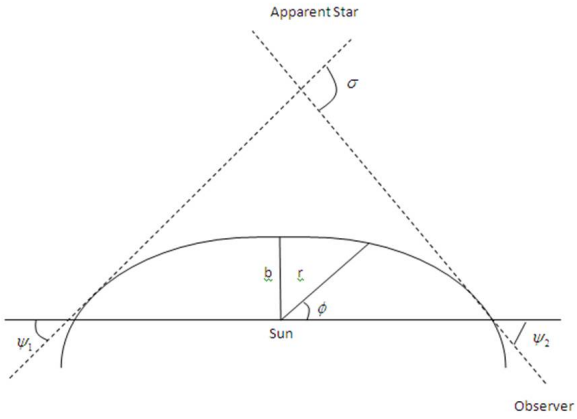

Fig. 1: Diagram showing the total deflection of light.

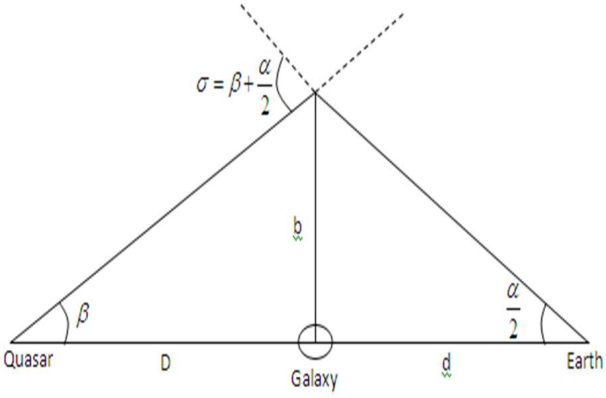

Fig. 2: Einstein's Ring.

The total deflection of light (σ) is given as

$$\sigma = \psi_1 + \psi_2$$

or

$$\sigma = \frac{2k}{bc^2}\left[\exp i\omega\left(t + \frac{b}{c\psi_1}\right) + \exp i\omega\left(t + \frac{b}{c\psi_2}\right)\right]. \tag{39}$$

Thus, the introduction of varying mass distribution with time introduces an exponential term in the deflection of light equation not found in static homogeneous spherical gravitational fields.

Now, as an example of the bending of light, let us consider a gravitational lens.

Consider a quasar directly behind a galaxy in our line of sight as shown in Fig. 2.

The distance of closest approach to the time varying spherical mass distribution corresponds to an angle (σ) given

as equation (39). From Fig. 2, considering that both α and β are small, it can be deduced that

$$\sigma = \frac{\alpha}{2} + \beta = \frac{b}{d} + \frac{b}{D} \tag{40}$$

and substituting equation (39) yields the impact parameter as

$$b = \left\{ \frac{2k}{c^2} \left(\frac{Dd}{D+d} \right) \left[\exp i\omega \left(t + \frac{b}{c\psi_1} \right) + \exp i\omega \left(t + \frac{b}{c\psi_2} \right) \right] \right\}^{\frac{1}{2}}.$$

Hence, the image of the quasar appears as a ring which subtends an angle

$$\alpha = \frac{2b}{d}$$

or

$$\alpha = \frac{2}{c} \left\{ \frac{Dd}{d(D+d)} \left[\exp i\omega \left(t + \frac{b}{c\psi_1} \right) + \exp i\omega \left(t + \frac{b}{c\psi_2} \right) \right] \right\}^{\frac{1}{2}}.$$

5 Conclusion

The results obtained in this study has paved the way for the theoretical study of homogeneous spherical mass distributions in which the mass content is varying with time. This will introduce correction terms found in Schwarzschild's static field. It is hoped that using this approach experimentally and astrophysically more satisfactory expressions and values will be obtained for gravitational phenomena in the universe.

Submitted on December 30, 2013 / Accepted on January 25, 2014

References

1. Chifu E.N. and Howusu S.X.K. Solution of Einstein's Geometrical Gravitational Field Equations Exterior to Astrophysically Real or Hypothetical Time Varying Distributions of Mass within Regions of Spherical Geometry. *Progress in Physics*, 2009, v. 3, 45–48.
2. Chifu E.N., Usman A. and Meludu O.C. Orbits in Homogeneous Oblate Spheroidal Gravitational Space-Time. *Progress in Physics*, 2009, v. 3, 49–53.
3. Weinberg S. Gravitation and Cosmology. J. Wiley, New York, 1972.

Exogenous Mechanism of the Time Sensor of Biological Clock

Takhir R. Akhmedov
333 S. Webster Ave, Suite 4, Norman, OK 73069. E-mail: TakhirAkhmedov@yandex.com

The problem of time sensor of a biological clock attracts interest of many scientists, and a great number of experiments are being conducted to study the influence of various physical and chemical factors on functioning of a biological clock. Analyzing publications and considering our own original results a physical exogenous mechanism of biological clock is formulated that adequately explains the obtained experimental data.

The problem of biological rhythms i.e. biorhythms (BR) with periodicity close to the periodicity of geophysical phenomena has been attracting interest of scientists for centuries. And a great number of experiments carried out on different organisms beginning from single-cell creatures and plants to animals and human beings confirm that biological organisms have the ability to measure time [1–6] and biological clocks (BC) really exist.

The central problem in this matter is explanation of how time sensor (TS) of a BC functions and of the very basic mechanism of TS. Attempts had been made to study the influence of different chemical and physical factors on the parameters of BC.

The most thoroughly studied rhythms are those with a period close to 24 hours. These are so called circadian rhythms (CR). Fewer works are devoted to lunar rhythms (LR) which are of periods around 29.53 and 14.77 days. A few works involve yearly rhythms, and there is information about a period of about 180 million years of the Earth‘s biosphere productivity [4].

In an attempt to determine the mechanism of TS influences of the following factors have been studied on the parameters of CR: illumination [7], light/darkness cycles [8], electrical and magnetic fields of the Earth [9, 10], and absence of such [11], temperature variations [12, 13], chemicals [14,15]. There were experiments in constant pressure and temperature environments [17].

The main properties of BC obtained from experiments are presented in [16]. The noteworthy fact is that the study of BC had been carried out on biological objects using parameters, which are the last stages of long chains of complex biochemical reactions and processes. In fact, in biological experiments researchers observe the motion of the “hands” of BC. Naturally, such observations do not allow revealing the mechanism of BCTS that controls the “hands” of the clock. Thus, the study of biological objects makes it impossible to draw conclusions about the specific stages where one or another factor begins to affect the biochemical chain of reaction. This means, it is difficult to come to a single conclusion, that the observed effects were the result of the action of a single factor on the mechanism of time BCTS. And, as J. Gustings noticed it is impossible to give an example of an isolated and studied biochemical system, which possesses the properties that would reveal the factor and the location of such factor’s influence on CR [14].

The summarized conclusion coming from broad experimental data is that physical and chemical factors, whose influence on BC have been studied, do not have any relationship with the mechanism of BCTS, but only play a synchronizing role. Namely, the factor whose influence is studied only affects the “hand” of the clock by force shifting it one way or another without affecting the actual mechanism behind the “face” of the clock, i.e. without changing the period of CR.

As a result the conclusion is drawn that the period of BC, particularly of CR, is independent from external factors. And thus this period of the rhythms must be defined by organisms independently from external factors, periodic or non-periodic, of physical or chemical nature. This hypothesis is based on three well known facts:

i. The difference of the period from 24 hours in experiments in constant conditions;

ii. Easiness of shifting the phase of the rhythms;

iii. Stability of the rhythm period during latitudinal shifts, that followed by the change of all geophysical factors determined by place and time.

But none of these facts can be accepted as a definite proof as it is established in scientific world [17].

Overall experimental data from studies of BCTS mechanism do not permit to arrive to a single conclusion regarding the physical foundation of BCTS. Therefore, presently the hypothesis of endogenous mechanism of BCTS is generally accepted. Though there are facts that may support a combined exogenous-endogenous mechanism [7]. Such attempts encourage search for processes (of physical or simple chemical nature) that would allow identifying possibly a single simple mechanism of BCTS.

Circadian periodicity of evaporation of water from a thermostated essel*

Initial experiments were carried out in 1974. During one of experiments (see the footnote) it became necessary to obtain a stable flow of water vapor of low intensity (1.4×10^{-5} kg/s).

*These experimental data had been obtained in 1974 by a group of physicists headed by Prof. M. A. Asimov. The author of the present article was a responsible leader for the experiments.

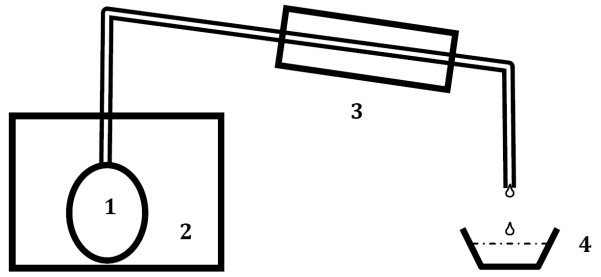

Fig. 1: (1) Container filled with distilled water; (2) Thermostated chamber with inside temperature of $103 \pm 0.1^{\circ}$C; (3) Cooling system; (4) Container where the water condensate was collected

For this, the experimental setup, schematics plotted on Fig. 1, had been assembled.

Container (1) with distilled water was placed into the thermostated chamber (2), where stable temperature at $103 \pm 0.1^{\circ}$C was maintained. Water was boiling inside the container (1). The water vapor went through the cooling system (3) and precipitated into the container (4). The mass of the evaporated/precipitated water was measured every 15 min and a set of 4 measurements had been plotted on the Fig. 2a and 2b. The experiments were carried out uninterruptedly by a number of series of 1 to 7 days of duration.

In order to thoroughly investigate the rate of water vaporization power supply of the thermostat was carefully stabilized, all containers and tubes and connections were thermally insulated, mass was carefully measured and stability of the temperature was closely monitored. The data coming from the measurements strongly suggested the existence of CR in the physical process of distilled water evaporation from a thermostated container.

Measurements were repeated 2001. Due to the limited resources and financial restrictions, the measurements were conducted for only 24 hours. The data collected in 2001 is plotted on Fig. 2b.

Simultaneously, external parameters were monitored. In the Fig. 3, these parameters were plotted vs. time of the day. Namely, temperature of the thermostated chamber T_{hot}, temperature of the liquid in cooling system T_{cold}, ambient temperature T_{amb}, atmospheric pressure p in mm Hg, relative humidity η, and voltage of the power supply were plotted vs. time. As it is clear from Fig. 3, no significant correlation was observed between external parameters and the mass of the evaporated/precipitated water*.

Lunar rhythm in the reaction of vapor conversion of methanol

The stable vapor flow of low intensity was necessary for studying of chemical reaction of vapor conversion of methanol. The reaction used in chemical industry to produce hydrogen is described by a formula:

$$CH_4 + 2H_2O \xrightarrow{450^{\circ}C} CO_2 + 4H_2 \qquad (1)$$

To investigate time dependence of the reaction speed there were provided stable flows of gaseous CH_4 and water vapor (deviations were $\pm 0.3\%$ and $\pm 3\%$, respectively).

The experiment had been carried out for 540 hours in October and November of 1974. In Fig. 4 the experimental measurements were plotted, y axis shows the fraction of residual methane in the converted dry gas at the output of the reactor.

Composition of the gas at the output was analyzed by the method of gas chromatography. Every 15 min three chromatographs were collected; results of 2-4 hour measurements

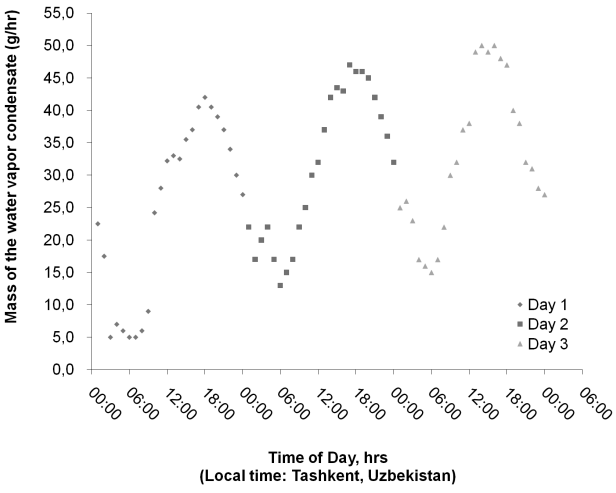

(a)

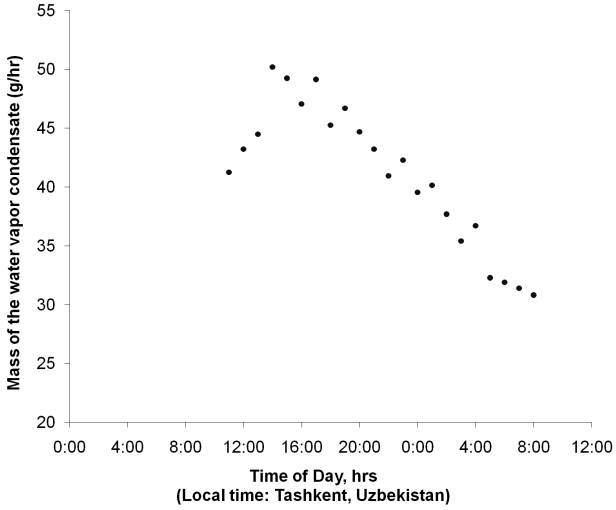

(b)

Fig. 2: Variation of the mass of collected water condensate vs. time of the day

*Experiment conducted in 2001 was made possible by generous technical assistance of Abdulaev Khikmat at the Biology Department of Tashkent State University.

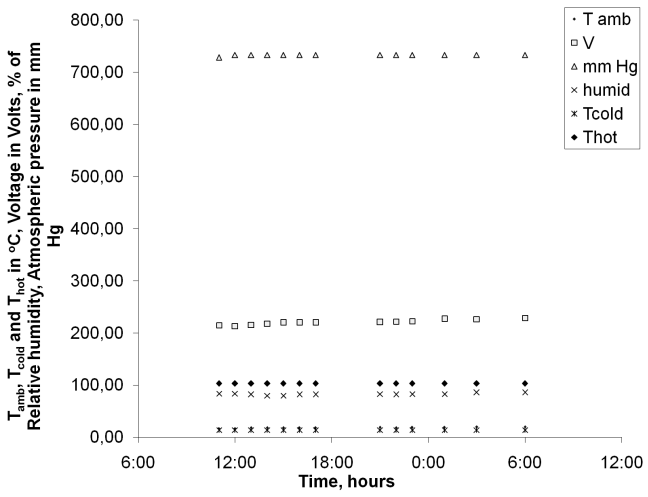

Fig. 3: Monitoring of external parameters of temperature of the thermostated chamber T_{hot}, temperature of the liquid in cooling system T_{cold}, ambient temperature T_{amb}, atmospheric pressure p in mm Hg, relative humidity η, and voltage of the power supply were plotted vs. time. Experiments were conducted in summer of 2001.

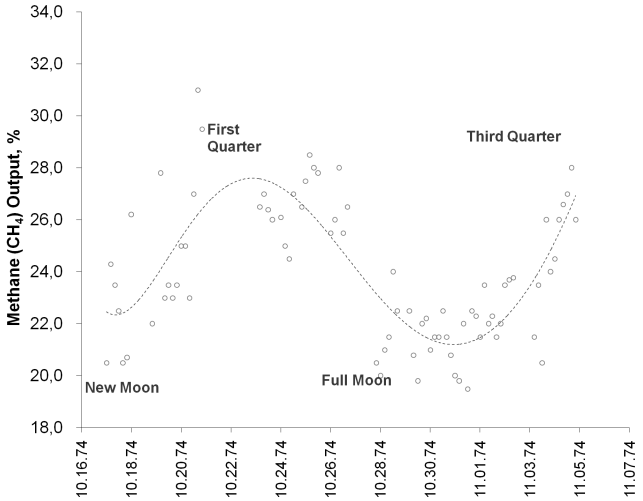

Fig. 4: Concentration of residual CH_4 in % in vapor conversion reaction output. (Experimental data presented in this figure were obtained in Tashkent State University, Uzbekistan by Docent M. A. Azimov's group, headed by Mr. Takhir R. Akhmedov in 1972–75)

were averaged and then plotted on the Fig. 4.

Results of these studies indicated on the existence of a lunar rhythm in the chemical reaction of vapor conversion of methanol at T = 450°C. This temperature is noticeably higher than temperature of any known living organism.

Discussion

A sum total of published experimental data and mentioned above original results of revealing of CR in water evaporation from a thermostated vessel (at T = 103°C), and LR in chemical reaction of vapor conversion of methanol (at T = 450°C) allowed to conclude that the mechanism of BCTS has exogenous nature.

Let's analyze changing of kinetic and potential energy of atoms/molecule on the surface of the Earth. An atom/molecule on the surface of the Earth takes part in following motions:

1. Spinning of the Earth around its own axis with the surface speed $V_1 = 465 \times \cos\alpha$ m/s, where α – is latitude;
2. Revolving with the Earth around the Sun with a linear speed of $V_2 = 3 \times 10^4$ m/s;
3. Moving with the Solar system around the center of the Galaxy with a linear speed of about $V_3 = 2.5 \times 10^5$ m/s;
4. Moving with the Galaxy from the center of the Universe with a linear speed of about $V_4 = 6 \times 10^5$ m/s [18];

It's known that total mechanical energy is the sum of kinetic energy KE and potential energy U:

$$E_{total} = KE + U \qquad (2)$$

And, if any of these components or both of them change according to a law, then the total energy will change according to the same law. And the change can be potentially affecting any physical, chemical or biological process.

The factors 1-3 cause changing of kinetic energy of atoms/molecules on the surface of the Earth with periods, respectively, 24 hours (CR), a year (year rhythm), 180 million years (the Galaxy "year" rhythm). The existence of the rhythms has been mentioned above. Analysis of the kinetic energy changing leads us to the following formula:

$$E_{max} - E_{min} = 2m \times V_T \times V_E \times \cos\alpha \qquad (3)$$

where m – mass of an atom/molecule, V_T – thermodynamic speed of an atom/molecule, V_E – the orbital speed of the Earth's surface on the equator, α – latitude.

Formula (3) evaluates the change of kinetic energy of H_2O molecule caused by orbital spinning of the Earth. Calculations show that the change of the kinetic energy is equivalent to the temperature change in the order of 1°C, which in turn explains the existence of a minimum/maximum of water evaporation from a thermostated vessel at 6 a.m./6 p.m. of the local time. Similar changes of energy in biological objects naturally lead to emerging of CR in them.

It should be underlined, that the argument I (differ of CR period from 24 hours), interpreted in the favor of endogenous mechanism of BCTS, actually proves exogenous character of the BCTS mechanism [15]. The argument II – easiness of shifting of CR phase in biological objects is not related to the mechanism of functioning of BC, but is the result of response of bio-objects to the external environmental factors, and the response is of biochemical nature.

The argument III – conservation of the rhythm during latitudinal shift – naturally follows from the above offered interpretation of the mechanism of BCTS. As the speed of an atom/molecule on the surface of the Earth is described by a formula:

$$V = V_T + V_E \cos\alpha \quad (4)$$

And for a given time zone during latitudinal shifting the BC of a studied object conserves circadian periodicity. But the shifting can be followed by a change of the amplitude. CR of bio-objects should disappear on the Poles of the Earth and in space (space stations).

As it's known, an atom/molecule besides kinetic energy possesses potential energy. E_{poten} in (2) for atoms/molecules on the surface of the Earth changes with a period equal to lunar rhythm, that is caused by displacement of celestial bodies in the system Sun-Earth-Moon. And temperature equivalent of the effect is of order of 10-20°C for the researched chemical reaction. The same mechanism of the energy changing may cause changing of daily global temperature [19].

Conclusions

1. The rhythms with periods close to geophysical rhythms (circadian rhythm, lunar rhythm, a year rhythm, and a rhythm of Earth's biosphere productivity-the Galaxy rhythm) have fundamental nature and take place not only in bio-objects, but also in physical and chemical processes at temperatures significantly higher then temperature of bio-objects.
2. The mechanism of time sensor of biological clock has exogenous nature.
3. The time sensor of biological clock is the changing of total energy E_{total} = KE + U of atoms/molecules on the surface of the Earth, caused by moving of the Earth in Space.
4. For global prove of the results and theoretical interpretation, experiments may be held to study the process of water evaporation from a thermostated vessel simultaneously in different places of the same latitude and/or longitude.

Submitted on December 6, 2013 / Accepted on December 9, 2013

References

1. Bunning E. Rhythms of Physiological Processes. FL, 1961.
2. Biological Clock. Trans. from Eng. with introduction by Shnol' S. E. Moscow, Mir, 1964 (further quoted as "*BC*").
3. Biological Rhythms. Vols. 1–2, Ed. Achhoff J. Moscow, Mir, 1984.
4. Malinovsky Yu. M. Dependence of the Earth's biosphere productivity on the Sun system position in Galaxy. *Problems of Space Biology*. Moscow, Nauka, 1973, v. 18.
5. Wilkins M. Influence of light on the rhythms of plants. In: *BC*, Moscow, Mir, 1964, 196.
6. Emme A. M. Biological clock. Novosibirsk, 1967.
7. Higo A. *Fed Proc.* 1977, v. 36 (2), 109.
8. Edmund L. N. etc. *Chronobiologia*, 1977, v. 4 (2), 109.
9. *Problems of Space Biology*. Moscow, Nauka, 1987, v. 37.
10. *Problems of Space Biology*. Moscow, Nauka, 1973, v. 18.
11. *Problems of Space Biology*. Moscow, Nauka, 1978, v. 37, 16.
12. Suinni B., Gustings J. In: *BC*, Moscow, Mir, 1964, 153.
13. Lukat K. *Expericutis*, 1978, v. 34 (4), 474.
14. Gustings J. Biochemical aspects of rhythms: phase shift, caused by chemical compounds. In: *BC*, Moscow, Mir, 1964, 220.
15. Brukmann K. J. *Interdiscipl. Cycle. Res.*, 1976, v. 7 (2), 149–170.
16. Pittendrigh C. S. Circadian rhythms and the circadian organization of living systems. In: *BC*, Moscow, Mir, 1964.
17. Brown F. Geophysical factors and problems of biological clock. In: *BC*, Moscow, Mir, 1964, 103.
18. Bakulin G. I. and others. General Course of Astronomy. Moscow, 1966.
19. Balling R. C. Jr. and Cerveny R. S. *Science*, 1995, v. 267, 1481–1482.

On the Effect of Lengthening Circadian Rhythm by Heavy Water

Takhir R. Akhmedov

333 S. Webster Ave, Suite 4, Norman, OK 73069. E-mail: TakhirAkhmedov@yandex.com

The problem of time sensor of biological clock (BC) attracts interest of many scientists, and a great number of experiments are being conducted to study the influence of various physical and chemical factors on functioning of BC. Special attention is drawn to studying the influence of heavy water (D_2O) on functioning of BC that always leads to lengthening of circadian rhythms (CR). This work presents theoretical consideration of lengthening of CR, when hydrogen (H_2) in water is replaced by deuterium (D_2), that is based on spacial difference of energy levels with similar principle quantum numbers.

The problem of the mechanism of time sensor (TS) of biological clock (BC), or biorhythms of periods close to periods of geophysical factors, attracts attention of scientists for a long time. The most thoroughly experimentally studied are circadian rhythms (CR) i.e. rhythms with a period close to 24 hours. And in a range of data about physical and chemical factors unfluence on CR there is a special case for the effects of D_2O on the rhythms. In [3, 4] it is noticed "that at present D_2O is the only matter, which always leads to lengthening of endogenous rhythms", and it is underlined, that theoretical interpretation of "the effect of heavy water" is based on the theory of reactions' absolute speeds, neglecting mass effects. However, the principle difference of H_2O and D_2O is the difference of masses of hydrogen and deuterium nuclei.

Consideration of the mass difference permits qualitave explanation of the lengthening of CR in biological objects, where H_2O is partially or completely replaced by D_2O.

Let's consider spacial distribution of energy levels of the same principle quantum number in atoms of hydrogen and deuterium. Taking into account the masses of the nuclei energy levels are separated by the distance.

$$r_{nH} = \frac{\alpha}{4\pi} \times \frac{1}{R_H} \times n^2 \qquad \text{in a hydrogen atom, and}$$

$$r_{nH} = \frac{\alpha}{4\pi} \times \frac{1}{R_D} \times n^2 \qquad \text{in a deuterium atom}$$

where α is fine structure constant, R_H and R_D are Rydberg constants for hydrogen and deuterium, respectively, n – the main quantum number [4].

In comparison with the similar levels of hydrogen atom in an atom of deuterium energy levels of the same principle quantum number are spatially shifted towards the nucleus by the value of

$$\Delta r = n^2 \times \frac{\alpha}{4\pi} \times \left(\frac{1}{R_H} - \frac{1}{R_D} \right)$$

Accepting that $\alpha = 7.397535 \times 10^{-3}$, $R_H = 109677.576\ \text{cm}^{-1}$ and $R_D = 109707.419\ \text{cm}^{-1}$, for $n = 1$, we have $r_1 = 1.3937 \times 10^{-12}$ cm. For example for $n = 10$, $r_{10} = 1.3937 \times 10^{-10}$ cm.

It is natural to assume, that the lower the energy threshold through which biochemical processes run in bio-objects the higher the sensitivity of the objects to the spatial shift of energy levels caused by the replacement of H_2 by D_2.

Thus, from above mentioned it follows that lengthening of CR by adding D_2O is caused by decreasing the possibility of biochemical processes running through the appropriate energy levels in deuterium atoms, which, being caused by mass difference, are spatially shifted towards the nucleus in comparison with analogous levels in hydrogen.

Submitted on December 6, 2013 / Accepted on December 9, 2013

References

1. Biological Rhythms. Ed. by Yu. Aschoff. Vols. 1–2, Moscow, Mir, 1984.
2. Biological Clock. Transl. from Eng. with introduction by Shnoll S. E.. Moscow, Mir, 1964.
3. Lobyshev V. I., Kalinchenko L. P. Isotope Effects in Biological Systems. Moscow, Nauka, 1978.
4. Dowse H. B. and Palmer J. D. The chronomutagenic effect of Deuterium Oxide on the period and entrainment of a biological rhythm. *Biological Bulletin*, 1972, vol. 143 (3), 513–524.
5. Shpolsky S. E. Atomic Physics. Vol. 1. Moscow, Nauka, 1973.

Progress in Physics is an American scientific journal on advanced studies in physics, registered with the Library of Congress (DC, USA): ISSN 1555-5534 (print version) and ISSN 1555-5615 (online version). The journal is peer reviewed and listed in the abstracting and indexing coverage of: Mathematical Reviews of the AMS (USA), DOAJ of Lund University (Sweden), Zentralblatt MATH (Germany), Scientific Commons of the University of St.Gallen (Switzerland), Open-J-Gate (India), Referential Journal of VINITI (Russia), etc. Progress in Physics is an open-access journal published and distributed in accordance with the Budapest Open Initiative: this means that the electronic copies of both full-size version of the journal and the individual papers published therein will always be acessed for reading, download, and copying for any user free of charge. The journal is issued quarterly (four volumes per year).

Electronic version of this journal: http://www.ptep-online.com

Postal address:
Department of Mathematics and Science, University of New Mexico,
705 Gurley Avenue, Gallup, NM 87301, USA

Printed in the United States of America